2018

A MICROSTRUCTURE-BASED MODEL VALIDATED EXPERIMENTALLY FOR QUANTIFICATION OF SHORT FATIGUE CRACK GROWTH IN THREE-DIMENSIONS

Pei Cai

University of Kentucky, peic29@gmail.com
Author ORCID Identifier:
https://orcid.org/0000-0003-2373-6398
Digital Object Identifier: https://doi.org/10.13023/etd.2018.385

A MICROSTRUCTURE-BASED MODEL VALIDATED
EXPERIMENTALLY FOR QUANTIFICATION OF SHORT FATIGUE
CRACK GROWTH IN THREE-DIMENSIONS

_____

DISSERTATION

_____

A dissertation submitted in partial fulfillment of the
requirements for the degree of Doctor of Philosophy in the
College of Engineering at University of Kentucky

By

Pei Cai

Lexington, Kentucky

Director: Dr. Tongguang Zhai, Associate Professor of Materials Engineering

Lexington, Kentucky

2018

ABSTRACT OF DISSERTATION

A MICROSTRUCTURE-BASED MODEL VALIDATED
EXPERIMENTALLY FOR QUANTIFICATION OF SHORT FATIGUE
CRACK GROWTH IN THREE-DIMENSIONS

Built on the recent successes in understanding the crystallographic mechanism for short fatigue crack (SFC) growth across a grain boundary (GB) and developing an experimental method to quantify the GB resistance against short crack growth, a microstructure-based model was developed in this study to simulate the growth behaviors of SFCs in 3-D, by taking into account both the driving force and resistance along at each point along the crack front in an alloy. It was found that the GB resistance was a Weibull function of the minimum twist angle of crack deflection at the boundary in AA2024-T3 Al alloys. In the digital microstructure used in the model, the resistance at each GB that the short crack interacted with could be calculated, as long as the orientations of grains and the crack were known. In the model, an influence function accounting for the overlapping effect of the resistance from the neighboring grain boundaries was proposed, allowing for calculation of the total resistance distribution along the crack front. In order to overcome the time consuming problem for the existing equations to derive the distribution of stress intensity factor along the crack front under cyclic loading, an analytical equation was proposed to quantify the stress intensity factor distribution along an irregular shape planar crack. By introducing two shape-dependent factors, the fractured area and the perimeter of the crack front, the newly proposed equation could readily and accurately derive the stress intensity factor distribution along the crack front that had large curvatures and singularities. Finally, a microscopic-scale Paris' equation was proposed that took into account both the driving force, i.e., stress intensity factor range, and the total resistance to calculate the growth rate at each point along crack front. The model developed in this work was able to incorporate microstructure, such as grain size and shape, and texture into simulation of SFC growth in 3-D. It was capable of simulating all the anomalous growth behaviors of SFCs, such as the marked scatters in growth rate measurement, retardation and arrest at grain boundaries, and crack plane deflection at grain boundaries, etc.

The model was used to simulate the growth behaviors of SFCs initiated from pre-fractured constituent particles in order to interpret the multi-site fatigue crack initiation observed in AA2024-T351 Al alloys. Three types of SFCs were observed initiating from

these particles, namely, type-I non-propagating cracks; type-II cracks which were arrested soon after propagating into the matrix; and type-III propagating cracks. To quantitatively study the 3-D effects of particle geometry and micro-texture on the growth behaviors of micro-cracks in these particles, rectangular micro-notches with different dimensions were fabricated using focused ion beam in the selected grains on the T-S planes in AA2024-T351 Al alloys, to mimic the pre-fractured particles in these alloys. Knowing the notch dimensions or particle shape, grain orientation and GB geometry, the simulated crack growth behaviors were consistent with the experimental observations, and the model was able to verify that the three types of cracks evolved from these particles were mainly associated with the thickness and width of the pre-fractured particles, though the particle geometry and grain orientation could also affect the behaviors of fatigue crack initiation at the particles. When the widths of the particles were less than 15 μm, like in most high strength Al alloys, the simulated results confirmed that the crack type was only associated with the particle thickness, consistent with the experimental results in AA2024-T351 alloys with a strong rolling texture. The lives for the SFCs to reach 0.5 mm in length were quantified with the model in the AA2024 alloy, revealing that there was a bimodal distribution in the life spectrum calculated, with the longer life peak being related to larger twist angles of crack deflection at the first GB the cracks encountered and the shorter life peak being associated with small twist angles ($< 5°$) at the first GB.

The model further demonstrated the influence of grain structure on SFC growth by considering two different grain structures with the same initial short crack, namely, a layered grain structure with only the primary GBs perpendicular to the surface and the layered grains with both primary and secondary GBs. Depending on their positions and geometry, the secondary GBs could still exert a strong retarding effect on SFC growth on surface. The model was validated by matching to the growth rate measured on surface of a SFC in an AA8090 Al-Li alloy. Good consistency was achieved between the simulated and experimentally measured growth rates when both the primary and secondary GBs were considered in the model. The model developed in this study exhibits its potential applications to optimizing the microstructure and texture in alloys to enhance their fatigue resistance against fatigue crack growth, and to satisfactory life prediction of engineering alloys.

KEYWORDS: High strength aluminum alloys, short fatigue crack growth, grain boundary, constituent particles, crystallographic orientation.

Pei Cai
_____

08/05/2018
_____

A MICROSTRUCTURE-BASED MODEL VALIDATED
EXPERIMENTALLY FOR QUANTIFICATION OF SHORT FATIGUE
CRACK GROWTH IN THREE-DIMENSIONS

By

Pei Cai

Dr. Tongguang Zhai
———————————————————
Director of Dissertation

Dr. Matthew Beck
———————————————————
Director of Graduate Studies

08/05/2018
———————————————————

ACKNOWLEDGMENTS

TABLE OF CONTENTS

LIST OF TABLES

LIST OF FIGURES

CHAPTER 1   Introduction

1.1   Background

The term "fatigue" was firstly introduced in the engineering context by Braithwaite in 1854 [1]. In his work, he attributed the failures after repeated use of engineering components, i.e. brewery equipment, crankshafts, railway axles, and levers, etc., to fatigue damage [2]. A formal descriptive definition of fatigue first appeared in the International Organization for Standardization in which fatigue was described to "apply the changes in properties which can occur in a metallic material due to the repeated application of stresses or strains, although usually this term applied specially to those changes which lead to cracking or failure".

First systematic investigations of metal fatigue were conducted by August Wöhler, a German railway engineer, during 1858-1870 [1]. His work, i.e. *cf.* [3], led to the concept of fatigue "endurance limit" and the characterization of fatigue behavior in terms of stress amplitude-life (S-N) curves, which was called "Wöhler curves" until Basquin [4] represented the finite life region in the form of log-log plot in 1910 resulting in a linear relationship. For some materials, the S-N curve flattens out at lower stress amplitudes, so that, below the endurance limit, σ_e, failure dose not occur no matter how many loading cycles, for instance, as shown in Figure 1.1 which illustrates the S-N curve of 1045 steel [5]. While for other materials like aluminum alloys, there are no such a well-defined

endurance limit in their S-N curves, as seen in the S-N curve of an AA2024-T6 aluminum alloy (Figure 1.1).

Numerous efforts were made in the early 1900s trying to describe the fatigue failure process quantitatively. Among them, George Irwin [6] firstly showed that the amplitude of the stress singularity ahead of a crack could be expressed in terms of the scalar quantity known as the stress intensity factor, K [7], which allows rapid development of linear elastic fracture mechanics (LEFM). When subjected to monotonic, quasi-static loading, the initiation of crack advance can occur if K is larger than the critical value of the stress intensity factor, K_c (or fracture toughness K_{Ic} when under mode I loading). Later on, in cyclic loading conditions, Paris, Gomez and Anderson [8-9] correlated the increment of fatigue crack length per loading cycle, da/dN, with the range of the stress intensity factor, ΔK, during a constant amplitude cyclic loading, and now this is well known as Paris "law":

$$\frac{da}{dN} = C \cdot \Delta K^m$$

Where C and m are empirical constants depending on material properties. However, the process of crack growth is much more complicated than the description by this equation. As illustrated in Figure 1.2, the black curve shows the typical growth rate of a long fatigue crack as a function of its stress intensity factor range at constant amplitude of cyclic loadings, which can be divided into three regions, region I: no crack propagation below a threshold value of ΔK (however, short fatigue cracks show anomalously growth behaviors below $\Delta K_{threshold}$, which will be discussed later in this chapter); region II: stable crack growth where log(da/dN) is linearly proportional to logΔK; and region III: rapid

crack growth to rapture. As shown in Figure 1.2, Paris law describes only region II of the growth process of a long fatigue crack.

In contrast to long fatigue cracks, an accelerated growth behavior of short fatigue cracks which are defined usually to be from a fraction of a millimeter to several millimeters long [7] was firstly observed by Pearson in 1975 [10]. As shown in Figure 1.2, the growth rates (blue dash lines) of short fatigue cracks can be much higher than those of long cracks under the same nominal driving force. Additionally, the transient deceleration or even permanent arrest of short fatigue cracks, as shown in Figure 1.2, were also reported when a short crack interacted with a grain boundary [11, 12]. Numerous experimental observations have confirmed this anomalous growth behavior of short fatigue crack, which was strongly affected by the local microstructure of not only grain boundaries, but also particles, voids and grain orientation etc. [13-15]. However, such retardation in short fatigue crack growth cannot be explained with LEFM from which both the nominal driving force ΔK and the crack growth rate are expected to increase as the crack propagates. Although extensive work has been carried out on short fatigue crack growth in the past several decades [16-18], the mechanisms of these anomalous growth behaviors are still not quantitatively understood. In the next section, the current findings and remaining challenges in understanding the influences of different microstructure-features on short fatigue crack growth are summarized and discussed.

1.2   The effects of microstructure-features on short fatigue crack growth

Since growth of a short fatigue crack can consume 50 to 90% of the fatigue life, quantitative understanding of its growth behaviors becomes crucial for accurate

estimation of the fatigue life of a material in order to prevent the unexpected catastrophic failure of an engineering structure due to fatigue damage [7, 19]. Previous studies [20-26] have shown that microstructural features in an engineering alloy, i.e. second phase particles, grain boundaries and grain orientation, have significant impacts on the fatigue properties, especially during initiation and early growth of short fatigue cracks.

1.2.1 Grain boundary and grain size

Microstructural interfaces, i.e. grain boundaries, are well recognized as one of the major barriers against short fatigue crack growth [7]. Deceleration of the growth rate or even complete arrest of a short fatigue crack at grain boundaries were observed in many engineering metallic materials [12, 27]. Figure 1.3 is an example showing scattered growth rates of crack tips measured on the sample surface with respect of its crack length, in which each drop of *da/dN* is associated with the interaction of the crack tip with a grain boundary [28]. The degrees of the growth retardation vary at different grain boundaries [29]. Crystallographic orientations of the two neighboring grains across a grain boundary have been shown to affect the grain boundary resistance [30]. Over the past few decades, numerous methods [31-34] were proposed trying to quantify the resistance of the grain boundary toward short fatigue crack growth, for instance, by relating the growth rate change to the distance of the crack-tip from the nearest grain boundary [30, 35], which will be introduced in the section 1.3.

Since each individual grain boundary could present a high influence on the growth behavior of a short fatigue crack, grain size, namely the density of grain boundaries, should play an important role in controlling the growth behavior of a short fatigue crack, thereby the fatigue life of an alloy. A study of titanium by Tokaji et al. [36] indicates that

4

short fatigue cracks in coarse-grained Ti exhibits higher growth rates than those in fine-grained Ti. However, the work by Deng et al. [37] on GH4169 nickel-based superalloy dose not show substantial influences of grain size on the growth rate of short fatigue cracks. The work done by Zurek et al. [38] on an AA7076-T6 aluminum alloy shows an increase of crack growth rate with decrease of grain size, which they believe to be attributed to an intensified plasticity induced crack tip closure stress. So far, the mechanism for the influence of grain size on the growth behaviors of short fatigue cracks still remains unclear.

1.2.2 Grain orientation and micro-texture

The growth of a stage I fatigue crack occurs predominantly on the primary slip system within a grain [7]. Subsequently, short fatigue cracks prefer to propagate along certain crystallographic plane within one grain. Especially for planar slip alloys which either are hardened by shearable precipitates or present a high stacking fault energy, i.e. AA8090 Al-Li and AA2024-T3 alloys, such a crystallographic growth behavior of short fatigue cracks was observed even when crack length reached hundreds of microns [29]. Therefore, grain orientation becomes crucial in determining the crack plane orientation which potentially influences the nominal driving force of crack growth and the grain boundary resistance.

Crack plane deflection was usually observed in experiments [29, 39] when a short fatigue crack successfully passed a grain boundary. Depending on grain orientation, the selection of crack path in the neighboring grain could be different. Previously, the misorientation of the two adjacent grains was considered to dominate the crack plane orientation after a crack propagated across a grain boundary [12, 40]. It is generally believed that the larger

the misorientation between the two grains, the more pronounced deceleration of crack growth will be at the grain boundary. However, it cannot satisfactorily describe the geometry of crack plane deflection at the grain boundary, as the inclination angle between two crack planes across a grain boundary on surface [41] can be mistaken for the crack plane deflection which consists of both twist and tilt components of the deflection at the boundary. As defined in Figure 1.4, the crack plane in grain 1 intersects with the grain boundary between grain 1 and 2 on line *ac*. Similarly, the crack plane in the neighboring grain 2 also exhibits an intersecting line with the grain boundary on line *ab*. The angle between the two intersect lines, *ab* and *ac*, on the grain boundary, is defined as the twist angle (α). And the angle between the two intersecting line, *ad* and *ae*, on the sample surface is called the tilt angle (β). Zhai et al. [42] successfully distinguished the twist and tilt components of crack plane deflection from the inclination angle, and revealed their importance in determining the crack path across the grain boundary. As demonstrated in Figure 1.4, in order for the crack to propagate across the grain boundary from grain 1 into the adjacent grain 2 along its favorite slip plane, the area *abc* which is controlled by the twist angle α has to be fractured, leading to a significant increase of energy. The higher the twist angle on a grain boundary is, the larger the resistance from the grain boundary should be expected for the crack to propagate. Therefore, the crack will prefer to select a slip plane in grain 2 with the minimum twist angle at the boundary. This minimum twist angle criterion for the determination of the crack path across a grain boundary has been verified in several alloy systems, i.e. AA8090 Al-Li [42], AA2026 [43], Ni-based superalloy [39], Ti-based alloys [18] and Mg-based alloys [44] etc. Although the tilt angle and Schmid factor could also contribute to the grain boundary

6

resistance by reducing the driving force at the crack tip, the twist angle is the most dominant factor controlling the growth path of a short fatigue crack [29, 42].

Since grain orientation plays a critical role in determining the short fatigue crack path, micro-texture, namely the distribution of grain orientation, should be expected to affect statistically the grain boundary resistance against a short fatigue crack in an alloy. For the planar slip alloys with FCC crystal structure, like AA2026 T3 Al-Cu alloys [43] and nickel-based superalloys CMSX-4 [39], a short fatigue crack propagates predominantly along one of the four {111} planes. Different grain orientations/textures may lead to different selection of crack orientation among the four {111} slip planes, thereby resulting in different grain boundary resistance against short fatigue crack growth. In an Al-Cu alloy AA2524 [45], for example, a much slower fatigue crack propagation was obtained in the samples with dominant Goss and Cube grains, compared to those in samples with only Cube-grains and Cube+Brass grains, respectively. Similar conclusion was also drawn by Wu et al. [46] in an Al-Cu-Mg alloy that higher intensity of Goss texture was associated with a slower fatigue crack propagation due to greater crack deflections. Although many efforts have been previously made to quantify the microstructure influences on the growth behaviors of short fatigue cracks [47, 48], they are limited by the simulation scale or computational expense, the statistical effects of micro-texture have not been incorporated in the simulation of short crack growth in order to predict the fatigue life of an alloy.

1.2.3   Second phase particle

In high strength aluminum alloys, e.g. 2000 and 7000 series, fatigue crack initiation is usually associated with second phase particles on surface, i.e. β-phase (Al_7Cu_2Fe)

particles [13, 49]. Most of these particles are brittle, and may have been fractured prior to or during the cyclic loadings, thereby becoming the favorite fatigue crack nucleation sites in these alloys during cyclic loading. Early research work [20] indicated that cyclic straining can weaken the particle-matrix interface, which increased the susceptibility to de-bonding between particles and the matrix grain. However, detailed investigations were conducted in AA2024-T3 and AA7075-T6 aluminum alloys [13, 23, 50, 51], indicating that the vast majority of fatigue cracks were formed at pre-cracked particles which are already fractured during the prior deformation forming of the alloys, i.e. hot rolling or extrusion, before cyclic tests. Trantina and Barishpolsky [52] showed in their finite element analyses that, compared to a void, the crack driving force for a bonded and cracked inclusion was 15% higher, and for a debonded inclusion, it was 10% lower compared to a void. Similar conclusions were also made in steels by Melander et al. [53].

Although pre-cracked particles were determined as the predominant sites for fatigue crack nucleation, their population was very low compared to the overall particle population in the alloy. The population of those pre-cracked particles successfully nucleating fatigue cracks was even smaller. Kung and Fine [13] observed that most particles at which fatigue cracks are initiated are at the high end of the overall particle size distribution whose sizes are greater than 6 μm on the surface. Similar conclusion was also made by Laz and Hillberry [54]. However, this method cannot predict the fatigue crack growth occasionally from small pre-cracked particles observed in the experiments [55]. Murakami *et al.* [56] proposed a model in which the square root of the projected crack plane area $\sqrt{area}$, namely the cross-sectional area of the pre-fractured particles, was related to the nominal driving force of a short fatigue crack when extending from a

pre-cracked particle into the matrix. And a threshold value was introduced which was associated with the micro-hardness and $\sqrt{area}$ value of the particle. However, Merati et al. [50] showed that there was no clear correlation between particle size/area and fatigue life in an AA2024-T3 aluminum alloy, and suggested there must be other microstructural factors that played more crucial roles in initiating fatigue cracks. In addition to the parameters related to particle geometry, Liao's model [57, 58] also takes into account the Schmid/Taylor factor in their model to try to explain the scatter of short-crack growth. Crystal plasticity finite element analysis provides another solution to incorporating the crystallographic orientation effect in simulating short crack growth behaviors. Recently, McDowell's group [59] related the maximum plastic strain amplitude at crack front with the crack driving force. The maximum tangential stress [60] near the cracked particles was used to determine the driving force and direction of fatigue cracks nucleated at pre-fractured constituent particles in Hochhalter's work. However, despite of the high computational cost, the effects of particle size and the probabilistic prediction of fatigue life were not studied in their work.

Recently, Zhai's group [55] reported three types of fatigue cracks initiated from the pre-fractured constituent particles in AA2024-T3 Al-Cu alloys, as shown in Figure 1.3(a)-(c), namely type 1 non-propagating fatigue cracks; type 2 fatigue cracks which are arrested soon after extended into the matrix; and type 3 propagating fatigue cracks which successfully developed into long cracks. These three types of fatigue cracks were also found in a 0.45%-carbon steel where fatigue cracks were in initiated at pores [56]. With the help of the focused ion beam technique, the particle geometry beneath the sample surface can be revealed, i.e. particle cross-sections, as shown in Figure 1.3(d)-(f),

demonstrating a profound correlation between the particle thickness beneath the sample surface and the three different types of fatigue cracks (Figure 1.4.). From the particles whose thickness are smaller than 3μm, type 1 non-propagating fatigue cracks are most likely to be obtained. As increase of particle thickness to 5μm, type 2 cracks were observed to develop from these particles. And type 3 fatigue cracks were observed to propagate from those particles with thickness larger than 5μm. In order to quantitatively understand such a strong relationship between the particle thickness beneath the surface and the tree types of cracks, a three-dimensional microstructure-based model is required that can take into account the effects of irregular particle geometry and grain orientation, etc., in quantifying the growth behaviors of micro cracks in the pre-fractured particles.

1.3 Literature review on previous attempts in quantifying short fatigue crack growth

Grain boundaries have been recognized as the major microstructure barriers against short fatigue crack growth [7, 12, 61]. Over the past few decades, numerous attempts were made to quantify the influences of a grain boundary on short fatigue crack growth. This section reviews the main results from the previous studies.

1.3.1 Modified linear elastic fracture mechanics models

LEFM cannot explain the anomalous growth behaviors of short fatigue cracks, i.e. retardation of the growth rate at grain boundaries, growth of a short crack grow is faster than a long crack at the same nominal driving force, and no threshold value of the driving force for short crack growth, etc. Previously, modifications based on LEFM were made in attempts to take into account the effects of the local GBs on short fatigue crack growth

behaviors. For example, Chan and Lankford [30] suggested a crack tip plastic strain model to predict the growth behaviors of short fatigue cracks by assuming the plastic strain range at short crack tip was a power-law function of the stress intensity range, and introduced a crystallographic function to account for the resolved shear stresses in the cracked grain and its neighboring grain ahead of the crack tip in quantification of the driving force. As a result, crack growth deceleration at a GB could be attributed to the decrease in strain amplitude ahead of the crack tip close to the boundary, which is called the blocking effect of the slip band by the boundary. However, for the grains with similar orientations, little or no deceleration in growth rate was predicted by the model. Hobson [35] suggested an empirical model in which the distance from the crack-tip to the next microstructural barrier was considered in determining the crack growth rate, which is only valid within the first grain.

1.3.2 Bilby-Cottrell-Swinden models

Some models for simulation of short fatigue crack growth [31, 33, 62, 63] were previously developed based on Bilby-Cottrell-Swinden (BCS) theory [64], in which the plastic zone ahead of crack tip was represented by continuous distribution of non-slip dislocations. These models could analyze the retardation of fatigue crack growth caused by the reduced amount of slip ahead of the crack tip when the plastic zone was blocked by a GB. Sudden increase of the crack growth rate immediately after slip was transferred across the GB was observed ahead of the crack tip. Moreover, these models are 2-D in nature, though Navarro [31] and Wilkinson [63] considered an averaged Sachs factor describing the mean behavior of those grains along the crack front. Based on the 2-D model developed by Kunkler et al. [65], the model has further been extended to 3-D [66]

11

by replacing dislocation dipoles by a continuous distribution of dislocation loops [67] ahead of crack tip to describe the relative displacement of the crack flanks. However, due to the significant increase of complexity of the model, the work is only limited on the crack growth inside the first grain. A critical stress intensity was proposed in these models, having an inverse relation with the Schmid factor. Blocking the plastic zone in the vicinity of the crack tip by a GB could build up a pressure at the GB, which would trigger deformation across the GB, leading to crack growth across the GB once this critical stress intensity is reached. This model predicted that the crack plane should follow the slip plane with the maximum Schmid factor, i.e., the primary slip plane, in the neighboring grain. However it is practically not always true since a crack is sometimes observed to follow a slip plane which does not have the highest Schmid factor [29, 39].

1.3.3   Dislocation-based models

Based on discrete dislocation theory, models were developed directly relating crack propagation with the formation, movement and annihilation of dislocations ahead of a crack tip, and, therefore, the stress field at the crack tip could be presented using the dislocation dipoles [34, 48, 68-70]. These models showed a discrete behavior of crack growth below the fatigue crack growth threshold and were able to capture the retardation and arrest of cracks at GBs as a result of the irreversibility of dislocation movements due to the asymmetry of the shear stress field in front of a blunted crack. Although the models could provide a solid physical explanation for crack propagation based on the interactions of dislocations during cyclic loading, they were restricted to 2-D, and unable to take into account the 3-D effects of the local microstructure and texture on short fatigue crack growth, due to the complexity of discrete dislocation simulation.

1.3.4 Crystallographic models based on experiments

Based on the minimum twist angle criterion proposed by Zhai et al. [42, 71], a three-dimensional crystallographic model was established to account for the 3-D behaviors of short fatigue crack growth across GBs. The model qualitatively revealed that the grain boundary resistance was dominated by the twist component of crack deflection at a GB. The twist component was a function of both the orientations of the neighboring grains and the geometry of their boundary, thereby allowing incorporation of the 3-D effects of the local microstructure and texture into simulation of crack growth across GBs. Subsequently, for the first time, an experimental method was developed to determine the grain boundary resistance against crack growth in an AA2024-T351 alloy in author's group [72]. The reduction of growth rate ($\Delta da/dN$) after a crack tip interacted with a grain boundary was measured on sample surface, which was directly related to the grain boundary resistance (R) through:

$$\Delta \frac{da}{dN} = \left(\frac{da}{dN}\right)_{matrix} - \left(\frac{da}{dN}\right)_{GB} = C \cdot \Delta K^m - C \cdot (\Delta K - R)^m$$

$$R = \Delta K - \left(\Delta K^m - \Delta \frac{da}{dN}/C\right)^{1/m}$$

Where m and C are material constants. Knowing the orientation of each grain from electron backscatter diffraction (EBSD), the minimum twist angle at each grain boundary can be calculated if a flat grain boundary geometry was assumed perpendicular to the sample surface. In the studied Al-Cu alloy AA2024-T351, a pancake shaped grain structure was observed with grain size in L direction ($361 \mu m$) being much larger than it in T ($97 \mu m$) and S ($37 \mu m$) direction, as shown in Figure 1.6. Therefore, it is still

reasonable to assume the GBs are flat and perpendicular to the sample surface. The measured grain boundary resistance was then plotted against the calculated minimum twist angle on the same grain boundary, as shown in Figure 1.7 where the grain boundary resistance was found to be a Weibull-type of function of the minimum α. In addition to the resistance from the local GBs, this microstructure-based model also takes into account the driving force along the irregular crack front. In Chapter 3, the methodology of the model will be introduced in detail.

1.4 Rational and purpose of the study

As reviewed above on previous studies of metal fatigue, presently, we are still far from fully and quantitatively understanding the mechanisms for fatigue damage, especially the process of crack initiation and early growth which are very sensitive to the local microstructure and yet can consume up to 50-90% of the total fatigue life [7], though extensive studies have been carried out in the field of materials fatigue over more than 150 years [3, 12, 62]. In our modern society, fatigue damage can still cause catastrophic accidents of engineering structures, i.e. collapse of steel bridges, failure of aircrafts and explosion of pressure vessels, etc., which could lead to a huge economic impact and loss of lives. It becomes crucial to predict accurately the fatigue lives of load-bearing components of engineering structures, in order to prevent fatigue failure of engineering structures. Therefore, quantitatively understanding the anomalous growth behaviors of short fatigue cracks is overriding important for developing a microstructure-based model to quantify short fatigue crack growth, and consequently predict satisfactory the fatigue life of metallic materials in engineering structures.

14

In the current research work, both experimental and theoretical work is planned in order to achieve the following main objectives,

1. To quantitatively study the effects of particle geometry and micro-texture on the growth behaviors of micro-cracks in the pre-fractured constituent particles in planar slip alloys using FIB and EBSD.

2. To study the 3-D effects of microstructure, i.e. grain boundaries, and texture on the early growth behavior of short fatigue cracks in high strength aluminum alloys.

3. To develop a novel microstructure-based model in attempt to quantify short fatigue crack growth in planar slip alloys in three-dimensions, and provide more reliable probabilistic predictions of crack initiation rate from pre-fractured particles in surface and subsequently life distribution of short fatigue crack under various microstructures and textures.

1.5   Key results obtained

The novel microstructure-based model developed in this study was introduced in Chapter 3, which takes into account both nominal driving force and local resistance when simulating the growth of a short fatigue crack in planar slip alloys. The influences of both primary grain boundaries which intersect with surface plane and secondary grain boundaries which are completely buried beneath the sample surface were quantitatively illustrated. The experimental results in an Al-Li 8090 alloy was then used to validate the model. And good agreement of crack growth rate between the simulated and experimental data can only been achieved when the influences of both primary and secondary grain boundaries are considered in the model. The model also shows its

potentials in statistical prediction of the texture and grain size effects on short fatigue crack growth. Part of the results from the work "*A novel microstructure-based model validated experimentally for simulating short fatigue crack growth in three-dimensions in planar slip alloys*", are currently under review in Materials Science and Engineering A.

When quantifying the growth behavior of a short fatigue crack from second phase particles in surface, previous models usually simply assume the particle has a semi-circular or semi-elliptical shape [58]. This assumption completely ignores the influences of geometry and orientation of matrix/particle interface, which can potentially have significant impact in determining the growth behavior of short fatigue crack from the particle, similar to grain boundaries. However, the challenge still remains when taking into account the irregular shape of a particle. Therefore, in Chapter 4, an analytical expression of the driving force for an arbitrary shaped planar cracks in three dimension was firstly proposed which exhibits low computation expense and a relatively high accuracy when compared with the solutions from existing numerical methods.

In Chapter 5, the microstructure-based model was employed to quantitatively study the propagating behaviors of short fatigue cracks from pre-fractured constituent particles in high strength aluminum alloys by considering both the driving force along an arbitrary shaped short fatigue crack and the resistance from the particle/matrix interface. However, in the experiments, the particle shape can be highly irregular beneath the sample surface which is difficult to measure nondestructively. Therefore, micro-notches were introduced in the sample using focused ion beam (FIB) to mimic the initial crack at the pre-fractured particles in materials, because the size and geometry of these micro-notches can be well controlled using FIB, and the orientation of grain where they located can also be

manipulated. Three different types of fatigue cracks propagated from micro-notches were also observed in the experiments, namely type 1 non-propagating cracks; type 2 propagated but arrested cracks; and type 3 propagating fatigue cracks, which is consistent with the observations at the pre-fractured constituent particles in the AA2024-T351 alloy [55]. Given the microstructural parameters measured experimentally, the model was able to distinguish the three types of crack growth behavior from micro-notches which is consistent with the experimental observations.

The influences of different microstructure features, i.e. particle width on the surface and thickness beneath the surface, and grain orientation, on obtaining the different types of short fatigue crack from the pre-fractured particles were firstly quantitatively demonstrated in Chapter 6. For each matrix grain orientation, a crack-growth map predicting the type of short fatigue crack from the pre-fractured particle/micro-notch was given for different values of notch/particle thickness and width. And for given texture, namely the distribution of grain orientation, the probabilities of obtaining different types of fatigue crack for certain notch/particle size can be predicted by the model. In the AA2024-T351 aluminum alloy where rolling-type of texture was dominant, the model suggested that the particle thickness beneath the sample surface was the key parameter controlling the different types of fatigue crack growth behaviors from the pre-fractured constituent particles, which is consistent with statistical results in the experiments. The model can also give probabilistic predictions of short fatigue life for those type 3 propagating fatigue cracks by taking into account the influences of texture and grain size distribution in the materials.
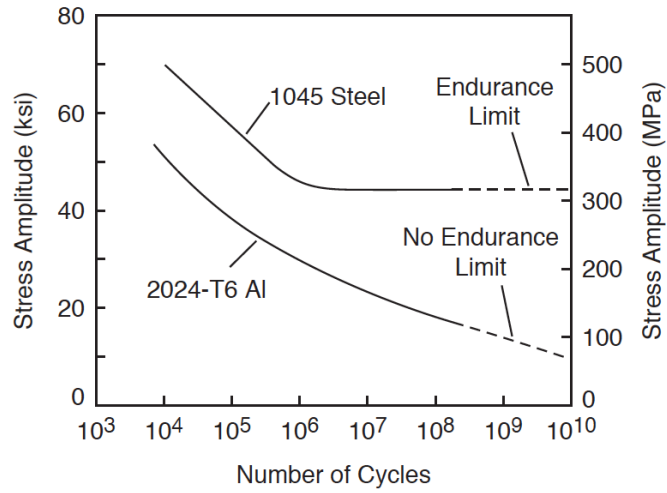
Figure 1.1. Examples of S-N curves for a steel and an aluminum alloy [5].
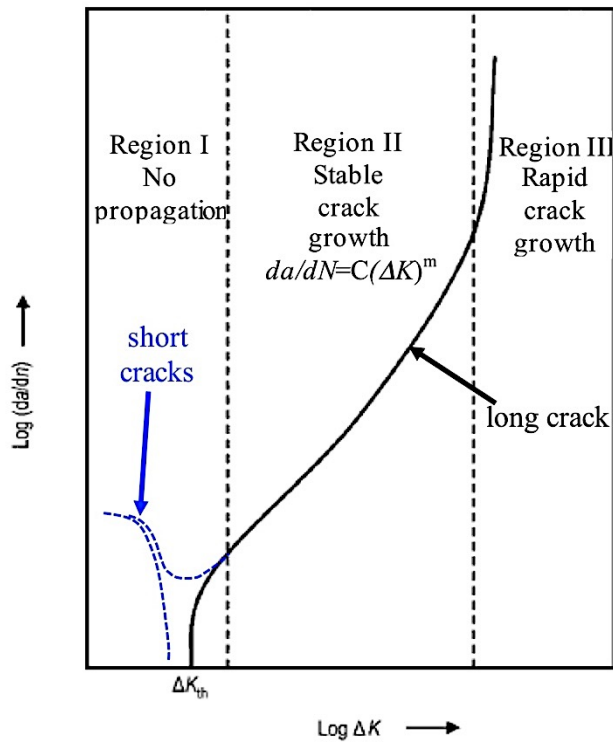
Figure 1.2. Demonstration of the typical fatigue crack growth behavior at constant amplitude of cyclic loading [7, 74].
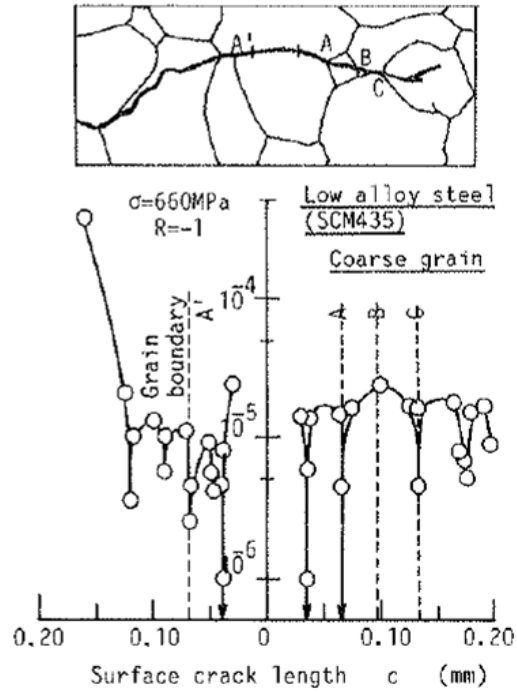
Figure 1.3. The scattered growth rate of short fatigue crack tips measured on the sample surface in a low alloy steel (SCM435) [28].
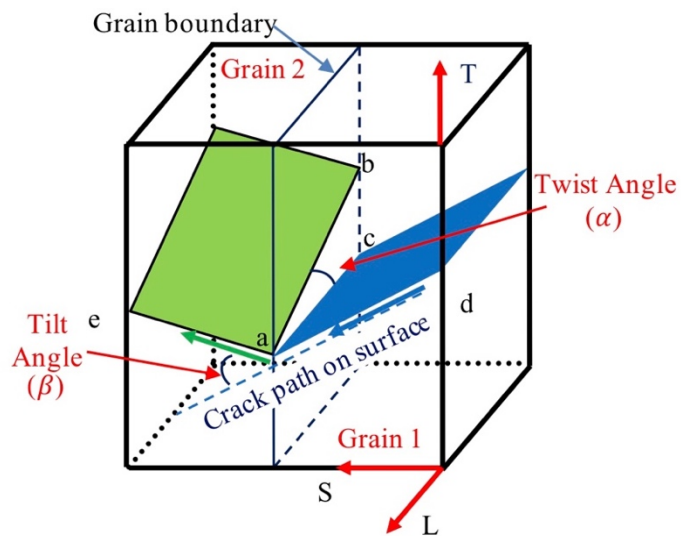
Figure 1.4. Schematic demonstration of twist and tilt angles when crack plane deflected at a grain boundary.
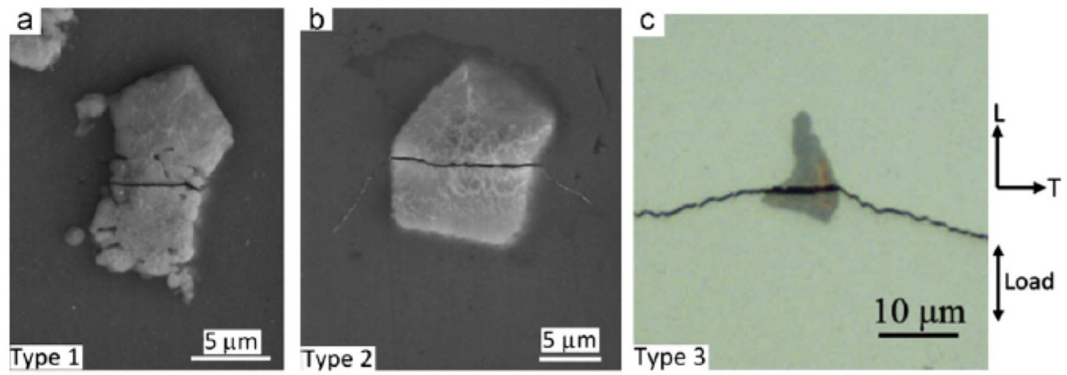
Cross-sectioning by Focused Ion Bean
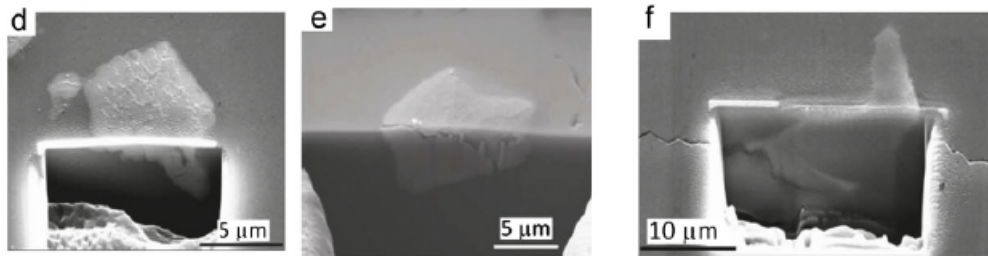
Figure 1.5. Fatigue cracks initiated from particles: (a) a type 1 non-propagating crack, (b) a type 2 fatigue crack, (c) a type 3 propagating crack, (d-f) the cross-sections of the particles shown in (a), (b) and (c), respectively. [55]
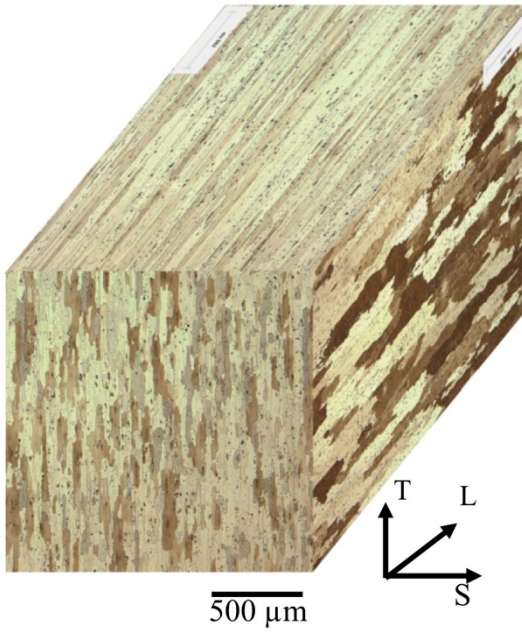
Figure 1.6. Microstructure of an AA2024-T351 Al-Cu alloy showing an elongated grain structure in L direction.
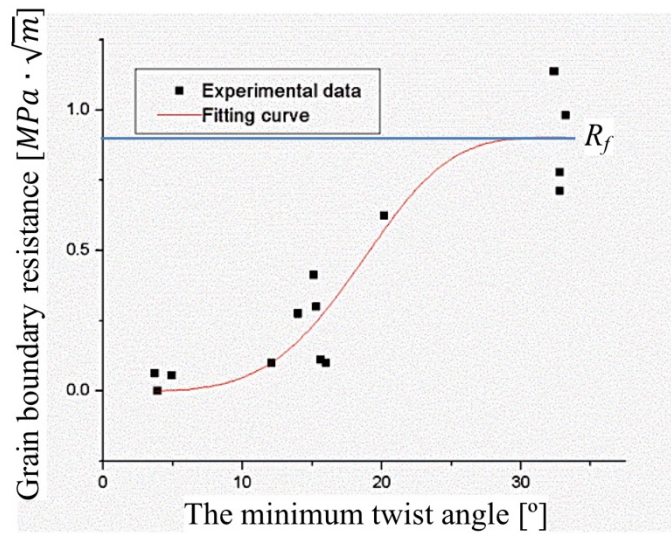
Figure 1.7. Resistance of grain boundary vs. the minimum twist angle on the same grain boundary [72].

CHAPTER 2   Experimental details and methodology

2.1   Selection of materials and sample preparations

2.1.1   Selection of materials

Two typical high-strength aluminum alloys, namely Al-Cu alloy AA2024 and Al-Li alloy AA8090 whose chemical composition were listed in Table 2.1, were selected for the model validation in the current work due to the following reasons:

(1) These two types of aluminum alloys are widely used in aircraft and spacecraft, due to their low density and superior balance of tensile strength, ductility and fatigue properties. For instance, the wing and fuselage structures under tension are usually made from AA2024, and the fuel and oxidizer tanks were made from Al-Li alloys in the recently launched SpaceX Falcon heavy [75].

(2) They both have high tendency of planar slip, and the propagation of short fatigue cracks prefers to follow certain crystallographic orientations within one grain during high cycle fatigue, which meet the assumptions of the crystallographic model introduced in section 1.3.4. Usually, planar slip occurs in metals or alloys with low stacking fault energy (SFE). A perfect dislocation may dissociate into two partial dislocations separated by stacking faults [76]. For example, in the materials with face centered cubic (FCC) crystal structure, like aluminum and copper, a perfect dislocation with burger's vector of $1/2[\bar{1}10]$ can dissociate into a pair of partial dislocations with burger's vector of $1/6[\bar{1}2\bar{1}]$ and $1/6[\bar{2}11]$.

Subsequently, during deformation, the gliding of a perfect dislocation is replaced by the moving of a leading and trailing partial dislocations. Studies [77] also indicate that pronounced short range order and precipitates with ordered atomic structure in alloys can also cause planar slip in FCC alloys. For instance, the dislocations in pure aluminum dose not exhibit a planar slip behavior due to its high stacking fault energy, while those in the Al-Li AA8090 alloys have high tendency of planar slip. And the change of slip mode in the Al-Li alloy was attributed to the formation of Al_3Li (δ') precipitates during age hardening, which are ordered but shearable [78, 79]. Similarly, in the Al-Cu AA2024 alloys, the high tendency of planar slip was the resultant of the formation of ordered precipitates of Al_2CuMg (s') phase [80, 81].

(3) The fatigue cracks initiated at different microstructure features in these two alloys. In the Al-Cu AA2024-T3 alloy, the constituent particles $AlCu_2Fe$ (β phase) on the L-T plane are the favorite fatigue crack nucleation sites because they already fractured along the plane perpendicular to the rolling direction (L) during hot rolling, as shown in Figure 2.1(a). Under the cyclic loading conditions selected in this work, instead of propagating along the particle/matrix interface, the short fatigue crack from the pre-fractured particles will extend into the matrix grain and propagate crystallographically. And the growth behaviors of such micro-cracks at the particles predominantly depend on the particle geometry and grain orientation. Therefore, AA2024-T3 alloy was selected to quantitative study the particle geometry and grain orientation effects on the fatigue crack initiation behaviors. However, the geometry of the particles can be highly irregular beneath the sample

surface and hard to measure non-destructively. In order to quantify their effects, micro-notches were fabricated to mimic the micro-crack at the constituent particles, so that the size and shape of the notch and the orientation of the grain where the notch located can be well controlled. It is worth mentioning that to ensure fatigue crack initiation from the micro-notches, instead of the pre-fractured particles, the notches were introduced on the T-S plane in the AA2024-T3 alloy on which the fractured plane in those particles is parallel to the load axis. While, on the L-S plane in the Al-Li AA8090 alloy, the fatigue cracks were always initiated along {100} planes that were perpendicular to the load axis (L-direction) [82], as shown in Figure 2.1(b). Therefore, the influences of particle size and shape on the initial crack geometry can be neglected, when studying the growth behavior of short fatigue cracks in this alloy.

2.1.2   Sample preparations

Prior to the fatigue tests, the sample surface under tensile loading during the fatigue test were firstly ground with SiC sand papers gritting from 240, 400, 600, 800 to 1200, then mechanically polished using alumina suspensions of 1μm, 0.3 μm to 0.05 μm in size. Finished polishing was conducted with a 50nm silica colloidal suspension, to remove the final layer of surface deformation introduced by the previous preparation. And for the electron backscatter diffraction (EBSD) measurement, Keller's etchant was used to etch the sample surface.

2.2 Mechanical test

2.2.1 Tensile test

The specimens for tensile test were prepared according to the ASTM standards [83], which has a gage length of 25.4mm and width of 6.35mm, as shown in Figure 2.2. For the AA2024-T351 aluminum alloy, the tensile test samples were cut along the T-direction (long transverse direction), whereas for the 8090 Al-Li alloy, the samples were cut along the L-direction (rolling direction) [42]. The tensile tests were conducted on an Instron 8800 servo-hydraulic testing machine at a constant crosshead speed of 1.2mm/min at room temperature in air, as shown in Figure 2.3. For each condition, two specimens were tested. And the yield strength σ_y was averaged over the two 0.2% offset yield stresses obtained from the two stress-strain curves. For the fatigue test, the selection of the applied stress levels was determined based on the measured tensile properties, especially the yield strength.

2.2.2 Four-point bend fatigue test

Compared to other commonly used fatigue tests, i.e. tension, four-point bend fatigue test owns several advantages: (1) easy sample preparation; (2) no special sample gripping required; (3) simply sample mounting and dismounting etc. However, it was found that depending on the sample geometry and the positions of the four support/loading rollers, more specifically, the load-span/specimen-thickness ratio (t/h) and the support-span/load-span ratio (L/t), as shown in Figure 2.5(b), the specimens can exhibit various fatigue behaviors due to non-uniform distribution of the tensile stress in the sample surface [84].

Zhai et al. [85] conducted systematic investigations to optimize the test geometry of the four-point bend fatigue test, which suggested the values of t/h and L/t between 1.2 and 1.5 and between 4 and 5, respectively, in order to obtain a relatively uniform stress distribution between the two loading rollers. And the nominal maximum stress σ_{nom} can be calculated by the beam theory of engineering mechanics

$$\sigma_{nom} = \frac{3P(L-t)}{wh^2}$$

where w is the specimen width and P is the load applied by one of the two loading rollers. For the four-point bend fatigue tests conducted in the current work, the samples geometry was selected with l=36.5mm, w=10mm and h=4.7mm. And the distances between two support and loading rollers were 30mm and 6mm, respectively.

A self-aligned rig for the four-point bend fatigue test [85] were used whose set-up was demonstrated in Figure 2.4 and 2.5(a). A ceramic hemisphere was used as a joint between the upper extension bar and the loading plate. Two sample pins were also designed to position the sample when mounting and prevent sample drifting during fatigue tests. Moreover, grooves were also fabricated on the upper and lower loading plates to position the support and loading rollers, respectively.

2.3   Crack/slip trace analysis

In order to quantitatively understand the growth of short fatigue cracks in three-dimensions, it is important to accurately identify the crystallographic orientation of the crack plane in each grain, especially in planar slip alloys. Therefore, in the current work, crack/slip trace analysis was performed, in which the slip traces of certain slip system on

26

the surface and/or cross-section planes were calculated and compared with the crack trace on the same plane, in order to identify the crack plane orientation. For planar slip alloys with FCC crystal structure, the short fatigue crack prefers to propagate along one of the {111} slip planes orientation in each grain. Therefore, in the following part, an example in FCC alloy was given on the determination of the slip traces of {111} orientations of a grain on certain plane (i.e. sample surface) in the specimen coordinate system:

(1) Transformation from crystal to specimen coordinate system: With specified the specimen and the crystal coordinate systems, an orientation is defined as "the position of the crystal coordinate system with respect to the specimen coordinate system," [86] which is

$$C_c = g \cdot C_S$$

where C_c and C_s are the crystal and specimen coordinate systems, respectively, and g is the rotation/orientation matrix. There are several methods to represent the rotation matrix. In the current study, the grain orientations were measured using EBSD in which three Euler angles [φ_1, Φ, φ_2] (Bunge definition) were used to represent a crystal orientation, as shown in Figure 2.6. And the rotation matrix can be can be represented using these three angles as

$$g = \begin{pmatrix} g_{11} & g_{12} & g_{13} \\ g_{21} & g_{22} & g_{23} \\ g_{31} & g_{32} & g_{33} \end{pmatrix}$$

in which
$$g_{11} = cos\varphi_1 cos\varphi_2 - sin\varphi_1 sin\varphi_2 cos\Phi$$

$$g_{12} = sin\varphi_1 cos\varphi_2 + cos\varphi_1 sin\varphi_2 cos\Phi$$

$$g_{13} = sin\varphi_2 sin\Phi$$

$$g_{21} = -cos\varphi_1 sin\varphi_2 - sin\varphi_1 cos\varphi_2 cos\Phi$$

$$g_{22} = -sin\varphi_1 sin\varphi_2 + cos\varphi_1 cos\varphi_2 cos\Phi$$

$$g_{23} = cos\varphi_2 sin\Phi$$

$$g_{31} = sin\varphi_1 sin\Phi$$

$$g_{32} = -cos\varphi_1 sin\Phi$$

$$g_{33} = cos\Phi$$

Therefore, the {111} orientations in grain A with Euler angles [φ_1, Φ, φ_2] can be represented in the specimen coordinate system as $C_s = g^{-1} \cdot C_c$.

(2) Calculation of the intersecting line between the slip plane and certain specimen plane: Knowing the slip plane orientations in the specimen coordinate system, C_s, their slip traces on certain specimen plane S_s, i.e. sample surface, can be calculated through cross product between C_s and S_s.

(3) Comparison between the slip traces and crack trace on the same specimen plane: Take sample surface for example, a fatigue crack will intersect with the sample surface, leaving crack trace on the surface. And crack plane orientation can be identified through comparison between the crack trace and the four calculated slip traces of {111} orientations in the same grain on sample surface. In some cases, the crack trace may be parallel to more than one {111} orientations, i.e. the example shown in Figure 5.5, therefore, to obtain an unambiguous crack plane

orientation, the crack/slip traces on another specimen plane need to be calculated and compared. In the current work, the cross-sectioning plane perpendicular to the sample surface was selected. And the crack trace on the cross-sectioning plane was revealed using focused ion beam.

2.4   Focused ion beam imaging, micromachining and deposition

Instead of electrons which are used in scanning electron microscopes (SEM) and transmission electron microscopes (TEM), a finely focused beam of ions was used in focused ion beam (FIB) systems for high-spatial-resolution imaging at low beam currents and for site specific sputtering and milling at high beam currents. In most commercially available FIB systems, the liquid-metal ion type source (LMIS) is used. Among the different types of LMIS source, i.e. In, Bi, Sn and Au, a Ga-based blunt needle source was most widely used due to its low melting temperature of 30ºC, low volatility and low vapor pressure [87]. Before bombard on the sample surface, the extracted Ga^+ ions from the source need to travel through a series of lens and apertures to define and then focus the beam on the sample surface.

When energetic ion beam hit the surface of a solid sample, the loss of its kinetic energy mainly transfers to sputtering of neutral and ionized substrate atoms (this effect enables substrate milling), electron emission (this effect enable imaging, but may cause charging of the sample), displacement of atoms in the solid (induced damage) and emission of phonons (heating) [88], as illustrated in Figure 2.7. Among these signals, the emitted electrons, referred to as ion-induced secondary electrons (ISEs), are collected by the detector for ISE imaging in FIB system, which not only exhibits contrast due to surface

29

topography and materials difference (similar to the secondary electron imaging in SEM), but also delivers strong channeling contrast from crystal orientation [87].

One of the major applications of FIB system is local and precise removal of sample material, namely micromachining, using high ion current beam. The interaction of the accelerated Ga+ ion beam with the sample material results in a physical sputtering of the sample material and an arbitrary shape can be etched. The sputtering yield and effective etch rate can be drastically different for various sample materials, accelerating voltage, angle of incidence, scanning style and redeposition etc. For instance, for 20keV Ga^+ ions, the sputtering yield (atom/ion) is 1.87 for silicon, while it is 2.98 for aluminum [88]. To speed up the etching rate, an etching gas can be introduced to the working chamber, which is referred to as gas-assisted etching (GAE). For example, the introduction of Cl_2 GAE gas would lead to an enhancement factor of etch rate of 10 in silicon, and 10-20 in aluminum [88].

Depending on the type of injected gas, FIBs can also perform sit-specific chemical vapor deposition (CVD). Platinum (Pt) and tungsten (W) are the most common deposited metals in commercial FIB systems. A fine nozzle needs to be inserted first before it sprays the precursor gas, i.e. W(CO)6, on the target surface. Then the adsorbed precursor gas was decomposed by the incident ion beam, leaving a thin film of desired reaction product on the surface, i.e. W, and the by-product, i.e. CO, being removed through the vacuum system [87, 88]. Usually, layers of W will deposit on the desired microstructure features before milling to prevent potential damages beneath the surface due to high-voltage incident ion beam.

In the current study, the FIB was used to (a) reveal the three-dimension geometry of the constituent particles and the crack trace on the cross-sectioning plane beneath the sample surface, and (b) fabricate micro-notches in attempt to mimic the pre-fractured particles as fatigue crack nucleation sites in the alloy. The above-mentioned experiments were conducted in two dual-beam SEM-FIB systems which are Hitachi NB5000 and FEI Quanta 200-3D.

2.5   Modeling software

The microstructure-based model developed in the current work was established using MATLAB. One of the biggest advantages of MATLAB over other methods or languages is using the matrix as the basic data element, which makes matrix calculations easy to manipulate, for instance, when calculating the twist angle on a grain boundary plane (vector) with given rotation matrixes from the Euler angles. Moreover, the graphical output of MATLAB is optimized for interaction and convenient to make modifications. MATLAB also provides various functionalities allowing easy extension of the model with other applications. The algorithm and methodology regarding the current crystallographic model will be discussed in Chapter 3.

Table 2.1. Chemical composition of Al-Cu alloy AA2024 and Al-Li alloy AA8090 (wt%)

Name	Cu	Mg	Si	Fe	Mn	Zn	Ti	Cr	Zr	Li	Al
AA2024	4.1	1.4	0.43	0.45	0.43	<0.25	<0.15	<0.1	0.25	-	balance
AA8090	1.58	1.14	0.18	0.27	0.08	0.23	0.09	0.09	0.13	2.65	balance

(a)   (b)
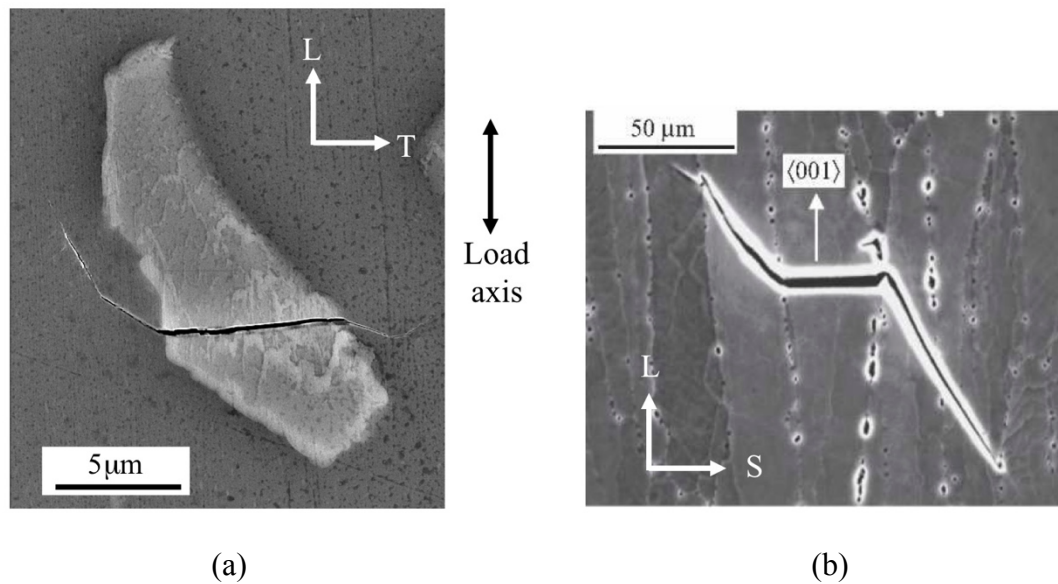
Figure 2.1. The typical fatigue crack initiation site on (a) the L-T plane in Al-Cu AA2024 alloy, and (b) the L-S plane in Al-Li AA8090 alloy.
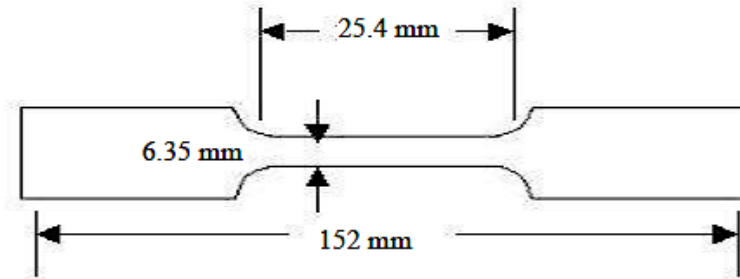
Figure 2.2. The geometry of specimens prepared for standard tension test for AA2024 and 8090 Al-Li alloys.

Figure 2.3. The Instron 8800 servo-hydraulic machine for tensile test.

Figure 2.4. The set-up of the four-point bend fatigue test rig in Instron 8800 machine.

(a)   (b)
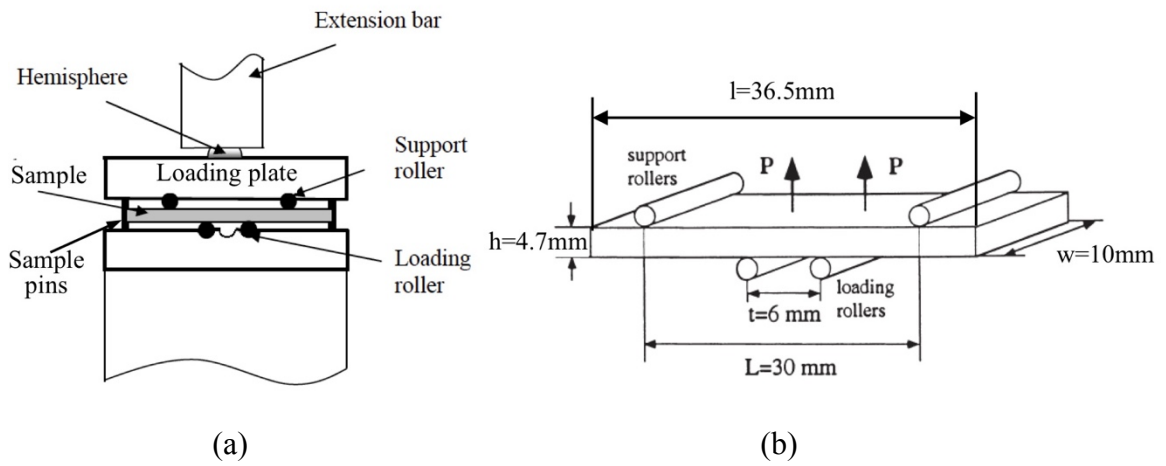
Figure 2.5. Schematic demonstration of (a) the set-up of four-point bend fatigue test, (b) sample geometry and the position of supporting and loading rollers on the samples [85].
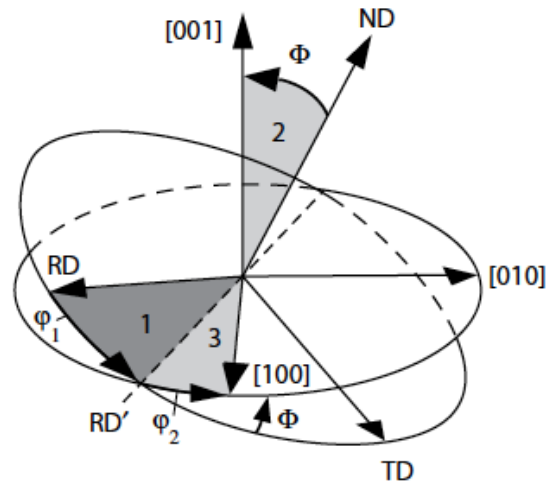
Figure 2.6. Demonstration the rotation between the specimen and crystal coordinate systems through the Euler angles φ_1, Φ, φ_2, in order 1, 2, 3 [86].
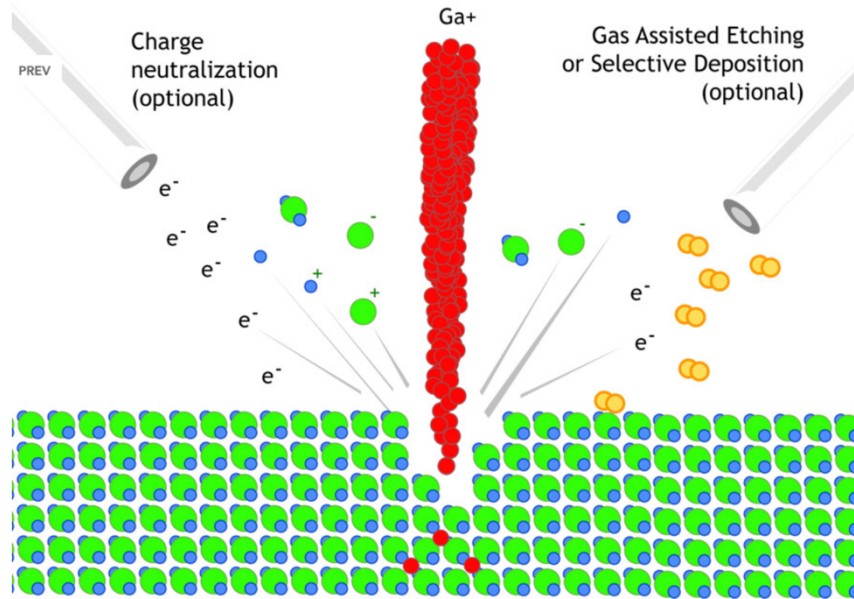
Figure 2.7. The interaction of Ga+ ion beam with sample material in FIB [89].

CHAPTER 3   A novel microstructure-based model validated experimentally for simulating short fatigue crack growth in three-dimensions in planar slip alloys

3.1. Introduction

It has been well recognized that growth of a short fatigue crack can consume a large portion of the high-cycle-fatigue (HCF) life, and is sensitive to the local microstructure in an engineering alloy, leading to its anomalous growth behaviors, such as marked scattering in growth rate measurement, growth under the driving force below the threshold for long cracks, and most of short cracks becoming non-propagating, etc. [7]. The mechanisms for these anomalous growth behaviors are still not quantitatively understood, though extensive work has been conducted on short fatigue cracks over last several decades [16-18]. It has been well recognized that grain boundaries (GBs) are the major microstructural barriers against short crack growth, often causing crack retardation or arrest in the alloys [11, 12, 61, 90]. Quantification of the GB effects becomes crucial for simulation of short crack growth and satisfactory prediction of the fatigue lives, especially in HCF to very high cycle fatigue (VHCF) regimes of the alloys.

Over the past few decades, numerous efforts have been made in attempts to understand the interactions of short fatigue cracks with GBs. Several quantitative models for simulating crack growth across a GB were proposed based on linear elastic fracture

mechanics (LEFM). For example, Chan and Lankford [30] introduced a crystallographic function $K(\Phi)$ which incorporated the resolved shear stresses in the cracked grain and its neighboring grain ahead of the crack-tip in quantification of the driving force, i.e., the plastic strain range, for short crack growth across the GB. Hobson [35] suggested an empirical model in which the distance from the crack-tip to the next microstructural barrier was considered in determining the crack growth rate.

Models for simulating short fatigue crack growth through a GB were also made [31, 33, 63, 91, 92] based on Bilby-Cottrell-Swinden theory which describes the plastic deformation zone near a crack-tip as an array of continuously distributed non-slip dislocations [64]. These models could demonstrate the constraint effect of the GB on the plastic zone in the vicinity of the crack tip, resulting in crack retardation at the GB. However, they did not directly take into account the effects of the local texture and its change across the GB on crack growth, though De los Rio et al. [92] incorporated an average Sachs factor over all the grains along the crack front.

Dislocation-based models [68-70, 93, 94] were also developed to quantitatively relate short crack propagation with the formation, movement and annihilation of dislocations ahead of a crack-tip. These models showed a discrete behavior of crack growth below the fatigue threshold and were able to capture retardation and arrest of a short fatigue crack at a GB as a result of irreversible dislocation motion due to the asymmetry of shear stress field in the vicinity of a blunted crack. The discrete dislocation models provided a physical explanation for crack propagation, based on the interactions of dislocations with the GB during cyclic loading. However, due to the complexity of these interactions in 3-D, these models could be applied to only one or two grains. Since all the models

mentioned above are 2-D in nature, they are unable to take into account the 3-D effects of the local microstructure and texture in simulating short crack growth. It is, therefore, still desirable to develop a more realistic microstructure-based model to quantify the 3-D effects of GBs on short fatigue crack growth.

Zhai *et al.* [42, 71] have identified that the twist angle α of crack plane deflection at a GB is the key parameter controlling the growth behavior of a short fatigue crack across the GB in an Al-Li alloy, and proposed a minimum twist angle criterion for the selection of the short crack path in the neighboring grain in planar slip alloys. This crystallographic criterion has been verified in Al-Cu alloys [42, 71], cast Al and Mg alloys [44, 95], a Ni-based alloy [39] and a Ti-Al alloy [18]. Recently, an experimental method was developed in Zhai's group to measure the GB resistance against short fatigue crack growth, and revealed that the GB resistance was a Weibull-type function of the minimum twist angle at the GB in AA2024 T351 Al alloys [72]. The quantification of the GB resistance by the experiment method provides an opportunity to establish a microstructure-based model for simulating short fatigue crack growth in 3-D by taking into account both the driving force and local resistance along the crack front.

Recently, McDowell *et al.* [32, 47] used a fatigue indicator parameter (FIP), which was a function of both plastic shear strain and normal stress in the vicinity of a crack-tip, as a surrogate of the local driving force for fatigue crack growth in 3-D. Although their model could demonstrate the scattering of the crack growth rate, the model could hardly explain crack-arrest at GBs, texture effects on crack growth and the multi-site crack nucleation behaviors occurred in many engineering alloys, since the resistance at different GBs was assumed to be a constant in their model [23, 96, 97].

38

In this work, a novel microstructure-based model was established to quantify the growth behaviors of short fatigue cracks in 3-D by taking into account both the local driving force and resistance along the irregular shaped crack front. A naturally-occurred fatigue crack in 8090 Al-Li alloy was used to validate the model by comparing the experimentally measured and simulated crack growth rates on the sample surface. The model was capable of quantifying crack retardation and arrest at GBs, the effects of texture and grain size on crack growth.

3.2. Methodology

3.2.1. Stress intensity factor range for an asymmetric crack front

For the sake of simplicity, a surface short crack is often assumed to be a planar crack with semi-circular or semi-elliptical shape, so that its driving force (i.e., stress intensity factor range) under mode I loading could readily be quantified as a constant along its front [58, 98]. However, even if there is such a semi-circular crack, it could quickly be evolved into an irregular shape soon after it starts to propagate, due to heterogeneous distribution of microstructural barriers against crack growth along the crack front. The irregular shape of the crack results in non-uniform distribution of both driving force and resistance along the crack front, which has to be taken into consideration in simulation of short crack growth in 3-D.

In the current work, a tortuous crack front was projected on the plane perpendicular to the loading axis. And the driving force along this projected planar crack under mode I cyclic loadings was defined through introducing a reference semi-circle whose area is equivalent to the total fractured area (A_{area}) of the projected irregular shape crack, as

shown in Figure 3.1(a) where an irregular crack front and its reference semi-circle are illustrated in solid and dashed lines, respectively. For an asymmetric crack, the center of its reference circle was assumed as the arithmetic mean position of the crack front on the sample surface. The centroid point (C_x) for a polygon was used here to calculate the center of the reference circle:

$$C_x = \frac{1}{6A_{area}} \sum_{i=0}^{n-1} (x_i + x_{i+1})(x_i\, y_{i+1} - x_{i+1}\, y_i) \qquad \text{Eq. (3.1)}$$

where x_i and y_i represent the position of point i on the crack front in x and y-direction, respectively. C_x depends on the crack shape. The definition of the center of the reference circle is crucial in the current model for the determination of not only the driving force but also the dragging forces from the GBs on the crack front, which will be discussed in the next section of the paper.

In this work, the empirical equation proposed by Newman and Raju [99] to calculate the stress intensity factor (SIF) range for a semi-circular surface crack was used to calculate the SIF range, ΔK_{ref}, along the reference semi-circle,

$$\Delta K_{ref} = [1 + 0.1(1 - sin\theta)^2]1.04\Delta\sigma\sqrt{\pi r_{ref}/2.464}$$

$$= [1 + 0.1(1 - sin\theta)^2]0.592\Delta\sigma\sqrt{\pi\sqrt{A_{crack}}} \qquad \text{Eq. (3.2)}$$

where the radius of the reference circle, $r_{ref} = \sqrt{2A_{crack}/\pi}$, $\Delta\sigma$ is the range of the applied normal stress, and angle θ represents the angle between the radial line of point i on the crack front and the sample surface, ΔK_{ref} varies slightly with θ from the minimum value of $0.592\Delta\sigma\sqrt{\pi\sqrt{A_{crack}}}$ at the middle of semi-circle to the maximum value of

$0.651\Delta\sigma\sqrt{\pi\sqrt{A_{crack}}}$ at the crack tip on the surface where $\theta = 0°$. On the surface, Eq. (3.2)

is very close in value to the one, $\Delta K_{max} = 0.65\Delta\sigma\sqrt{\pi\sqrt{A_{area}}}$, proposed by Murakami [56]

for the maximum SIF range of a surface irregular shaped crack. Although Eq. (3.2) might

be regarded as the average driving force for the surface irregular shaped crack, the

variation in driving force due to irregularity of the crack front has to be quantitatively

described in order to simulate the growth behaviors of short fatigue cracks in 3-D.

In this work, the SIF range, ΔK_i, at point i on an irregular shaped crack front was

calculated as,

$$\Delta K_i = \Delta K_{ref,i} + \left(\Delta K_{ref,i} - B\Delta\sigma\sqrt{\pi r_i}\right) \qquad\qquad \text{Eq. (3.3)}$$

Where $\Delta K_{ref,i}$ calculated using Eq. (3.2) is the SIF range at point i' on the reference circle,

r_i the distance between the center O of the reference circle and point i (Figure 3.1(a)), and

$B = [1 + 0.1(1 - sin\theta)^2]0.66$. As shown in Figure 3.1(a), in a region where the crack

falls behind the reference circle, such as point i, the driving force, ΔK_i, computed using

Eq. (3.3) is larger than $\Delta K_{ref,i}$ (i.e., the average driving force), thereby the crack should

propagate relatively faster in this region. On the other hand, the crack in a region (such as

point h in Figure 3.1(a)) ahead of the reference circle is under a driving force less than

$\Delta K_{ref,i}$ and grows slower in a homogeneous and isotropic media. Figure 3.1(b)

demonstrates the distribution of the driving force along the irregular shaped crack front

shown in Figure 3.1(a), in comparison to that of the corresponding reference circle. The

larger the difference in distance between points i and i' or h and h', the greater the

difference between ΔK_i and $\Delta K_{ref,i}$ (Figure 3.1(b)). As a first-order approximation, Eq.

(3.3) could reasonably capture the non-uniform distribution of the driving force along an irregular shaped crack and be conveniently used in simulation of short crack growth in 3-D under cyclic loading for millions of cycles. An analytical equation is being currently developed by the authors of this paper to quantify the distribution of the driving force more accurately along irregular shaped crack fronts, especially in those with singular points.

3.2.2. Resistance along the short crack front

Recently, an experimental methodology has been developed by the authors of this paper to quantitatively measure the resistance of a GB to short fatigue crack growth [72]. In an AA2024 T351 alloy, it was found that the GB resistance ($R_{GB,j}(\alpha)$) was a Weibull-type function of the twist angle (α_j) of crack plane deflection across GB$_j$,

$$R_{GB,j}(\alpha) = R_f\{1 - exp[-(\alpha_j/\alpha_0)^n]\}$$ Eq. (3.4)

where R_f is the maximum possible resistance of GB_j, and α_0 and n the shape parameters. α_0 and n are material-dependent constants and can be determined experimentally. With Eq. (3.4), the resistance of each GB along the crack front can be quantitatively determined, when the orientations of the relevant grains and the crack paths in these grains are known. This allows incorporation of GBs with different resistance along the crack front in simulating fatigue crack growth in 3-D for the first time.

A GB with large resistance can impose a stronger retardation effect on its surrounding crack front, which also has to be taken into consideration in quantifying the growth behavior of the crack in 3-D. In this work, the total resistance (R_i) at point i on the crack front was calculated to be the summation of the dragging forces from all those GBs at

which the crack fell behind point i, since those GBs where the crack propagated ahead of point i could not contribute to the resistance at point i on the crack front. Therefore,

$$R_i = \sum_j^M F_{ij} \cdot R_{GB,j}(\alpha) \qquad \text{Eq. (3.5)}$$

where F_{ij} is an influence function of GB_j and M the total number of the GBs interacting with the crack and behind point i. In this work, F_{ij} was simply assumed to be a Gaussian function of distance, since the contribution of GB_j to the total resistance at point i should heavily depend on the distance, x_{ij}, between GB_j on the crack front and point i,

$$F_{ij} = \exp\left[-\left(\frac{x_{ij}}{D}\right)^2\right] \qquad \text{Eq. (3.6)}$$

where D is the Gauss parameter determining the effective zone size of GB_j. Further work may still need to be done to identify the other factors, such as the direction of point i relative to the GB, that might also affect F_{ij}, in order to improve the accuracy of the influence function in Eq. (3.5).

3.2.3. Simulation of short fatigue crack growth in 3-D

As shown in Figure 3.1(a), the 3-D tortuous crack front was projected the S-T plane which is perpendicular to the loading axis. The crack front was discretized by a series of radial lines (such as points i, $i+1$, …) with a separation angle of 0.5° from the center of the reference circle. The mid-point of a discretized section on the crack front was used to calculate ΔK_i and R_i of the section, and the effective driving force for the section was then given by,

$$\Delta K_{eff,i} = \Delta K_i - R_i \qquad \text{Eq. (3.7)}$$

When $\Delta K_{eff,i} \leq 0$, the crack at point i was non-propagating, otherwise, it became

propagating when $\Delta K_{eff,i} \geq 0$. This means that the short crack has to overcome the local

resistance (R_i) in order to further propagate, thereby providing the quantitative

explanation for short crack retardation and arrest often observed at GBs. On a

microscopic-scale in a high strength Al alloy, Paris' power-law could still be valid for

quantification of crack advancement at each point along the crack front, if $\Delta K_{eff,i}$ is used,

because the size of the plastic deformation zone in the vicinity of the crack tip is typically

within 2 μm, much smaller than the crack size (>10 μm) [100],

$$\Delta a_i = \int C\left(\Delta K_{eff,i}\right)^m dN \qquad\qquad \text{Eq. (3.8)}$$

where Δa_i is the propagation distance of point i on the crack front, C and m the material-

dependent constants, and N the number of loading cycles. Each point on the crack front

propagated in the direction normal to its discretized section on the crack front. Note that

Eq. (3.8) could still be valid for long cracks as R_i becomes a constant, i.e., the average

total resistance of the GBs over the crack length when the crack is long in size. The

constant value of R_i should be equivalent to the threshold (ΔK_{th}) for long crack growth in

an alloy. In other words, Eq. (3.8) could be regarded as a unified equation for both short

and long crack growth. As revealed earlier using EBSD by the authors of this paper, in a

high strength Al alloy the size of the plastic deformation zone in the vicinity of a short

fatigue crack was typically around 2 μm across, much smaller than the average grain size

(> 20 μm), i.e., the initial crack size. This satisfies the small yield requirement for Paris'

equation [16]. It was, therefore, reasonable to apply the micro-scale Paris' equation to

simulating the growth behaviors of short fatigue cracks in the high strength Al alloys.

Incorporation of R_i in $\Delta K_{eff,i}$ calculation allows consideration of the effects of the local microstructure and texture in simulation of crack growth in 3-D using Paris' equation in Eq. (3.8). This could help to quantitatively explain the anomalous growth behaviors of short fatigue cracks, observed previously [16], such as retardation and arrest at GBs, significant scattering in experimental crack growth rate curves, and dependence of local grain structure and texture, etc. [100], as discussed in details later in the paper.

3.3. Results and discussions

3.3.1. Simulation of anomalous growth behaviors of a short crack

The alloy studied in this work was a hot cross-rolled AA8090 Al-Li alloy plate which exhibited a pancake-shaped grain structure with an average grain size of $217\times176\times$ $26\ \mu m^3$ in rolling (L), transverse (T) and short transverse (S) directions, respectively [82]. As a result of the pan-cake shaped grain structure in the alloy, a digital microstructure of layered grains of $25\ \mu m$ in thickness was first used in the model developed in this work to simulate the 3-D growth behaviors of short fatigue cracks in the alloy, as shown in Figure 3.2(a) where the grain structure is sketched on T-S plane perpendicular to the load axis L. The GBs (dash lines in Figure 3.2(a)) are located symmetrically with respect to Y-axis. All the seven GBs on the left-hand side of the microstructure in Figure 3.2(a) were assumed to have the same twist angle of 7.4° for crack deflection, while those on the right-hand side were randomly assigned twist angles of 2.1°, 1.8°, 12.9°, 3.9°, 5.2° and 2.6° for GB1/2 (i.e., the boundary between grains 1 and 2), GB2/3, GB3/4, GB4/5, GB5/6, GB6/7 and GB7/8, respectively. An initial semi-circular crack with a diameter of 25 μm was assumed in grain 1 (G1) in the surface. The parameters used in the simulation are listed in Table 3.1 where the maximum applied cyclic stress is 50% yield strength

(492 MPa) of the alloy and coefficients C and m used in the modified Paris' equation were obtained from literature [101]. Note that C used in Paris' equation was assumed approximately to be one order of magnitude higher than that for long cracks, according to ref. [16].

The 3-D propagation process of the initial crack in G1 was simulated quantitatively using Eq. (3.8) on T-S plane in the digital microstructure in Figure 3.2(a). The cyclic loading and the alloy parameters used in the simulation are listed in Table 3.1. The simulated crack fronts with an interval of 3,500 cycles are plotted in solid lines together with the digital grain structure in Figure 3.2(a). As shown in Figure 3.2(a), the initial semi-circular crack quickly evolved into an asymmetric and irregular shape soon after it interacted with the first two GBs (GB1/2' and GB1/2) in the alloy. Its length on the surface and depth reached 357.3 μm and 151.4 μm respectively at 1.37×10^5 cycles. It is evident in Figure 3.2(a) that the crack was retarded at almost every GB that it interacted with, leading to a concave shape in the crack front around the GB. The most marked crack retardation was found to be at GB3/4 where the crack front significantly lagged behind due to the highest resistance resulting from the largest twist (12.9°) at the boundary among all the 14 GBs studied in the microstructure (Figure 3.2(a)). Consequently, the largest negative curvature of the crack front took place around GB3/4. At those GBs with smaller twist angles, e.g. GB1/2 and GB2/3 with twist angles of 2.1 and 1.8° respectively, the dragging effect on crack propagation appeared to be relatively insignificant, leading to minimal changes in curvature of the crack front around them (Figure 3.2(a)). In this work, the decrease rate of the crack growth rate (da/dN) at a GB, i.e., the decrease in growth rate across the GB divided by the growth rate just before the crack crosses the GB, was used to define crack

retardation at the GB. Figure 3.2(b) shows crack retardation on surface at each of the GBs (i.e., GBs 1/2', 2'/3', 3'/4', 4'/5', 5'/6', 6'/7', 7'/8') that the crack tip B encountered on the left side of the microstructure in Figure 3.2(a). Since the twist angles at these GBs were same (7.4°), the results shown in Figure 3.2(b) demonstrate that crack retardation at a GB is influenced by the crack length. The crack retardation at GB1/2' $x = 12.5$ μm (x is the distance from the center of the crack to tip B) was 73.2%, while it was reduced to 24.2% at GB7'/8' $x = 162.5$ μm (Fig. 2(b)). The differences in retardation between these GBs, as shown in Figure 3.2(b), demonstrate profoundly that the crack length is also an important factor affecting crack retardation at a GB, in addition to the resistance of the GB. The longer the crack, the smaller the retardation effect that the GB could cause, which is understandable since the longer the crack, the higher the ΔK_i, thereby giving rise to a higher $\Delta K_{eff;i}$ at the GB, according to Eq. (3.7), i.e., less influence from the GB on da/dN.

Figure 3.2(c, d) depict the simulated growth rates (da/dN) of the two crack-tips on the surface as functions of the number of loading cycles and ΔK_I, respectively. Note that ΔK_I was calculated by assuming the crack was in a semi-circular shape with the surface length being the diameter of the circle, similar as that commonly used in the experimental measurements on short crack growth, for comparison with the experimentally observed behaviors of short crack growth. It is evident in Figure 3.2(c, d) that each drop in *da/dN* curves occurred at the GB that the crack-tips encountered, and that the growth rate of the short crack was markedly scattering, consistent with those often reported in literature [16]. This demonstrated that the crack retardation at a GB was a function of both its resistance (i.e., the twist angle) and distance (Figure 3.2(c, d)). For example, the da/dN drops (1.8%,

0.6% and 2.5%) occurred at GBs1/2, 2/3 and 4/5 were very small because of the small twist angles (2.1°, 1.8°, and 3.9°, respectively) at these GBs, whereas it was substantially large (98.5%) at GB3/4 due to its large twist angle (12.9°) and relatively short distance (62.5 μm). Meanwhile, the drops occurring in the da/dN curve were gradually reduced with increase in crack length from GB1/2' to GB7'/8' (Figure 3.2(c)), same as that shown in Figure 3.2(b), though these GBs have the same twist angle. This is consistent with the previous experimental observation in a Ni-based superalloy that the cracks with a shorter length showed a much stronger retardation influence by grain boundaries on the crack growth rate [39]. However, the model used recently by Musinski and McDowell et al. [47] could only predict a constant value of growth rate decrease at GBs irrespective of their distances from the crack center, unable to account for the distance effect of a GB on crack retardation.

At GB1/2', the first GB the crack tip B passed, the crack growth rate was so small (< 1 Å per cycle, less than a Burgers vector per cycle), due to relatively high resistance at the boundary and short distance from the crack center, that the crack could be regarded as temporarily non-propagating as da/dN had to be larger than Burgers vector per cycle for the crack to grow. In the meantime, tip A could propagate across GB1/2 into the next grain (G2). ΔK_{ref} was gradually increased with increasing the total fractured area as a result of the crack tip A further propagating. Eventually it became sufficient to drive tip B forward across GB1/2'. This indicated that $\Delta K_{eff,i} \leq 0$ had to be valid all the way along the whole crack front for the crack to be fully arrested. Otherwise, the crack would continue to grow from the region where $\Delta K_{eff,i} > 0$, and gradually drive the rest of the crack front forward as the fractured area was increased. As shown in Figure 3.2(c, d),

crack tip B consequently took about 7×10^4 cycles to catch up with the reference circle in terms of da/dN, i.e., tip B suffered a prolonged retardation on surface because the GB1/2' continues to drag the crack front beneath the surface, resulting in a slow growth rate of tip B on surface. As the interacting point between the crack and GB1/2' moved further inside the alloy, the dragging effect by the GB was gradually reduced because of the distance effect of the GB, as shown in Figure 3.2(b). This, together with the increase in crack length, led to the recovery in growth rate of tip B on surface, as shown in Figure 3.2(c). These 3-D effects of the GB on crack retardation revealed by the model developed in this work are consistent with the experimental measurements on short fatigue growth across GBs in planar slip alloys, i.e. CMSX-4 [39] and mild steel [102]. Previously, they could hardly be explained quantitatively using a 2-D model, such as those by [31, 92].

3.3.2. Quantification of crack retardation and arrest by GBs

Assuming the resistance inside a grain is zero, from the micro-scale Paris' equation, the crack growth rates at a GB, $\left(\frac{da}{dN}\right)_{GB}$, and just before the crack impinging on the GB, $\left(\frac{da}{dN}\right)_{matrix}$, can expressed by,

$$\left(\frac{da}{dN}\right)_{GB} = C(\Delta K - R)^m \qquad \text{Eq. (3.9)}$$

$$\left(\frac{da}{dN}\right)_{matrix} = C(\Delta K)^m \qquad \text{Eq. (3.10)}$$

Combine Eqs. (3.9) and (3.10), the decrease rate in da/dN, i.e., the crack retardation, at the GB is derived as,

$$\Delta\left(\frac{da}{dN}\right) \Big/ \left(\frac{da}{dN}\right)_{matrix} = \left[\left(\frac{da}{dN}\right)_{matrix} - \left(\frac{da}{dN}\right)_{GB}\right] \Big/ \left(\frac{da}{dN}\right)_{matrix} = 1 - \left(1 - \frac{R}{\Delta K}\right)^m \text{Eq. (3.11)}$$

For simplicity, assuming that there are no other GBs affecting growth of the crack, and $\sqrt{r_{ref}} - \sqrt{r_i} \ll \sqrt{r_{ref}}$, then Eq. (3.3) is simplified as,

$$\Delta K = B\Delta\sigma \sqrt{\pi \sqrt{2A_{Crack}/\pi}}$$

Eq. (3.11) provides a quantitative relation of crack retardation at the GB with *m, R* and *ΔK*. Given the applied cyclic loading, Δσ, crack retardation for a crack tip on surface can be plotted as a function of $r_{ref} = \sqrt{2A_{crack}/\pi}$ at different *R*, as shown in Figure 3.3 where Δσ = 246 MPa, and *R* = 0.2, 0.44, 0.9 and 1.5 $MPa\sqrt{m}$, separately,. Figure 3.3 profoundly demonstrates that the crack retardation caused by a GB is a function of both *R* and crack size under cyclic loading. At a fixed crack size, the higher the GB resistance R, the greater the crack retardation the GB could cause. For a constant GB resistance *R*, crack retardation at the GB is decreased as increase in crack size.

Assume that crack arrest occurs when da/dN ≤ *b* per cycle (*b* is the Burger's vector) at a GB. The critical SIF range, ΔK_c for crack arrest can be obtained from Eq. (3.9),

$$\Delta K_c = R + \left(\frac{b}{c}\right)^{\frac{1}{m}} = 1.292\Delta\sigma \sqrt{\pi\sqrt{A_{crack}}} \qquad \text{Eq. (3.12)}$$

Where ΔK_c is the critical SIF range for da/dN = *b* at the GB with resistance of *R*. Combine Eqs. (3.11) and (3.12), one can obtain the critical crack retardation when crack arrest takes place at the GB,

$$\left[\left(\frac{da}{dN}\right)_{matrix} - \left(\frac{da}{dN}\right)_{GB}\right] \Big/ \left(\frac{da}{dN}\right)_{matrix} = 1 - \frac{b}{c}\left[R + \left(\frac{R}{c}\right)^{\frac{1}{m}}\right]^{-m} \qquad \text{Eq. (3.13)}$$

Eqs. (3.12) and (3.13) define the critical condition for crack arrest. From Eq. (3.12), one can extract the critical values of the radius of the reference circle, $r_{ref} = \sqrt{2A_{crack}/\pi}$, at different GB resistance and the fixed $\Delta\sigma$, and plot them in Figure 3.3. Take $R_{GB} = 0.44\,MPa\sqrt{m}$ for an example, the critical r_{ref} equals to 7 μm, which means the crack will be arrested at a GB with resistance of $0.44MPa\sqrt{m}$, if the fractured area is smaller than $0.5\pi 7^2 \approx 77\ \mu m^2$.

However, it is worth mentioning that this criterion is suitable for the case of only a single GB without the influence from any other GBs. As discussed earlier in the paper, for a short crack to be fully arrested, each point along the crack front needs to be arrested. Continuous growth in any parts of the crack would eventually help to overcome the barriers that stop the crack locally, since the driving force is increased by increasing the cracked area due to the growth in parts of the crack front. Interactions between neighboring GBs as expressed in Eq. (3.5) could also affect crack growth, which needs to be taken into account in simulating the growth behavior at each point along the crack front.

3.3.3. The effects of secondary GBs beneath surface

In addition to the primary GBs as shown in the microstructure in Figure 3.2(a), the alloy studied in this work also exhibited secondary GBs that were oriented roughly perpendicular to the primary GBs due to the existence of fine recrystallized grains in the vicinity of some primary GBs. Consequently, a horizontal secondary GB (GB1/0) was placed inside G1 in the layered grain structure in Figure 3.2(a), as shown in Figure 3.4(a), in order to quantify the effects of the secondary GBs on crack growth along the crack front. GB1/0 was 25 μm beneath the surface and had a twist angle of 15°. As shown in

Figure 3.4(a), the 3-D growth behavior of the short crack was subsequently simulated in the microstructure in Fig. 4(a) using Eq. (3.8) with the same parameters as used for the crack in Figure 3.2(a). It can be seen in Figure 3.4(a) that higher density of the crack front lines occurs around GB1/0 beneath the surface, indicating much stronger retardation around GB1/0, compared to the results without the secondary GB (Figure 3.2(a)). The shape of the crack front around GB1/0 was also significantly changed by the existence of GB1/0 (Figure 3.4(a)). The growth rate of crack tip B on surface from the simulated crack growth of the crack is plotted together with that without GB1/0 in Figure 3.4(b). It is evident in Figure 3.4(b) that the crack growth rate with GB1/0 was substantially lowered starting from 6×10^4 cycles when the crack began to interact with GB1/0, compared to that without the secondary GB. Because of the retardation by GB1/0, crack tip B reached each of the GBs on surface significantly later than that without GB1/0. For example, it was delayed by about 6,300 cycles for tip B to reach GB2'/3' because of GB1/0, relative to the case without GB1/0. The retardation on tip B on surface by GB1/0 continued until the crack front completely propagated through the entire GB1/0 beneath the surface. Subsequently, the crack growth behaviors in terms of da/dN recovered soon after complete passing through GB1/0. For example, the growth rate of tip B became the same (2 nm/cycle) as that without GB1/0 at GB3'/4', though it was delayed by about 15,000 cycles for tip B to arrive at GB3'/4'. The growth behavior of the crack was also simulated when GB1/0 was placed at 15 μm beneath the surface, and the results showed that the crack was fully arrested all the way through the crack front. This indicated that GB1/0 could fully stop the crack if it started interacting with the crack earlier when the crack was smaller in size, i.e., the driving force for the crack was not sufficiently high to

drive the crack forward. These 3-D effects of microstructure on short crack growth could be quantitatively understood, for the first time, using the model developed in this work. This could help to explain why many short fatigue cracks became non-propagating, as often observed in high strength Al alloys [55] [103]. This model is capable of simulating short fatigue crack growth in 3-D based on the microstructure, texture and applied cyclic loading in high strength Al alloys.

3.3.4. Validation of the model by experiments

The growth behavior of a naturally occurring short fatigue crack, measured previously on surface in an 8090 Al-Li alloy in four-point fatigue [29, 85], was used to validate the current model. Detailed description of the experiments, the analysis of the short fatigue crack path and the grain orientations can be found in the earlier papers [29, 85]. As illustrated in Figure 3.5(a), the short fatigue crack, initiated on a (100) plane which was perpendicular to the loading axis in G3 (due to the trace elements of Na and K in the alloy [85]), propagated predominantly in a crystallographic fashion and followed the {111} plane with the minimum twist angle at each GB [42]. Crack tip A was found to be temporarily arrested soon after propagating into G1, until tip B stopped at GB11/12 (Figure 3.5(a)). Subsequently, the crack plane of the arrested tip A was deflected inside G1 and started to propagate again. The growth rate was measured experimentally only from G7 to G12, and used to verify the results simulated using the current model in the same region on the surface of the alloy in this work.

3.3.4.1.Simulated crack propagation in the grain structure consisted of only primary GBs

Since the alloy had a pan-cake shaped grain structure, a simple layered grain structure similar to that in Figure 3.2(a) was first assumed in simulating the growth behavior of the

53

crack shown in Figure 3.5(a) without incorporating the secondary GBs in the microstructure, as shown in Figure 3.5(b). The sizes of the grains in S direction were same as measured on the sample surface (Figure 3.5(b)) and listed in Table 3.2. An initial semi-circular crack with a diameter same as the size of G3 was assumed existing in G3 in S-direction. Other parameters used in the model for simulating crack growth are listed in Table 3.1.

Knowing the grain orientations and loading condition, the crack path could be determined using the minimum twist angle criteria through each GB that the crack interacted with in the microstructure in Figure 3.5(b). Subsequently, the growth behavior of the crack was simulated in 3-D in the microstructure using Eq. (3.8), and the calculated crack fronts at loading cycles of 6000 apart were plotted on the T-S plane perpendicular to the load axis, before the crack length reached 36 μm on surface, in Figure 3.5(b). From the length of 36 μm on surface, the interval of crack fronts was reduced to 3000 cycles to better reveal the crack growth behaviors in detail. As shown in Figure 3.5(b), very densely populated crack front lines and prominently concave crack fronts around GB1/2 were simulated, indicating a strong dragging effect by GB1/2 on crack growth because of its relatively large twist angle of 10°. This was consistent with the experimental observation that significant retardation of tip A occurred at GB1/2 [29]. The model was also able to predict the arrest of crack-tip B at GB11/12 on the surface, as observed experimentally.

The simulated growth rate of crack tip B on the surface in the region from G7 to G12 was plotted vs. the number of cycles, together with that experimentally measured [29], in Figure 3.5(c). Although the drop in growth rate at GB8/10 was successfully captured by the model, no decrease in growth rate within G8 was predicted by the model, resulting in

earlier arrival of crack tip B at GB8/10 than the experimentally observed by 3,000 cycles. Moreover, it took a total of only 20,000 cycles for tip B to propagate across the entire G10 in the simulation, compared to the 37,000 cycles measured in the experiment. In order to better compare the growth behaviors of the crack theoretically simulated and experimentally observed in G11, the crack was assumed to propagate from GB10/11 on surface at the same load cycles (813,000 cycles) as experimentally measured. As shown in Figure 3.5(c), 15,000 cycles were approximately required for the crack tip to cross G11 in both the simulation and experiment. And a peak value of growth rate around 3.5 nm/cycle was also predicted by the model before the crack tip was arrested at GB11/12, close to that of 4.1 nm/cycle measured experimentally. Although the model was able to quantitatively demonstrate crack retardation at GBs with different resistance by considering only the primary GBs measured on the surface, a relatively large deviation between the experimental and theoretical results was still evident in Figure 3.5(c). With the microstructure consisting of only the primary GBs, the model could hardly capture the decreases in crack growth rate within some grains, especially the observed arrest of crack tip A on $(11\bar{1})$ plane inside G1, as experimentally observed (Figure 3.5(c)). The secondary GBs that linked between the primary GBs beneath the surface needed to be incorporated into the microstructure used in the model, in order to better simulate the growth behavior of the crack.

3.3.4.2.Simulated crack propagation in the grain structure with both primary and secondary GBs

Detailed analysis of the fracture surface of the crack shown in Figure 3.5(a) could reveal the 3-D grain structure (i.e., GB structure) beneath the surface, since crack plane was

deflected at almost every GB it interacted with on its path [29]. Figure 3.6(a) depicts the fracture surface inside G7, G8 and G10 of the fatigue crack in Figure 3.5(a). From the change in direction of the fracture steps from one grain to another, the boundaries between these grains could be identified in the fracture surface. It can be seen in Figure 3.6(a) that G8 turned out to be small in size with a secondary GB about 13 μm beneath the surface. It contained two parts, one was tilted by 40° toward G8 and the other horizontal. The minimum twist angle at GB8/10 was calculated as a function of GB tilt angle, as shown in Figure 3.6(b) where the twist angle is increased to 9.1° when GB8/10 was tilted by 40° toward G8. Due to relatively small dimension beneath the surface, G8 was completely fractured when the crack depth reached 20 μm in this region. As a result, GB7/10 became the GB interacting with the crack beyond G8. Similarly, the crack-plane deflection observed in G1 was also attributed to a secondary GB1/1' which was 10 μm beneath the surface and had a twist angle of 10° [29]. As shown in Figure 3.7(a), these secondary GBs were added to the microstructure used above in Figure 3.5(b) for simulation of crack growth in 3-D in Figure 3.5(a).

As shown in Figure 3.7(a), the crack propagation was consequently simulated in the microstructure with both the primary and secondary GBs. It is evident in Figure 3.7(a) that, due to the combined retardation effects from GB1/2 and GB1/1', crack tip A was fully arrested after propagating 4.1 μm along the $(11\bar{1})$ plane on surface in G1, which was reasonably consistent with the crack length of 5 μm experimentally measured from GB1/2 to the deflection point in G1 (Figure 3.5(a)), before the crack plane was deflected to the (111) plane in G1. As shown in Figure 3.5(b), the arrest of tip A inside G1 could not be predicted without considering the effect of secondary GB (GB1/1'), demonstrating

the importance of the 3-D effects of the microstructure on the growth behaviors of short fatigue cracks. After crack tip B propagated 5 μm on the surface in G8, the crack front beneath the surface started to intersect with GB7/10 which had a large resistance compared to GB7/8, leading to denser crack front lines at the triple point of grains 10, 8 and 7. Similarly, significant retardation occurred when the crack interacted with the tilted GB8/10, resulting in a significant decrease in growth rate near this region.

As shown in Figure 3.7(b), the simulated growth rate of crack tip B on surface was now in a reasonablely good agreement with the experimental results. In addition to the decreases in growth rate at GBs, the drops in growth rate observed inside G8 and G10 were also predicted by the model. They were attributed to the interaction of the crack front with the secondary GBs between G8 and G10 beneath the surface. A sudden increase in growth rate after the crack-tip entered G11 was also successfully captured, which was attributed to the breaking-through of the secondary GBs of G8 beneath the surface by the crack front. In the previous experiment, it was found that the crack-tip B branched at GB10/11, which consumed approximately 9,800 loading cycles. Currently, the model developed in this work could not predict the crack branching, though the crystallographic model proposed earlier by Zhai et al. [42] could explain the branching qualitatively. The delay in crack growth due to the branching was manually added to the simulated results, as shown in Figure 3.7(b).

The reasonable agreement shown in Figure 3.7 between the simulated and experimentally measured growth behaviors of the short crack could serve as validation of the microstructure-based model developed in this work for quantitative simulation of the growth behaviors of short fatigue cracks in 3-D. It also revealed that, in high strength Al

alloys, the 3-D growth of short cracks could still follow Paris' equation on a microscopic scale as long as Paris' equation is modified with addition of a resistance term [72], in contract to the traditional belief that Paris' equation was invalid for short cracks because of the breakdown of linear elastic fracture mechanic theory for short cracks. Both the local driving force and resistance have to be considered in calculating crack growth at each point along the crack front. The incorporation of the resistance at GBs and their dragging effects on the surrounding crack front into the present model played a key role in the success for quantifying the anomalous growth behaviors of the short crack in 3-D in the AA8090 Al-Li alloy (Figure 3.7(a,b)). This enabled to extend Paris' equation to the s hort crack regime in 3-D.

The method used in the model to quantify the driving force along the front of an irregular crack appeared to be effective in capturing the stress concentration due to change in curvature of the crack front, as evident in the ability of the model to simulate the anomalous growth behaviors of short fatigue cracks in 3-D (Figure 3.7(a,b)). Although numerical methods have previously been developed to quantify the SIF for an irregular shaped 3-D planar crack under monotonic loading [104] [105] [106] [107], they could hardly be applied to simulation of crack growth in 3-D under cyclic loading for millions of cycles, as it would be too time-consuming to compute the SIF along the irregular crack front using these methods every fraction of a load cycle for millions of cycles. For short cracks with more complex shapes, such as those with sharp corners (i.e., the points where the curvature is discontinuous) on the crack fronts, the method used in the present work might not be sufficiently accurate to describe the SIF of the cracks. An analytical expression for more accurate quantification of the SIFs for 3-D fatigue cracks might need

to be developed in order to quantify the growth behaviors of short cracks with complex shapes. This work is being under way in the authors' group and the results will form another paper to be published in future.

It was the first time that the anomalous behaviors of short crack growth previously reported [16] could be quantitatively explained in this work, as the model is able to simulate crack retardation and arrest at GBs as a function of GB resistance, distance and interaction, thereby the scatters in crack growth rate could be quantified (Figure 3.2(c,d)). It also provides the criterion for the arrest of a short crack in 3-D that the effective driving force ΔK_{eff} equals or less than zero everywhere along the crack front, otherwise, crack propagation in the region where $\Delta K_{eff} > 0$ could gradually help to overcome the barriers that stop crack growth in the other regions in the crack front. This explains why many short fatigue cracks often become non-propagating. The model developed in this work shows the potential for thorough and quantitative understanding of the 3-D growth behaviors of short fatigue cracks with regard to the microstructure and texture beneath the surface, which could lead to advancement of technologies for fatigue life prediction and alloy development.

3.4. Quantification of texture and grain size effects on short crack growth

To demonstrate the model's capabilities of quantifying the effects of texture and grain structure on the short crack growth in high strength Al alloys, simple layered grain structures without secondary GBs (Figure 3.8(a)) were used to possess different textures. Random, rolling and recrystallization textures, as shown in Table 3.3, were formed in the digital microstructure, respectively, by assigning the crystallographic orientation selected randomly from the orientation pool (in Table 3.3) of each of these textures to each grain

in the microstructure, respectively. Therefore, the three digital microstructures formed showed the same volume percentages of all the components in the textures made, as listed in Table 3.3, respectively. The growth behavior of a surface crack with the initial length equivalent to the thickness (40 μm) of the planar grain in the middle of the microstructure was simulated using the model. For each texture, the simulation was repeated 500 times to derive statistically valid growth behaviors of short fatigue cracks. For a better graphic presentation of the simulated results Figure 3.8(b) shows only 50 out of the 500 simulated crack growth curves of half crack length on surface vs. load cycles (i.e., *a-N* curves) in random texture.

It is evident in Figure 3.8(b) that the lives of the short cracks at the length of 400 μm on surface are scattered between 0.44×10^5 and 1.8×10^5 cycles, that they are distributed preferably around either 0.5×10^5 or 1.7×10^5 cycles, and that crack retardation (i.e., the crack length remains the same for a large number of cycles at GBs) occurs most significantly at the first GB the crack encounters. The crack retardation gradually became less significant at the subsequent GBs as the crack propagated further, which was consistent with the results discussed earlier in Figure 3.2. The bimodal distribution of short crack lives can be better illustrated in Figure 3.8(c) where the cumulative probabilities (CPs) of the crack life ($N_{200\mu m}$) at half surface length of 200 μm are plotted as a function of load cycle for random, rolling and recrystallization textures, respectively. Figure 3.8(c) demonstrates profoundly that the short crack life varies between 0.44×10^5 and 1.8×10^5 cycles, and that it prefers to distribute around 0.5×10^5 and 1.7×10^5 cycles, respectively, in all three different textures. The transition between the bimodal peaks was characteristic of the specific texture (Figure 3.8(c)). The life probability curves of both

rolling and recrystallization textures in the transition region were almost parallel to each other, but the transition occurred at a lower cumulative probability (CP) = 0.25 in the recrystallization texture than that of 0.47 in the rolling texture, i.e., a lesser probability for the crack to present a shorter life (around 0.5×10^5 cycles) and a higher chance to have a longer life (around 1.7×10^5 cycles) in the recrystallization texture than in the rolling texture. However, in the random texture, the transition was slower than those in the other two textures (Figure 3.8(c)). It was found that the "longer life peak" (around 1.7×10^5 cycles) was attributed to the stronger retardation effect at the 1st GB the crack encountered, since the recrystallization texture presented the highest statistic average twist angle of 21.6° at the 1st GB, compared to 14.1° and 11.5° for random and rolling textures, respectively. It was understandable that the 1st GB played an important role in determining the life of a short crack, since the driving force (ΔK) was smallest at the first GB among all the GBs the crack interacted with, because the size of the crack was shortest at the 1st GB, thereby the effective driving force, $\Delta K_{eff,i}$, was relatively more significantly dominated by the resistance R at the 1st GB (Eq. (3.7)). In other words, the life of the crack was relatively less dominated by R at the subsequent GBs away from the 1st GB.

The effects of grain structure and size on short crack growth were quantified using the model developed in this work. Three different types of layered grain structures (GSs) were made (Figure 3.8(a)), such as GS-I: grain thickness of 40 μm without secondary GBs, GS-II: grain thickness of 40 μm with secondary GBs, and GS-III: grain thickness of 25 μm without secondary GBs. As shown in Figure 3.8(a), only three secondary GBs were added surrounding the initial crack in GS-II, since a GB could only have a

significant effect on crack growth when the crack was very short. They were located at 50 μm beneath the surface in G1 where a surface crack was nucleated, 30 μm and 10 μm beneath the surface in G3 and G3', respectively. The life of an initial crack in G1 was subsequently quantified using the model developed in this work in each of these three GSs which were assigned a random texture. A maximum stress of 246 MPa, equivalent to 50% yield strength in an Al-Li 8090 alloy, was used in simulation. The simulation was repeated 500 times in each GS after the random texture was re-assigned each time.

Figure 3.8(d) shows the cumulative probabilities of the calculated short fatigue lives at a half surface length of 200 μm in the three different GSs, respectively. It can be seen in Figure 3.8(d) that the cumulative probability varies between 0 and 1 in GS-I, in contrast to 0 to 0.42 and 0 to 0.29 in GS-II and GS-III, respectively. In GS-I, short cracks could all reach the length of 400 μm on surface, but only 42% and 29% of the short cracks could become propagating cracks. In other words, 58% and 71% of the cracks were fully arrested before reaching 400 μm long on the surface in GS-II and GS-III, respectively. This profoundly revealed that secondary GBs and grain refinement could markedly retard short cracks, leading to a large percentage of crack arrest. Compared to the secondary GBs, grain refinement from 40 μm to 25 μm presented a greater retardation effect on short crack growth, as a higher percentage (71%) of crack arrest occurred and the range of the crack life was increased from 0.45×10^5-1.75×10^5 cycles to 0.64×10^5-2.55×10^5 cycles in GS-III. These results demonstrate that grain refinement is an effective method to enhance the fatigue life by retarding short cracks in an alloy. This also verified that GBs were the main barriers for short fatigue crack growth, thereby largely responsible for the occurrence of multisite crack nucleation. As discussed earlier in the paper in Figure

62

3.2, the earlier a short crack encounters a GB, the greater the retardation the GB could impose on the crack. The pronounced retardation effect by grain refinement was likely to be attributed to the early encounter of short cracks with the first GBs in GS-III, since a crack encountered the first GBs at the crack length of 25 μm in GSIII, compared to 40 μm in GS-I, though higher number density of GBs could also contribute to the crack retardation in GS-III.

The results in Figure 3.8(b-d) could hardly be observed by experiments without the assistance of the model developed in this work. This work demonstrated that the model was capable of quantitatively explaining the stochastic and anomalous growth behaviors of short fatigue cracks that had puzzled researchers for the last several decades in the field of materials fatigue. The model could take into account the effects of grain structure and texture in quantification of 3-D growth behaviors of short cracks.

3.5. Conclusions

- A microstructure-based model was developed to quantify the 3-D growth behaviors of short fatigue cracks by taking into account both the local driving force and resistance at each point along a crack front in a planar slip alloy. The local driving force ΔK_I was computed by incorporating the stress concentration effects due to the irregularity in shape on the crack front, while the local resistance R at a GB was quantified by taking into account the resistance of the GB and the dragging effects from the surrounding GBs at which the crack front fell behind relative to the crack front at the GB. The effective driving force ΔK_I-R was considered in a microscopic-scale Paris equation to quantify the growth rate at each point along the crack front beneath the free surface.

- The 3-D growth behaviors of a naturally-occurring short surface crack was simulated using the model, which led to the results consistent with those experimentally observed in an AA8090 Al-Li alloy. This indicated that the modified Paris' equation was still valid for describing the growth behaviors of short fatigue cracks as long as the local resistance was incorporated in the equation.

- Depending on the resistance and position of secondary GBs beneath the surface, a noticeable retarding effect on the surface crack-tip could be captured by the current model, which explained the growth rate drop within a grain as observed experimentally.

- The microstructure-based model was capable of quantifying the influence of microstructure and texture, such as primary and secondary GBs, different textures and grain size, etc., on the statistical growth behaviors of short fatigue cracks.

- It was found that the twist component of the crack plane at the first GB that a short crack encountered played a crucial role in determining the life of the crack. The smaller the twist component, the shorter the short crack life.

- There was a bimodal distribution in the life spectrum of short cracks in a planar slip alloy such as an AA8090 Al-Li alloy regardless of the texture in the alloy.

- The recrystallization texture could lead to a higher probability (about 70%) of longer lives of short cracks, compared to only 39% in a typical rolling texture and 50% in a random texture in the AA2024 T3 Al-Cu alloy.

- For the first time, the anomalous growth behaviors of short fatigue cracks, such as crack retardation and arrest at GBs, scattering in growth rate, microstructural and

texture effects, etc., could be quantitatively simulated with the model developed in this work.

- Grain refinement and secondary GBs could lead to pronounced crack retardation and high probabilities of crack arrest.

Table 3.1. Parameters used for simulating crack growth

$R_f\,[MPa\sqrt{m}]$	1.5	n	3.5	$\alpha_0[°]$	10
$C\,[m/cycle]$	1.83×10^{-9}	m	3	$D\,[\mu m]$	6
$\sigma_{max}\,[MPa]$	246	**Load ratio R**		0.1	

Table 3.2. Parameters used in reconstruction of the digital microstructure in Figure 3.5(a)

Grain no.	Grain sizes [μm]	Twist angles [°]	Grain no.	Grain sizes [μm]	Twist angles [°]
G1	32(S)-10 (T)	GB1/1'=10	G7	9.5 (S)	GB6/7=2
G2	20 (S)	GB2/1=10	G8	10 (S)	GB7/8=1.7
G3	14 (S)	GB3/2=0	G10	13 (S)	GB8/10=7.4
G5	7 (S)	GB3/5=2.5	G11	27 (S)	GB10/11=0.7
G6	4.5 (S)	GB5/6=2			GB11/12=29.4

Table 3.3. Volume fractions of texture components in simulated rolling- and recrystallization-type textures

Rolling-type	20% Brass	20% S	20% Copper	40% Random
Recrystallization-type	20% Cube	20% Goss	20% R-cube	40% Random
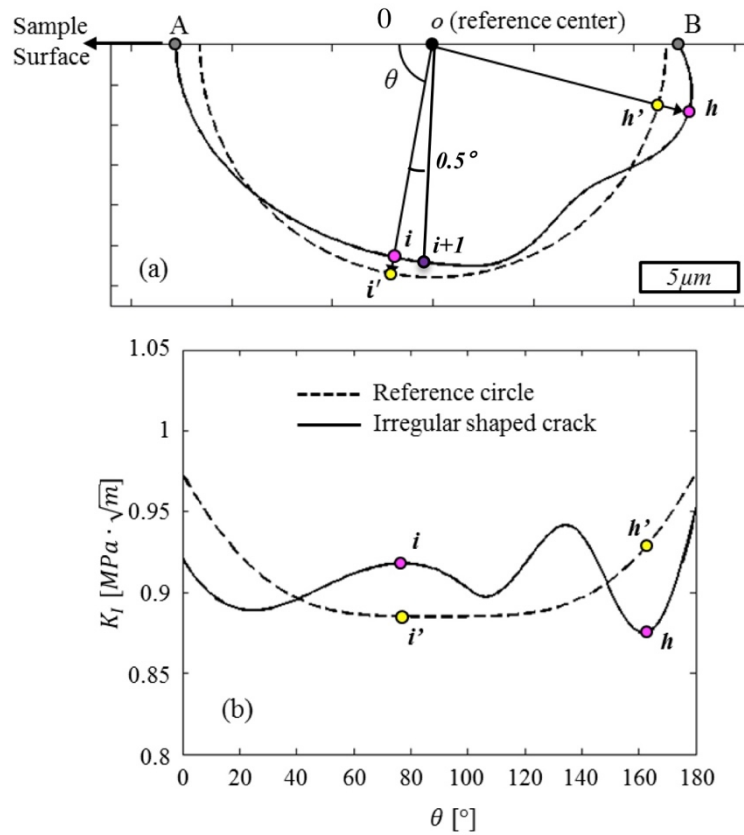
Figure 3.1. (a) Demonstration of an irregular shaped crack (solid line) and its reference circle (dashed line) beneath the surface, and (b) the corresponding distribution of driving force along the irregular shaped crack front (solid line) and its reference circle (dashed line).

(a)

(b)

(c)
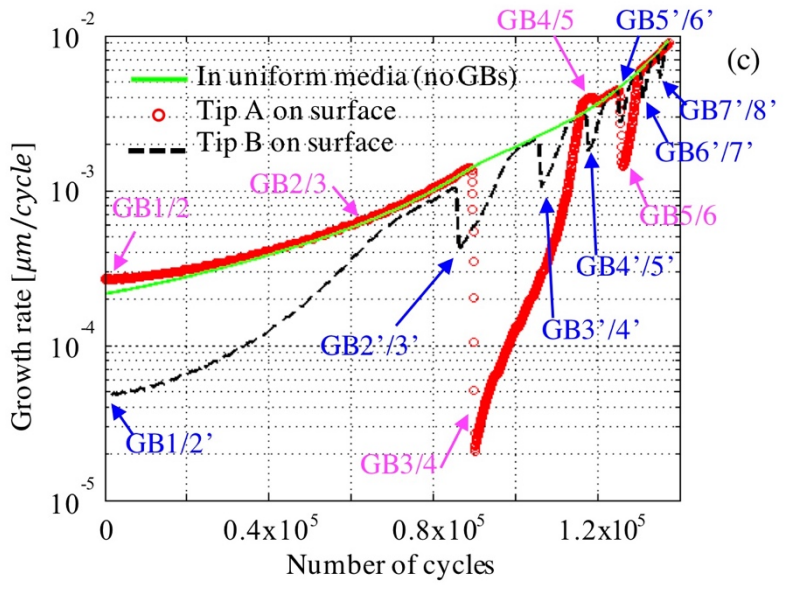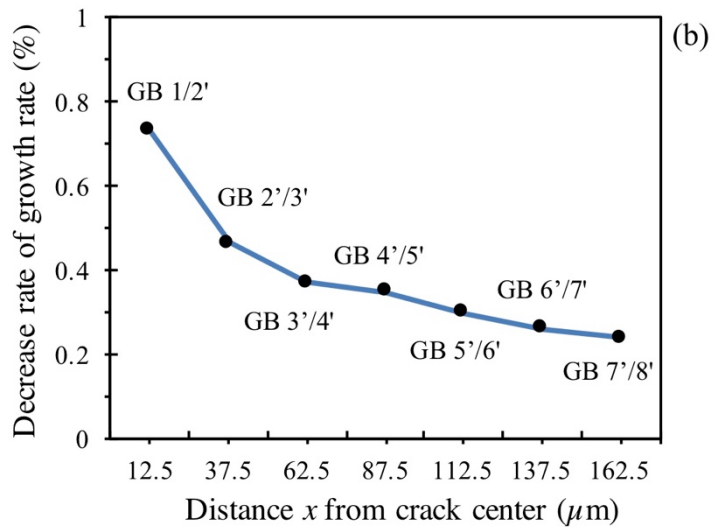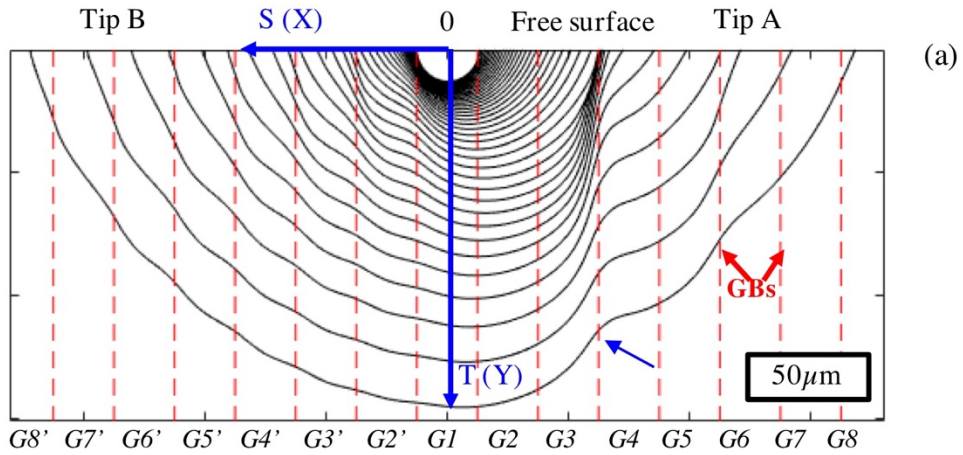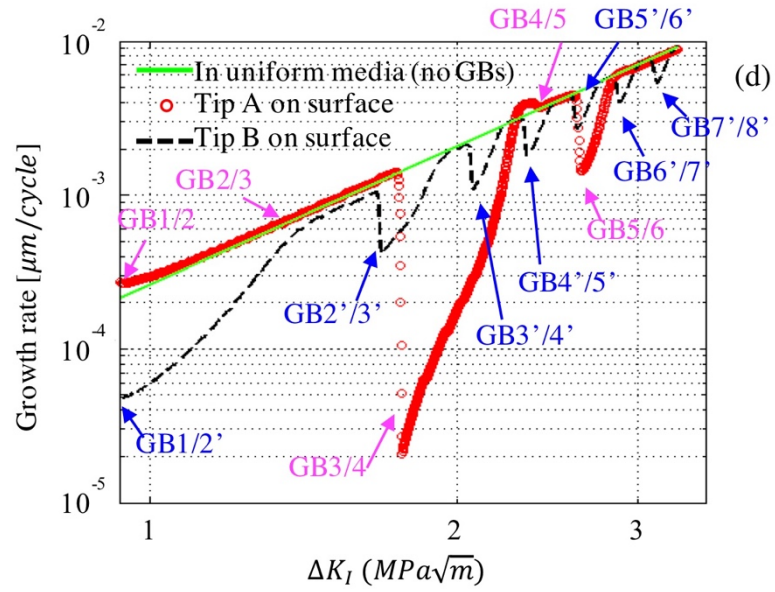
Figure 3.2. (a) The evolution of a short fatigue crack front (black lines) beneath the free surface in a layered grain structure (GBs were highlighted in dashed red lines) during cyclic loadings, (b) the percentage decrease of growth rate when tip B encountered GBs on surface, (c) and (d) the evolution of growth rate at the two crack tips on the surface over number of loading cycles and the stress intensity range, respectively.
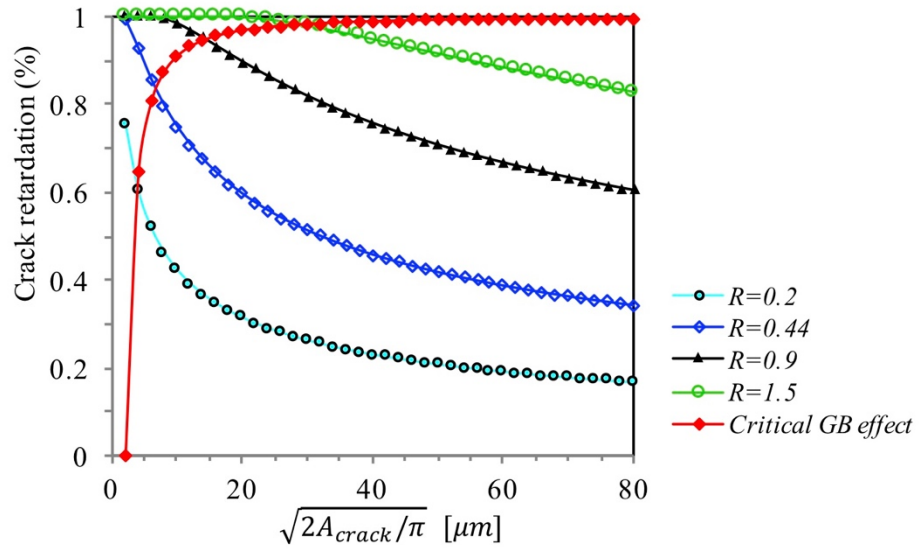
Figure 3.3. The crack retardation by a GB as a function of GB resistance (R) and radius of the reference circle $\left(\sqrt{2A_{crack}/\pi}\right)$. The maximum stress is 50% yield strength and stress ratio = 0.1.
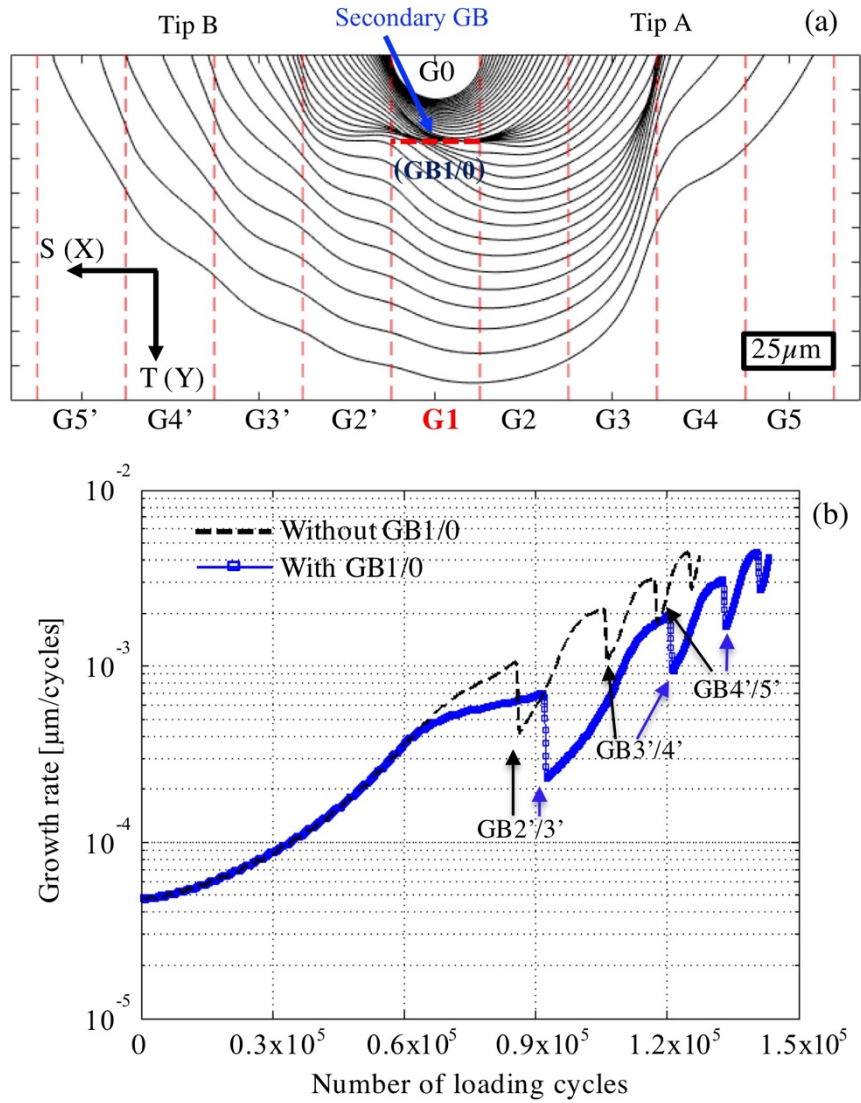
Figure 3.4. (a) The layered grain structure with a secondary GB, GB1/0, inside G0; and simulated fatigue crack fronts as iso-cycle lines in 3-D beneath surface; (b) The simulated growth rates of tip B of the short fatigue crack on surface with and without GB1/0.
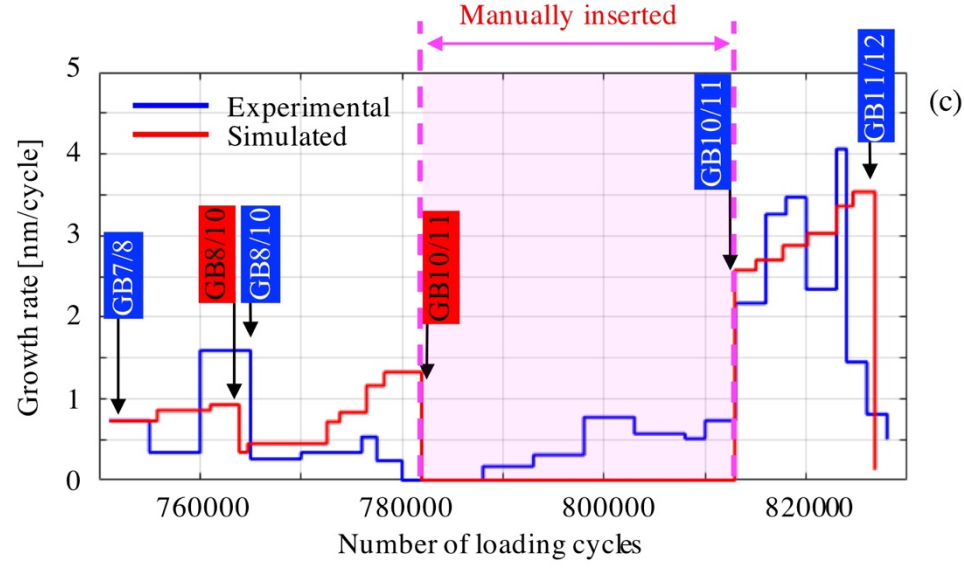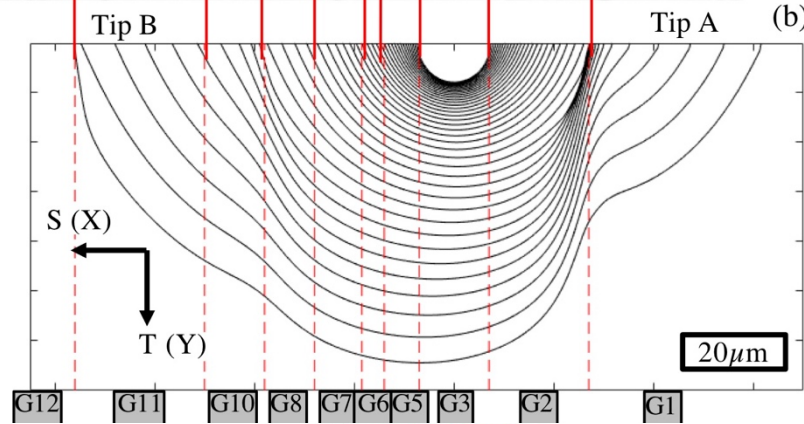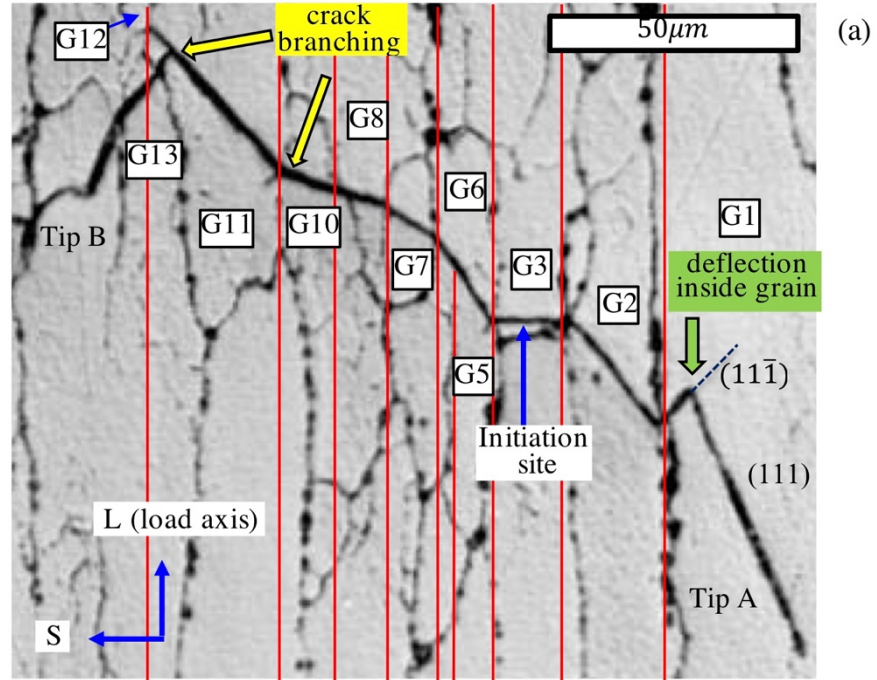
Figure 3.5. (a) The optical micrograph of AA8090 alloy after 915,000 cycles, (b) the simulated crack growth beneath the surface when a layered grain structure was assumed, and (c) the comparison of growth rate at crack tip B on surface between the experimentally measured (blue line) and simulated (red line) results. The number of loading cycles when the crack tip encountered GBs was indicated by blue arrows for the experiments and red arrows for the simulations.

(a)

(b)
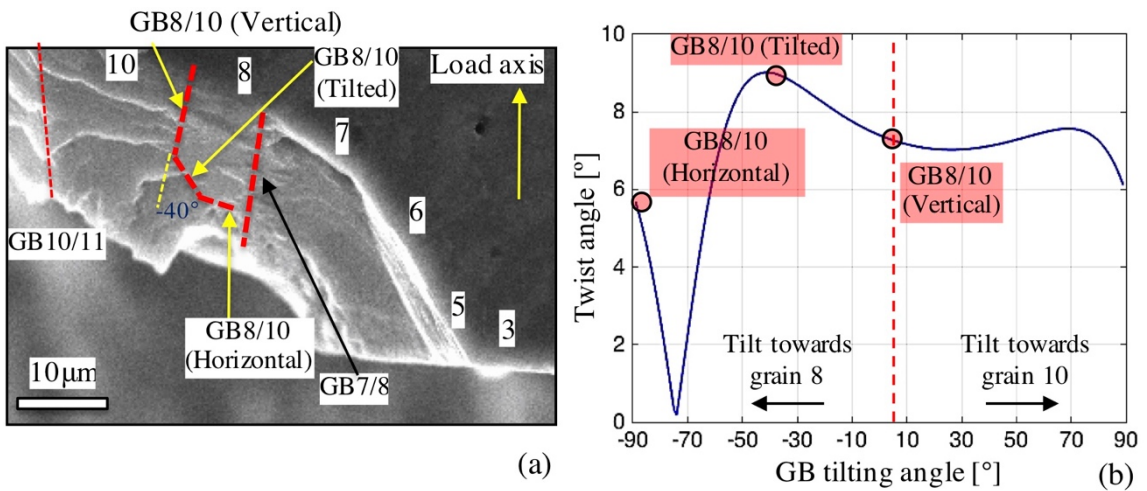
Figure 3.6. (a) the fracture surface of the fatigue crack shown in Fig. 5(a) around G8 highlighted using dashed lines, and (b) the calculated minimum twist angle on GB8/10 with different GB tilt angle.
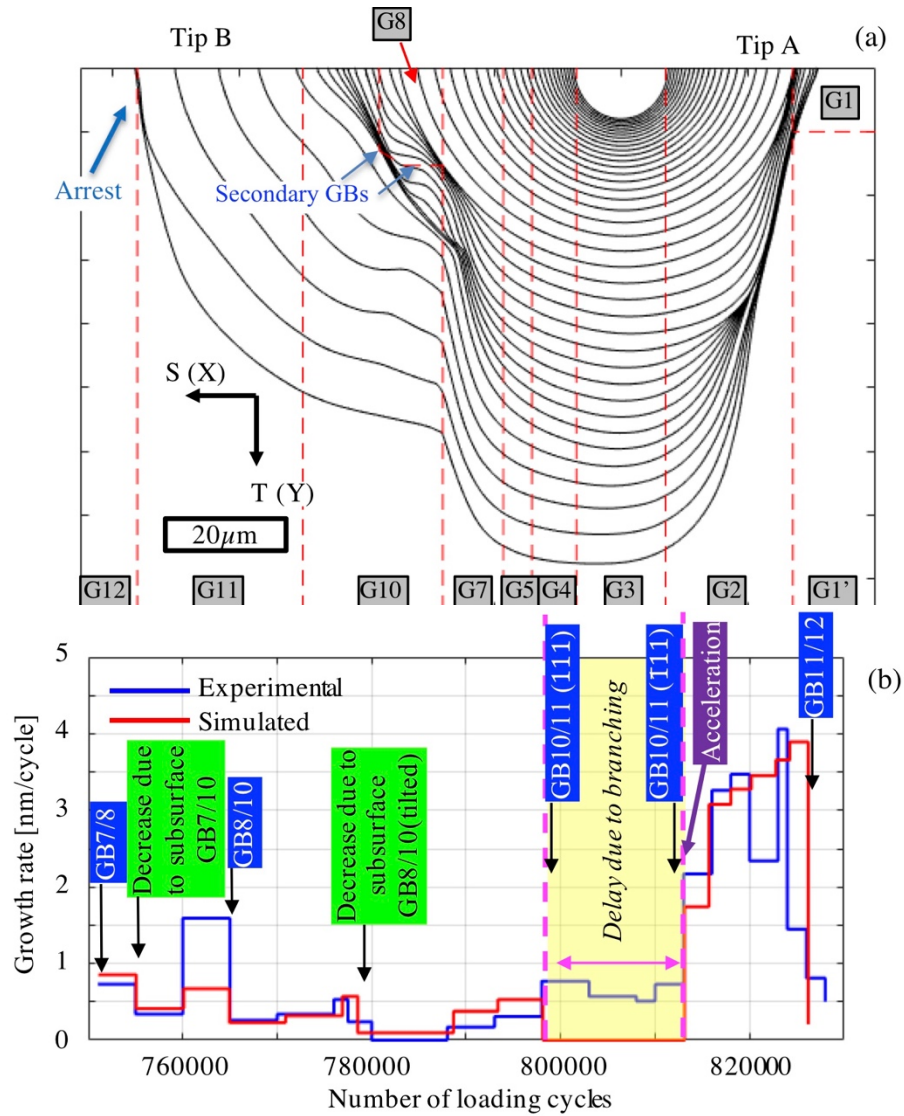
Figure 3.7. (a) consideration of the secondary GBs in G8 beneath the surface, and the simulated growth of the crack front beneath the surface; and (b) comparison of growth rate at the left crack tip on surface between simulated (red line) and experimentally measured (blue line) results.

(a)

(b)

(c)

(d)
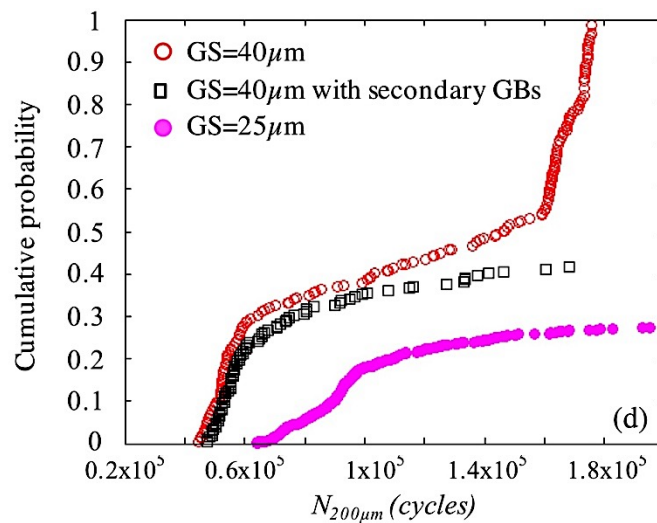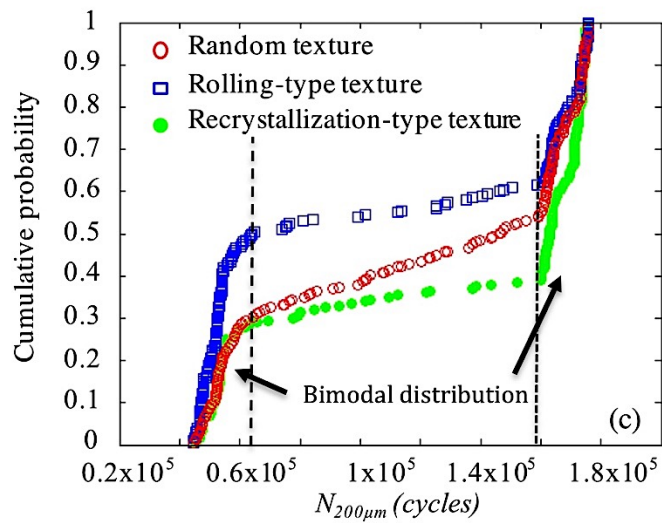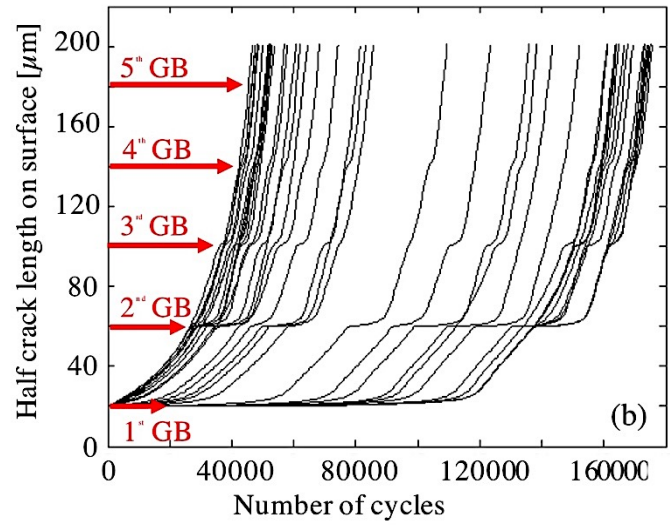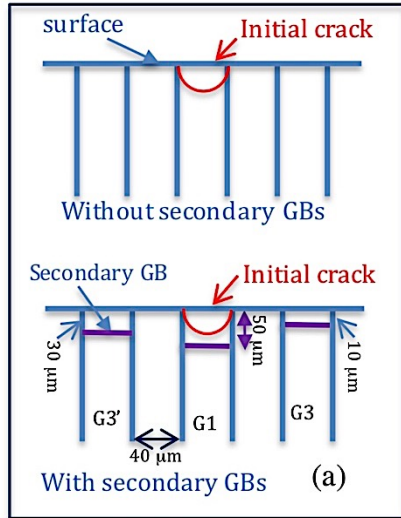
Figure 3.8. (a) Digital layered grain structures without and with secondary GBs; (b) Simulated half crack length on surface vs. number of loading cycles under layered grain structure with grain size of 40μm, (c) cumulative probability (CP) of $N_{200μm}$ for layered grain structure (GS = 40 μm) in random, the rolling-type, and the recrystallization-type of textures, and (d) the CP for layered grains of 40 μm thick with and without secondary GBs (GS = 40 μm), and for a layered grain structure of 25 μm in grain thickness.

CHAPTER 4   Quantification of the driving force for an arbitrary-shape planar fatigue crack in three-dimensions

4.1   Introduction

To extend the two-dimensional crack problem to a three-dimensional one, it becomes profoundly complex to calculate the stress intensity factors (SIF) along the crack front. For the cracks in circular and elliptical shapes in a homogeneous isotropic solid under a uniform tensile stress (mode I loading condition), their SIFs have been analytically solved [108, 109]. However, for cracks in more complex shapes than circles or ellipses, analytical solutions for their SIFs are unavailable. Integral equations have been formulated to quantify the SIF for such a crack in three-dimensions, which can be solved numerically. The SIF numerical solutions by a finite element method (FEM) [110] and a boundary element method (BEM) [111] have been found to be sufficiently accurate for cracks in arbitrary shapes. However, these methods are time-consuming, thereby not suitable for the applications under cyclic loading for millions of cycles, since the shape of the crack front evolves dynamically almost every loading cycle, leading to significant computational time and storage which limit the theoretical simulation, especially when trying to compute the stochastic behaviors of fatigue crack growth.

To simplify the calculation and lower the computational costs, the weight function methodology was firstly introduced by Bueckner [112] and Rice [105]. However, they also have certain drawback, for instance, a particular weight function solution is

necessary for each type of crack geometry, which limits its application to only simple regular crack geometries in three-dimensions. Oore and Burns [104] proposed a general form of weight function, known as the O-integral, which depends on the local geometry of the crack. Later on, Livieri et al. [107] further simplified the O-integral based on its first-order approximation. However, these methods could deliver K_I results with errors of up to 20% for simple geometries such as elliptical cracks with low aspect ratios [113].

Therefore, there is still a need to develop a more straightforward method which can be used to quantify promptly the SIF distribution along an irregular shape planar crack in three-dimensions under mode I loading with acceptable derivations/errors.

4.2   Theoretical Background

4.2.1   Derivation from Irwin's analytical solution for ellipse

For an embedded elliptical crack, the analytical solution of the stress intensity factor (K_I) under uniform tensile loading was well established by Irwin [6], which is

$$K_I = \frac{\sigma\sqrt{\pi a}}{E(k)} \left(\sin^2 \alpha + \frac{a^2}{c^2} \cos^2 \alpha \right)^{1/4} \qquad \text{Eq. (4.1)}$$

where $E(k)$ is the complete elliptic integral of the second kind,

$$k^2 = 1 - \left(\frac{a}{c}\right)^2$$

and angle α is represented in Figure 4.1.

Two parameters, r_{ref} and r'_{ref}, were introduced which were directly related to the total fractured area (A_{crack}) and the perimeter (C_{crack}) of the crack front, through

$$r_{ref} = \sqrt{A_{crack}/\pi} \qquad \text{Eq. (4.2)}$$

$$r'_{ref} = C_{crack}/2\pi \qquad \text{Eq. (4.3)}$$

For elliptical cracks $r_{ref} = \sqrt{ac}$ and $r'_{ref} = 2cE(k)/\pi$. If substitute angle α, elliptical parameters a and c with r_{ref}, r'_{ref} and $r(\theta)$ (distance from the ellipse boundary to the center), Eq. (4.1) can be rewritten as

$$K_I(\theta) = \frac{2\sigma}{\sqrt{\pi}} \cdot \frac{r_{ref}}{r'_{ref}} \cdot (a^2 + c^2 - r(\theta)^2)^{1/4} \qquad \text{Eq. (4.4)}$$

Detailed derivations can be found in the appendix. $a^2 + c^2$ can be further approximated using the perimeter of ellipse by

$$C_{crack} = 2\pi r'_{ref} \approx 2\pi \sqrt{\frac{a^2 + c^2}{2}} \qquad \text{Eq. (4.5)}$$

And Eq. (4.4) can be further simplified as:

$$K_I(\theta) = \frac{2\sigma}{\sqrt{\pi}} \cdot \frac{r_{ref}}{r'_{ref}} \cdot \left(p_1 \cdot r'_{ref}{}^2 - r(\theta)^2\right)^{1/4} \qquad \text{Eq. (4.6)}$$

For near elliptical-shaped crack, the parameter p_1 = 2. Good agreements of K_I for elliptical cracks between the Irwin's solution [6] and Eq. (4.6) were achieved over a relatively wide range of the aspect ratio, with average deviations of 0.035, 0.010, 0.005 and 0.020 for the aspect ratio of 0.2, 0.5, 1.5 and 3, respectively.

The expression of K_I in Eq. (4.6) generalized the solution in Eq. (4.1), and made it applicable for near-elliptical shaped cracks by relating to the total fractured area and perimeter of crack front through r_{ref} and r'_{ref}, respectively. No parametric equations are

required to describe the irregular crack front. Instead, discrete crack front can be considered, and the K_I of each discrete point on the crack front can be directly calculated using Eq. (4.6), knowing its distance to the crack center, $r(\theta)$. For those crack points falling behind which had smaller $r(\theta)$, a larger K_I according to Eq. (4.6) can be expected to accommodate the stress concentration at these points, whereas for the crack points moving ahead, a smaller K_I value is obtained. It is worth to note that the concept of centroid point was adapted here to define the center of an irregular shaped crack (x_c, y_c) through

$$x_c = \frac{1}{6A_{crack}} \sum_{i=0}^{n-1}(x_i + x_{i+1})(x_i y_{i+1} - x_{i+1} y_i)$$

$$y_c = \frac{1}{6A_{crack}} \sum_{i=0}^{n-1}(y_i + y_{i+1})(x_i y_{i+1} - x_{i+1} y_i)$$

An example of K_I distribution along an asymmetric crack front with half circular-half elliptical shape was demonstrated in Figure 4.2. Different from the coordinate center, (x_0, y_0), the position of the crack center was indicated as (x_c, y_c) in Figure 4.2(a). And the distance from crack front to the crack center was plotted in Figure 4.2(a), in which lowest distance was obtained around $\varphi = 65°$. Correspondingly, the highest K_I value according to Eq. (4.6) was achieved in this region, as shown in Figure 4.2(b). Compared to the solutions reported in literatures [106, 107] which were also illustrated in Figure 4.2(b), good agreements were obtained with average deviations of 0.017 from the Livieri's solution [107] and 0.016 from the Mastrojannis' solution [106].

4.2.2 Accommodation of large deviation from elliptical shape

For an irregular shaped crack with large deviation from elliptical shape, i.e. having flat boundary, concave curve and existence of singularities, the approximation of K_I using Eq. (4.6) may lead to large errors. For instance, for the square-like flaw illustrated in Figure 4.3(a) whose boundary follows $r(\theta) = a/(\cos^4 \theta + \sin^4 \theta)^{1/4}$, the K_I distribution obtained from Eq. (4.6) was plotted in red line in Figure 4.3(b). The highest and lowest value which are corresponding to the shortest and longest distance between the crack boundary to the center, respectively, were successfully predicted at $\theta = 0°$ and $45°$, respectively. However, the segments of crack front with large deviation from elliptical shape, e.g. around $\theta = 0°$ and $\theta = 90°$, which are near the center of each side, and $\theta = 45°$, which is corresponding to the round edge of the shape, the magnitudes of stress concentration or subtraction were not sufficient compared to the results given by Livieri et al. [114], which leading to the maximum deviation of 0.060 and an average deviation of 0.034.

To accommodate the additional stress concentration/subtraction raised from the large deviation from elliptical shape, a reference ellipse was defined using the least square criteria. For the square-like shape shown in Figure 4.3(a), the major ($2c_e$) and minor ($2a_e$) axis length of the reference ellipse was determined to be $c_e = a_e = 1.096a$. The reference ellipse was plotted in dashed red line in Figure 4.3(a). The mean deviation of the irregular shape from the reference ellipse was taken into account when estimating K_I through parameter p_1

$$p_1 = 2 + \left\{ \frac{1}{n} \Sigma_{i=1}^{n} \left[\left(\frac{x_i}{c_e} \right)^2 + \left(\frac{y_i}{a_e} \right)^2 - 1 \right]^2 \right\}^{1/3} \qquad \text{Eq. (4.7)}$$

the expression in the braces of the second part in Eq. (4.7) is the mean squared residuals, which are the differences between the points on the irregular shaped crack and its corresponding points on the reference ellipse. For an elliptical shape, the second part in Eq. (4.7) equals to zero, leading to $p_1 = 2$. In the case of the square-like shape shown in Figure 4.3(a), p_1 was calculated to be 2.248.

4.2.3 Consideration of the effects from local curvature

In addition to the mean deviation from the reference ellipse, locally, the curvature at each point along the crack front was also taken into account, so that the acute change of stress intensity factor around singular points can be carefully described as well. A position-dependent parameter $p_{2,i}$ was introduced into Eq. (4.6) as:

$$K_{I,i} = \frac{2\sigma}{\sqrt{\pi}} \cdot \frac{r_{ref}}{r'_{ref}} \cdot \left(p_1 \cdot {r'_{ref}}^2 - r_i^2 \right)^{1/4} \cdot p_{2,i} \qquad \text{Eq. (4.8)}$$

and $p_{2,i}$ was formulated as:

$$p_{2,i} = 1 + \sum_{j=1}^{n} m_j \cdot f_{ij} \qquad \text{Eq. (4.9)}$$

in which m_j accounts for the maximum influence of point j of the crack front due to the change of tangent line near it, and f_{ij} describes the effect of such point j on point i on the same crack front. In principle, a greater change of the tangent line at point j, described using angle ϕ_j, should lead to more noticeable influence on SIF. And a positive influence on K_I, namely additional stress concentration, will be expected for local inward curve ($\phi_j > 0$), while a negative influence on K_I will be associated with local outward curve where $\phi_j < 0$. Thus, the expression for m_j was proposed as

$$m_j = \left\{m_1 - exp\left[-\left(\tfrac{\pi+\phi_j}{2\pi}\right)^3\right]\right\}/(1 - m_1) \qquad \text{for } \phi_j < 0 \qquad\qquad \text{Eq. (4.10a)}$$

$$m_j = \left\{exp\left[-\left(\tfrac{\pi-\phi_j}{2\pi}\right)^3\right] - m_1\right\}/(1 - m_1) \qquad \text{for } \phi_j > 0 \qquad\qquad \text{Eq. (4.10b)}$$

in which $m_1 = ex\, p[-(\pi/2\pi)^3] = 0.882$ is used to normalize the expression, so that for local outward curve ($\phi_j < 0$), m_j ranges between -1 to 0, while for local inward curve where $\phi_j < 0$, m_j is between 0 to 1. In Figure 4.4(a), the change of m_j with angle ϕ_j was illustrated, in which large change of the tangent line around point j leads to an increasing deviation of $|m_j|$ from zero.

For those crack points closer to point j, a stronger influence exerted by point j on them would be expected, and it reached the maximum value of m_j at point j. Thus, an expression for f_{ij} was proposed which depends on the distance between point j and i (l_{ij}) along the same crack front.

$$f_{ij} = exp\left[-3 \cdot l_{ij} \cdot (\pi - |\phi_j|)^2/r_{ref}\right] \qquad\qquad \text{Eq. (4.11)}$$

in which ϕ_j was included to adjust the size of the affecting zone of point j. As shown in Figure 4.4(b), when reducing the distance between point i and j, an increasing influence from point j on point i, namely increase of f_{ij} value, was obtained. And the larger the $|\phi_j|$ value is, the wider the affecting distance along the crack front is expected. While for small $|\phi_j|$, f_{ij} quickly decreases to zero as increase of l_{ij}, resulting in little or no influence on the neighboring crack points. For instance, if the crack front was discretized by segments with 0.5μm in length, for point j with a small ϕ_j of 5°, its influence on the neighboring crack point i ($l_{ij} = 0.5$μm), namely f_{ij} value, quickly dropped from 1 to only

0.061, if assuming r_{ref} = 5μm. The parameter $p_{2,i}$ considered in Eq. (4.8) consists both m_j and f_{ij} functions which includes two variables (ϕ_j and l_{ij}). Its distributions as increase of l_{ij} were plotted in Figure 4.4(c) under four different ϕ_j values, namely -120º, -60º, 0º and 90º. For a flat crack front where the change of tangent line around each discrete point on it is zero (ϕ_j = 0º), the $p_{2,i}$ parameter is a constant value of 1 (shown in red line in Figure 4.4(c)), and there is no additional stress concentration/subtraction associated with the local curvature of the crack front was considered. Therefore, the SIF calculated by Eq. (4.6) and Eq. (4.8) are the same. It is also evident that for the discrete point with positive ϕ_j value where local inward crack front was expected, parameter $p_{2,i}$ is larger than one (shown in dashed blue curve in Figure 4.4(c)), which indicates higher SIF value after considering the influences of local curvature according to Eq. (4.8). While for those discrete points with negative ϕ_j, namely, local convex shape, parameter $p_{2,i}$ is smaller than one leading to lower SIF value based on Eq. (4.8).

For the square-like flaw shown in Figure 4.3(a), the SIF calculated using Eq. (4.8) was plotted in Figure 4.3(b). Compared to the results obtained using Eq. (4.6), an increased stress concentration and subtraction were successfully predicted around θ = 0º and 45º, respectively, and the average deviation from the solution has given by Livieri et al. [114] reduced from 0.034 to only 0.007.

4.3 Irregular-shaped cracks with singularity points

In order to compare the results given by Eq. (4.8), three examples of planar cracks with singularity points under tensile loading condition were considered, namely, half circle-like sinusoidal, rectangular and equilateral triangular shaped cracks.

Figure 4.5(a) shows a half circle-like sinusoidal crack whose left part has semi-circular shape with radius of a and right part follows $r(\theta) = A/\sqrt{1 + (A^2/a^2 - 1)|sin\theta|}$ with A=1.5a. The crack front was discretized by points with constant spacing of two neighboring points of 0.025a. Depending on the position, the change of tangent line (ϕ_i) around each discrete point on the crack front can be calculated for the shape shown in Figure 4.5(a), which was plotted in black circles in Figure 4.5(b). Negative ϕ_i values were obtained for all discrete points along this convex shaped irregular crack, indicating that their $p_{2,i}$ parameters were smaller than one, as shown in red cross signs in Figure 4.5(b). However, except for the singularity point at $\theta = 0°$, the ϕ_i along the crack front do not have large deviation from 0° (within 1.5°). Consequently, these discrete points do not contribute much when determining their $p_{2,i}$ parameters. On the contrary, the large change of the tangent line ($\phi_i = $ -64.4°) at the singularity point leads to a significant stress subtraction around $\theta = 0°$, therefore, a sudden decrease of $p_{2,i}$ to 0.27 at this point was expected, as shown in Figure 4.5(b). And this influence due to large local curvature change at the singularity point gradually decreases as the discrete points being away from this singularity point. Thus, an increase of $p_{2,i}$ parameter was obtained in Figure 4.5(b). Correspondingly, the calculated SIF distribution according to Eq. (4.8) was plotted in Figure 4.5(c). A decrease of K_I around the singularity point was successfully predicted by the current method. Compared to the numerical solutions in the literatures, the average deviations of K_I were 0.029 from Livieri et al. [107] and 0.028 from Mastrojannis et al. [106].

Variation of SIF along rectangular shaped cracks with different aspect ratios, namely a/c = 1, 1/2 and 1/3, were considered next, as shown in Figure 4.6. The calculated SIF

distributions given by Eq. (4.8) were checked by the numerical solutions in the literatures where the SIF was solved either by a system of integral equations defined over the crack area, i.e. [115], or through one integral equation under generic stress distribution over the cracks, e.g. [106] [116]. Figure 4.6(b) shows the comparison of SIF for a square shaped crack, in which a deep drop of $K_I/\sigma\sqrt{\pi a}$ was obtained near the singularity point ($\theta = 45°$). The average differences are small which are 0.017, 0.024, 0.037 and 0.020 from the solutions by Wang et al. [116], Livieri et al. [107], Mastrojannis et al. [106] and Isida et al. [117], respectively. As decrease the a/c ratio for the rectangular shaped crack, the reference ellipse and p_I parameter change accordingly, which were listed in Table 1. Figure 4.6(c) and (d) illustrate the change of $K_I/\sigma\sqrt{\pi a}$ along a rectangular crack with a/c = 1/2 and 1/3, respectively. Similar drops of SIF around the singularity point ($\theta = 26.56°$ when a/c = 1/2 and $\theta = 18.43°$ when a/c = 1/3) were successfully predicted by Eq. (4.8). For the rectangular crack with a/c = 1/2, an average deviation of 0.027 from Wang's solution [Wang01] was obtained. And the average errors were 0.048 and 0.038 from the solutions of Weaver et al. [115] and Livieri et al. [107], respectively, for the rectangular crack with a/c = 1/3.

When considering an embedded equilateral triangular crack (as shown in Figure 4.7(a)) subjected under tensile loading condition, the reference ellipse was determined first (red dashed circle in Figure 4.7(a)), according to the least square criteria, whose $a_e = c_e = 1.55a$. Subsequently, parameter p_I in Eq. (4.8) was calculated as 2.554 based on Eq. (4.7). The variation of $K_I/\sigma\sqrt{a}$ along the crack border was plotted in Figure 4.7(b). The sudden drops of SIF at each singularity point were successfully predicted, and the maximum $K_I/\sigma\sqrt{a}$ was determined at the center of each side which equals to 1.341. Compare to the

86

numerical solution by [106], the average deviation was 0.042. Note that rounded corners of triangular crack were considered when solving the SIF by Mastrojannis *et al.* [106]. Through the first order approximation of the Oore-Burns integral [104], the solution by Livieri *et al.* [114] exhibits a much larger average error of 0.110 when compared to the results in ref. [106].

4.4   An example of non-convex shaped crack

The shape of a fatigue crack can be much more complicated, and may has non-convex part due to, i.e. high local resistance from the microstructures [15]. Therefore, as shown in Figure 8(a), a example of non-convex shaped crack was considered whose crack border follows $r(\theta) = a + 0.1 \cdot sin\,(5\theta)$. Its reference ellipse was determined $a_e = c_e = 1.02a$, leading to parameter $p_l = 2.269$. The distribution of $K_I/\sigma\sqrt{\pi a}$ was shown in Figure 4.8(b) in which each peak is corresponding to the crack front with the minimum $r(\theta)$, while each valley represents for the crack front with the maximum $r(\theta)$. Compared to the prediction by [107], the average difference was 0.042.

4.5   Distinguish between surface and embedded cracks

For embedded cracks discussed above, their crack centers are the centroid positions of the irregular shapes. For a surface crack as shown in Figure 4.9(a), an imaginary part above the surface was considered which has mirror symmetry of the crack front with respect to the surface plane. Treating the imaginary and the real crack front as a whole crack, the new crack center can then be determined which is the centroid position of this "whole crack" locating on the surface plane, as indicated in Figure 4.9(a). Subsequently, the reference ellipse for the exampled surface crack was determined as $a_e = 1.45a$ and $c_e =$

2.51a, resulting in p_1 = 3.186. The predicted distribution of $K_I/\sigma\sqrt{a}$ along the equilateral triangular crack on the surface was demonstrated in Figure 4.9(b), in which the maximum value of 1.759 exhibits around θ = 30º. Compared to Figure 4.7(a) where a embedded crack with same equilateral triangular shape was considered, the maximum $K_I/\sigma\sqrt{a}$ increases from 1.341 to 1.759. Murakami [98] proposed a new geometric approach to approximate the maximum KI for an arbitrarily shaped 3D crack

$$K_{Imax} = 0.5\sigma_{max}\sqrt{\pi\sqrt{A_{area}}} \qquad \text{for embedded cracks}$$

$$K_{Imax} = 0.65\sigma_{max}\sqrt{\pi\sqrt{A_{area}}} \qquad \text{for surface cracks}$$

According to Murakami's approach, the maximum $K_I/\sigma\sqrt{a}$ for embedded and surface equilateral triangular cracks are 1.338 and 1.739, respectively, which is very close to the values obtained using Eq. (4.8) with deviation of 0.002 for the embedded crack and 0.012 for the surface crack.

4.6 Conclusions

- An analytical expression of stress intensity factor for an irregular shaped planar crack in three-dimensions was proposed under mode I loading condition, which derived from Irwin's analytical solution for elliptical cracks [6] by substituting elliptical-related parameters with geometric-related parameters, i.e. fractured area and circumference of the crack front.

- For irregular shape cracks with large deviation from elliptical shape, parameter p_1 was introduced which relates to the mean square root residual between the irregular shape and its fitted ellipse.

- For irregular shape cracks with singularity points, parameter $p_{2,i}$ for each discrete point on the crack front was considered, which includes the influences of local curvature along the entire crack front.

- Good agreements of the SIF between the current work and existing numerical solutions were obtained for several typical crack shapes, i.e. rectangular cracks with different aspect ratios, triangular cracks as well as a non-convex shaped crack, with average deviations smaller than 5%.

- For the surface and embedded cracks with same shape, the current expression of SIF was able to distinguish the differences of their SIF distributions whose maximum values are consistent with Murakami's $\sqrt{area}$ method [106].

Appendix

Introducing parameter θ which was indicated in Fig. 1, and the relation between angle θ and φ can be obtained as:

$$x = r(\theta) \cdot cos\theta = c \cdot cos\alpha$$

$$y = r(\theta) \cdot sin\theta = a \cdot sin\alpha$$

Substituting angle φ with θ, Eq(a) can be rewritten as

$$K_I = \frac{\sigma\sqrt{\pi a}}{E(k)} \left(\frac{r(\theta)^2}{a^2} \sin^2\theta + \frac{a^2}{c^2} \cdot \frac{r(\theta)^2}{c^2} \cos^2\theta \right)^{1/4}$$

$$K_I = \frac{\sigma\sqrt{\pi a}}{E(k)} \left\{ \frac{r(\theta)^2}{a^2} + \cos^2\theta \cdot \left[\frac{r(\theta)^2}{c^2} \cdot \frac{(a^2+c^2)(a^2-c^2)}{a^2c^2} \right] \right\}^{\frac{1}{4}}$$

From the expression of elliptical shape

$$\frac{r(\theta)^2 \cos^2\theta}{c^2} + \frac{r(\theta)^2 \sin^2\theta}{a^2} = 1$$

One can obtain

$$\cos^2\theta = \frac{c^2 \cdot (a^2 - r(\theta)^2)}{r(\theta)^2 \cdot (a^2 - c^2)}$$

And put it into Eq(A1)

$$K_I = \frac{\sigma\sqrt{\pi a}}{E(k)\sqrt{c}} (a^2 + c^2 - r(\theta)^2)^{1/4}$$

As mentioned earlier in the paper, two parameters, r_{ref} and r'_{ref}, relating to the fractured area and the circumference were introduced. For an embedded elliptical crack, in which $r_{ref} = \sqrt{ac}$ and $r'_{ref} = 2cE(k)/\pi$, the expression for SIF is

$$K_I = \frac{2\sigma}{\sqrt{\pi}} \cdot \frac{r_{ref}}{r'_{ref}} \cdot (a^2 + c^2 - r(\theta)^2)^{1/4}$$

Table 4.1. Parameters calculated for the rectangular shaped cracks

Rectangular shape	p_1	Half minor axis length of reference ellipse	Half major axis length of reference ellipse
a/c=1	2.367	1.183	1.183
a/c=1/2	2.361	1.140	2.498
a/c=1/3	2.353	1.120	2.922
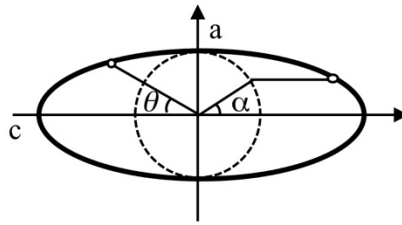
Figure 4.1. Definition of the parameters in Eq. (4.1).
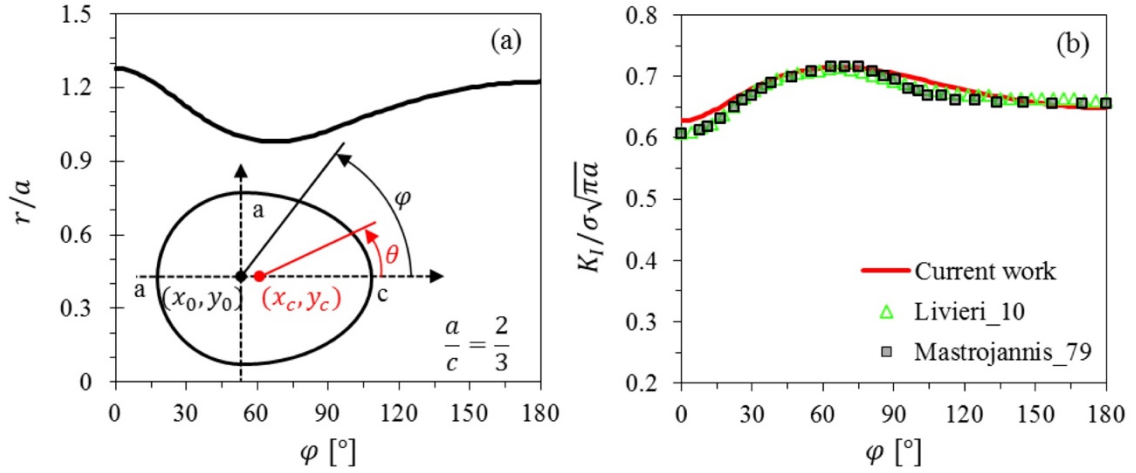
Figure 4.2. For an asymmetric crack with half circular-half elliptical shape, (a) the distribution of the distance from crack front to the crack center, and (b) comparison of SIFs between existing solutions in literature and Eq. (4.6).
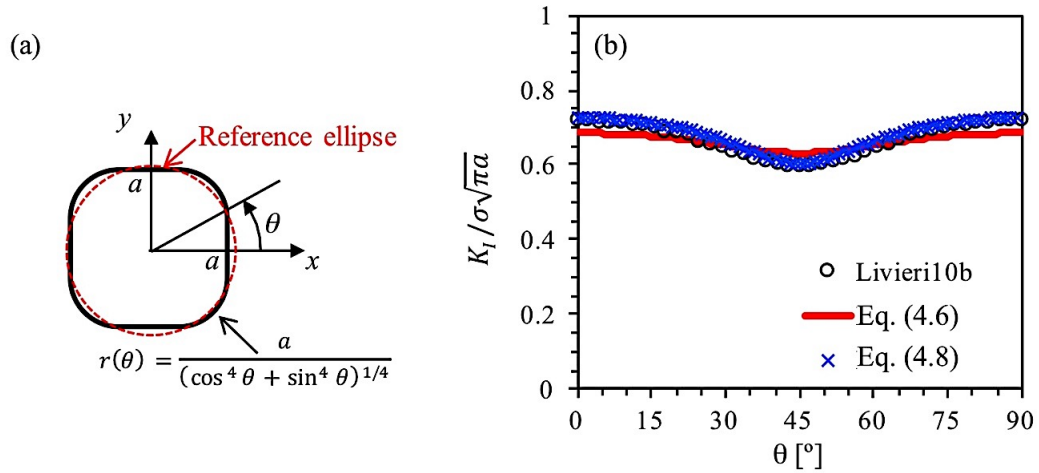
Figure 4.3. (a) A square-shaped flaw, (b) SIF along the square-shaped flaw shown in (a) by means of Eq. (4.6) and Eq. (4.8).
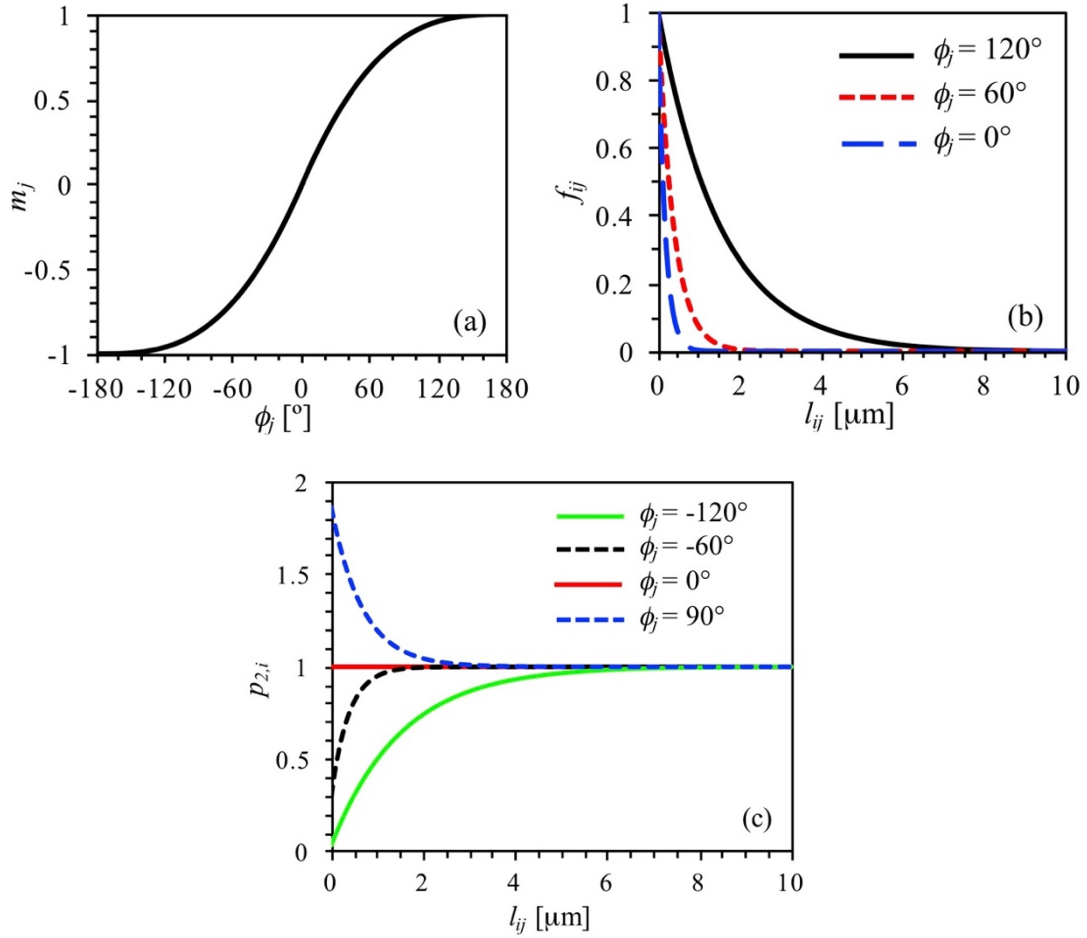
Figure 4.4. (a) The change of m_j with angle ϕ_j, (b) the distribution of f_{ij} with l_{ij} under different ϕ_j values (assume $r_{ref}= 5\mu m$), and (c) the change of the parameter $p_{2,i}$ as increase of l_{ij} under different different ϕ_j values (assume $r_{ref}= 5\mu m$).
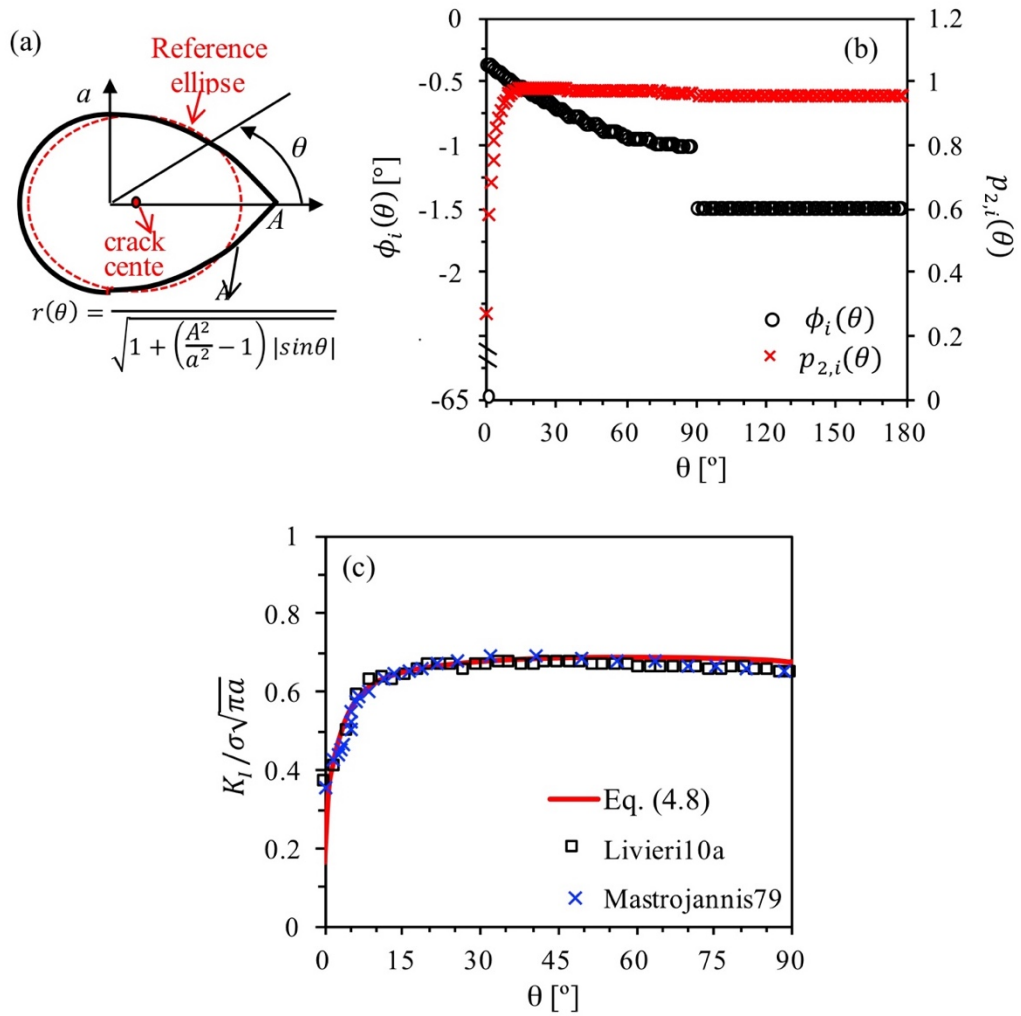
Figure 4.5. (a) A half circle-half sinusoidal crack (A/a = 1.5), (b) the change of tangent line (ϕ_i) and parameter $p_{2,i}$ along the crack front, and (c) comparison between the numerical solutions and Eq. (4.8) for the irregular-shape crack shown in (a).
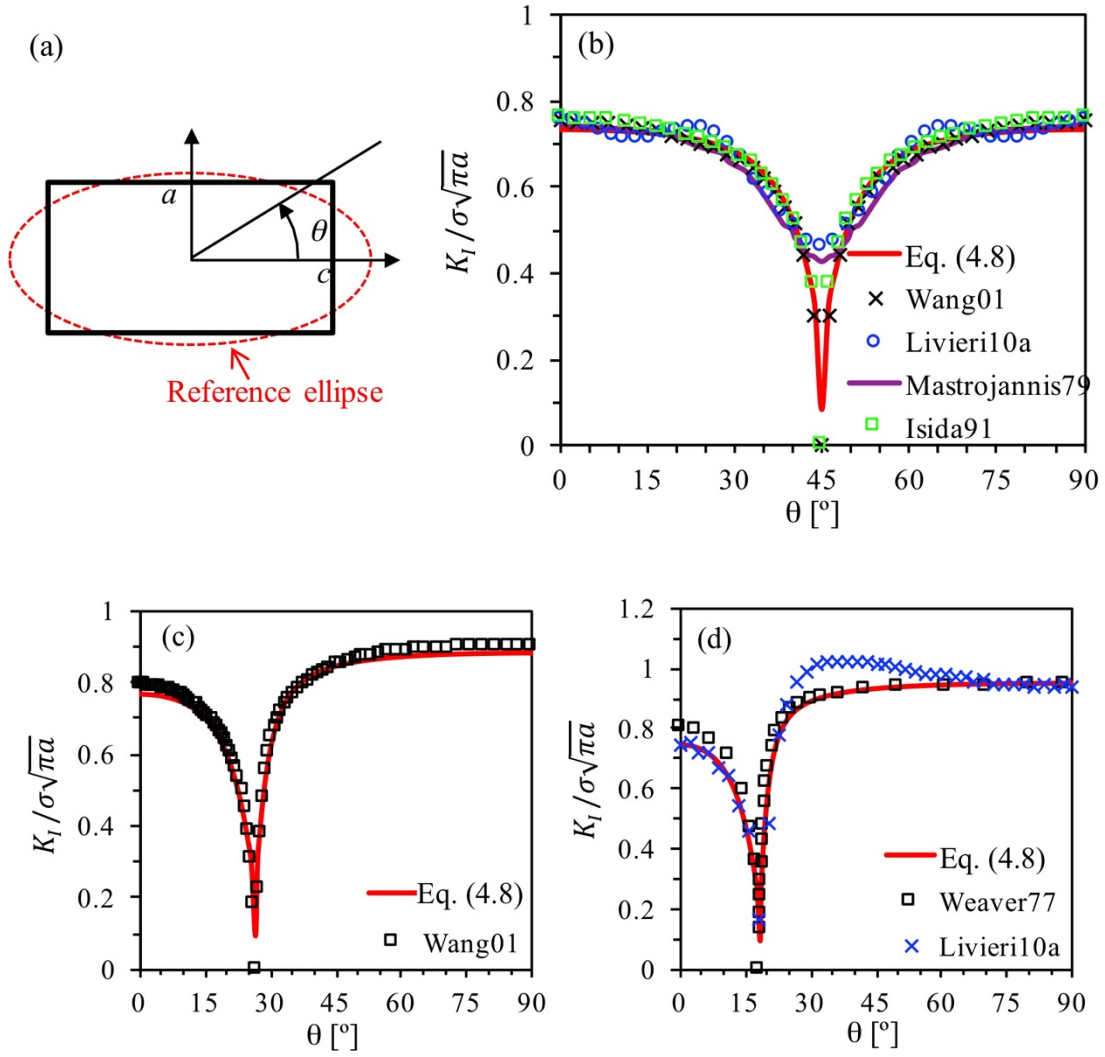
Figure 4.6. Comparison between existing numerical solutions and Eq. (4.8) for rectangular-shape crack shown in (a), with (b) a/c=1, (c) a/c=1/2, and (d) a/c=1/3.
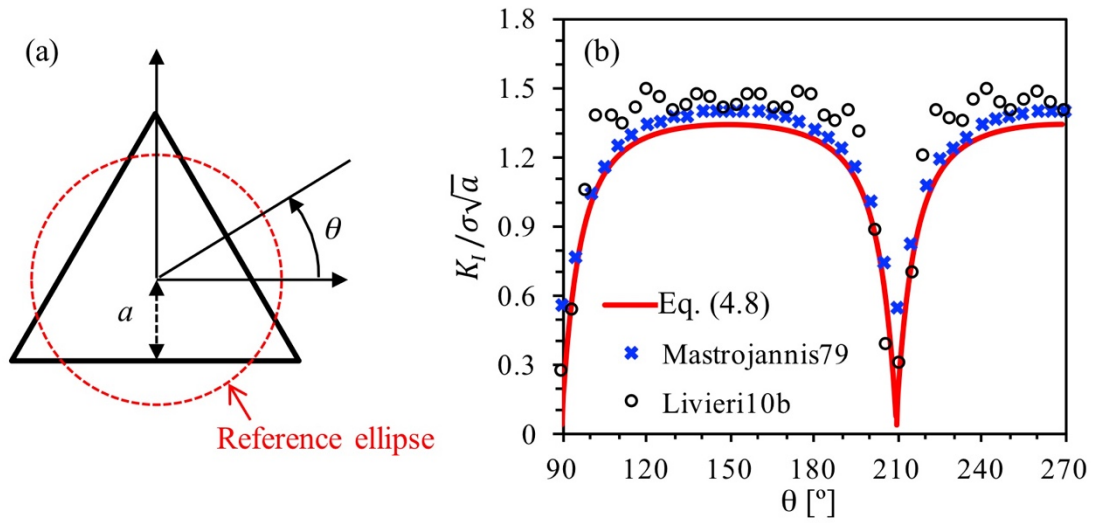
Figure 4.7. (a) A equilateral triangular shape crack, (b) comparison between existing numerical solutions and Eq. (4.8) for the irregular-shaped crack shown in (a).
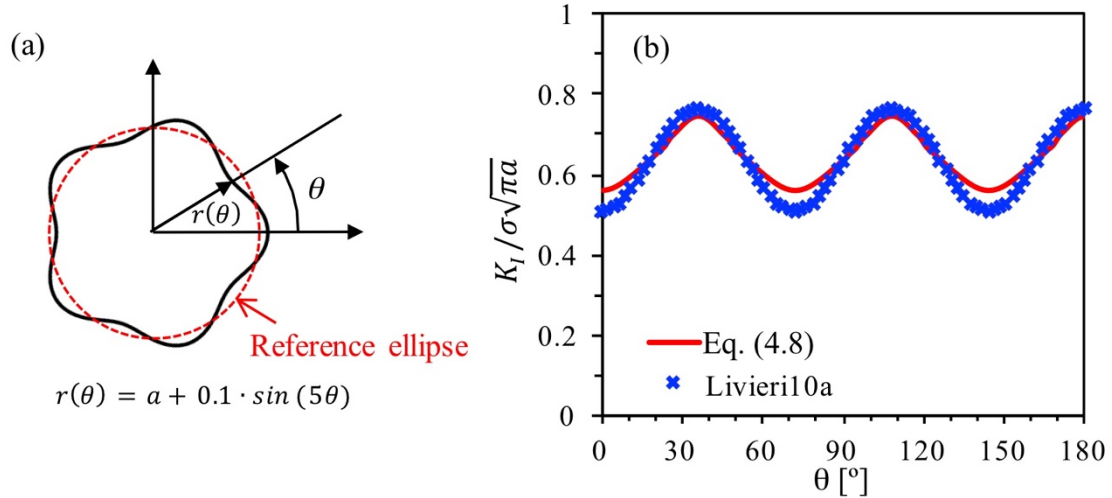
Figure 4.8. (a) An example of non-convex shape crack, (b) comparison of the solution from Eq. (4.8) and the existing solution according to Livieri *et al.* [107] for the irregular shape crack shown in (a).
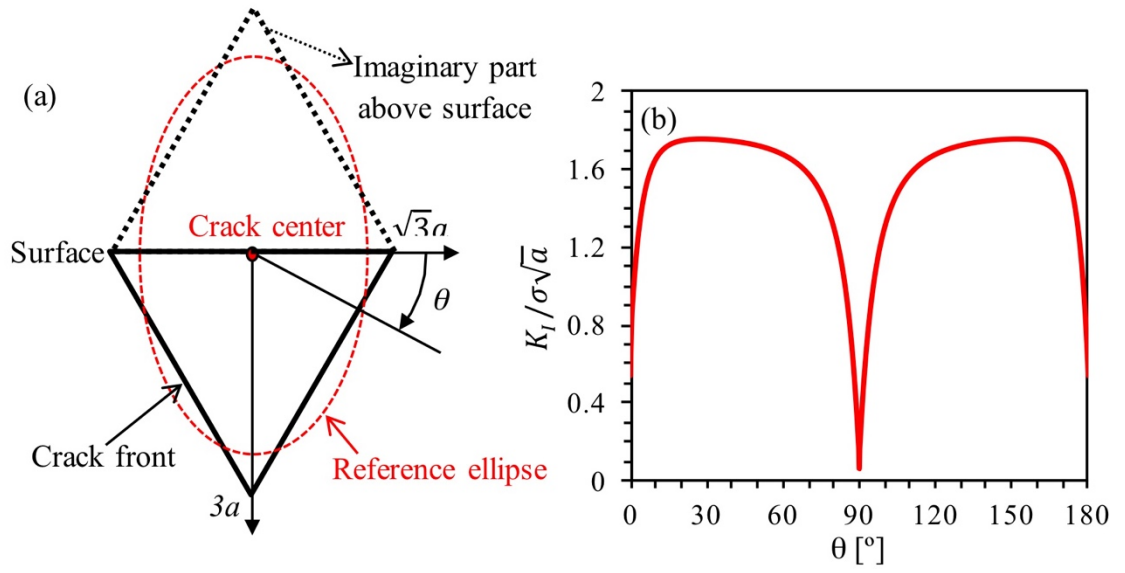
Figure 4.9. Prediction of K_I for a surface equilateral triangular shape crack using Eq. (4.7).

CHAPTER 5   Simulation of short fatigue crack growth from micro-notches in an AA2024-T351 alloy using a 3D microstructure-based model

5.1   Introduction

Initiation and propagation of short fatigue cracks can consume 50-90% of the total fatigue life of an engineering component [118]. In high strength aluminum alloys, such as 2000 and 7000 series aluminum alloys, the preferred nucleation sites of fatigue cracks are often the pre-fractured constituent particles, i.e. Fe-containing particles [23, 51, 52]. Due to the brittleness of these particles at elevated temperature, some of them were fractured during hot deformation processing, i.e. hot rolling or hot extrusion, thereby becoming the fatigue crack initiation sites during cyclic loading due to the existence of micro-cracks in these particles. However, most of the micro-cracks in these fractured particles never extended into the matrix (forming so-called type 1 cracks) [55]. Only few of them can successfully propagate into the matrix during cyclic loading, but they could still be arrested by local microstructure barriers, like grain boundaries (GBs), which were referred as type 2 cracks in this work. Eventually only about 5% of these micro-cracks can successfully develop into long fatigue cracks (named as type 3 cracks). Earlier studies [54, 58, 118] have shown that both particle width on the surface and thickness beneath the surface are important factors controlling the propagation behaviors of fatigue

cracks from the pre-fractured particles in AA2024-T351 alloys. And the larger particle sizes were, the easier crack propagation was. However, this theory cannot explain the experimental observations [50, 55] that the fatal cracks were not necessarily developed at the largest fractured particles, and, occasionally, the cracks from the particles with much smaller size can still develop into long fatigue cracks. According to the statistical results [55], in AA2024-T351 alloy, the dimensions of the particles from which fatigue cracks were successfully initiated ranged from 5 to 30μm. This large fluctuation of particle dimensions also indicates there must be other factors that could have a substantial influence on the propagation behaviors of the micro-cracks in the pre-fractured particles. Apparently, consideration of the particle geometry alone cannot explain these phenomena and may underestimate the critical size of the defects to develop a fatal fatigue crack in the alloy. Therefore, the growth behavior of the micro-cracks in the pre-fractured particles in high strength Al alloys still needs to be quantitatively understood.

In the past decades, several models [30, 70, 119, 120] were developed in attempt to quantify the microstructure influence on the propagation of short fatigue cracks, especially the effects from GBs and constituent particles. However, most of them were 2D in nature, thereby could not satisfactorily capture the growth behaviors of short fatigue cracks, since the cracks interact with the local microstructure in three dimensions. Based on the crystallographic model for a short crack growth across a grain boundary by crack plane twist and tilt, Wei and Zhai [100] firstly established a quantitative microstructure-based model to simulate the 3-D growth behaviors of short cracks in planar slip alloys, by incorporating a hypothesized relationship between GB resistance and crack plane twist as a Weibull-type of function into the model. Later, the relationship

has been verified by experiments [72]. Recently, McDowell et al. [47] also developed a 3D model and included a constant GB resistance term when simulating crack tip and GB interactions. This approximation might be suitable when the driving force of crack propagation was dominant compared to the value of boundary resistance, so the oscillation of boundary resistance can be ignored. However, the influence of GB resistance becomes more significant with decreasing crack length. Thus, in the early stage of fatigue crack growth, especially for those short cracks in a microstructure with a high density of local barriers, i.e., GBs and interfaces, the variation of the local resistance could greatly affect the crack growth behaviors, therefore, it cannot be neglected. Furthermore, it is reasonable to believe that the resistance at particle/matrix interface also contributes to the observed different crack propagation behaviors from the pre-fractured particles [55]. As the crack plane inside these brittle particles is commonly assumed perpendicular to the loading axis [55, 121], the crack plane deflection at the particle/matrix interface can be expected when the crack extends into the matrix. Since the twist component of crack plane deflection at a GB has been determined to be the key parameter controlling the GB resistance against crack growth [42], similarly, the twist angle at the particle/matrix interface should also be taken into consideration when determining the resistance toward micro-crack growth from the pre-fractured particles.

In order to study quantitatively the influence of interface resistance as well as the effect of particle geometry, rectangular micro-notches were fabricated in attempt to mimic the pre-fractured particles with highly irregular shape (large deviation from semi-circular shape), so that the dimensions of micro-notches and the orientations of grain where the notch located can be well controlled. However, challenges remain for the definition of the

stress intensity factor (SIF) and resistance distribution along the crack front with irregular shape. Recently, an experimental methodology was developed to quantitatively measure the GB resistance toward short fatigue crack growth in an AA2024-T351 alloy [72], which paved the way for modeling the crack propagation in three dimensions in microscopic scale. Therefore, in this work, besides the quantitative representation of resistance on the GBs and interfaces, a correlation function was also developed to describe the dragging effect by each of the local microstructure barriers that intersected with the crack on the total resistance at each point along the crack front. The proposed solution of SIF for a surface irregular-shaped crack in Chapter 4 will be used here.

5.2 Methodology

5.2.1 Definition of reference center

The outline of a short fatigue crack usually does not have an ideal circular/elliptical shape and asymmetric due to local microstructure barriers, like GBs and interfaces. Thus, in the current work, the concept of reference center (x_c, y_c) was used to define the crack center. For a surface crack, an imaginary part out of surface was considered, so that the surface crack and its imaginary part together exhibit mirror symmetry with respect to the surface plane. And the centroid position of this whole part was defined as the reference center. In other words, for a surface crack, the reference center always locates on the surface plane, which indicates $y_c = 0$. And x_c can be calculated as:

$$x_c = \frac{1}{6A_{crack}} \sum_{i=1}^{n-1} (x_i + x_{i+1})(x_i \cdot y_{i+1} - x_{i+1} \cdot y_i) \qquad \text{Eq. (5.1)}$$

in which A_{crack} is the area surrounded by the crack front, x_i and y_i is the coordinates of discrete point i on the crack front, and n is the number of such discrete points. As the

crack front evolves during cyclic loadings, the position of the reference center may also change depending on the crack shape. And in the current model, the definition of the reference center directly affects its distance to a discrete point on the crack front, which is important when calculating its SIF and resistance and will be introduced in details in the following sections.

5.2.2   SIF defined for an irregular crack

When simulating the propagating behaviors of fatigue cracks from pre-fractured particles, the initial crack front shape depending on the particle geometry was irregular and asymmetric. Although the crack front tended to form semi-circular shape after propagated into the matrix grain [98], due to asymmetric local microstructure barriers, it would again evolve into irregular shape. In some models [54, 119], the initial crack shape at the fractured particle was simplified as semi-circle/ellipse. However, the particle/matrix interface resistance considered in the current work strongly depends on the orientation of interface [29], namely, the particle geometry, thus, the initial crack shape which is identical to the particle geometry perpendicular to the surface cannot be simplified as semi-circular shape, because it may significantly alter the resistance that the crack fronts should have experienced during their early propagation from these particles/notches. Although there are existing numerical solutions of SIF for surface irregular shaped cracks under tensile loading condition, i.e. the weight function [104, 105] and the body force method [116, 117], they usually involve solving several singular integral equations. For the growth of a fatigue crack which can easily consume up to millions of loading cycles, the crack shape may vary after every loading cycle, which aggravates the computational expanse. Although some numerical solutions can predict SIF with high accuracy, their

high computational cost cannot be neglected, especially when trying to capture the stochastic growth behaviors of short fatigue cracks in the alloy. Therefore, a more straightforward method is still desirable, and the new approach elaborated in Chapter 4 was used in the current work to capture the distribution of the SIF along the irregular crack fronts with acceptable deviation from the existing solutions.

5.2.3　Definition of resistance along crack front

5.2.3.1　Resistance at grain/notch root

The twist component of crack plane deflection at GB was proposed [42] to be the key parameter influencing the propagation of short fatigue crack across the GB. And the crack would follow the slip plane that offers the minimum twist angle (α) in the neighboring grain. This minimum α angle criteria have been observed in several planar slip alloys, e.g. Al-Li8090 [29], AA2026 [43], CMSX-4 [39], Tiβ21S alloy [18] and a Mg alloy [44]. Recently, the GB resistance was experimentally quantified in authors group [72], which showed a Weibull-type function of the α angle on GB.

$$R(\alpha) = R_f\{1 - exp[-(\alpha/\alpha_0)^n]\} \qquad\qquad \text{Eq. (5.2)}$$

in which R_f represented the maximum resistance that a GB can exert, n and α_0 are material dependent parameters. These parameters were determined in *ref.* [72] for an AA2024-T351 alloy, which were $0.9\,MPa\cdot\sqrt{m}$, 20.1º and 4.2 for R_f, α_0 and n, respectively. In the current work, these values were used when calculating the resistance at notch root and GBs in an AA2024-T351 aluminium alloy.

5.2.3.2 Dragging force from retarded crack points

In order to propagate across a GB, the discrete points on the crack front have to overcome the GB resistance $R(\alpha)$ defined by Eq. (5.2), thus their propagation will be retarded or even completely stopped. However, as a continuum solid, the crack front connecting to these pinned/retarded crack points cannot continue to propagate, unaffectedly. They will start to experience a dragging force exerted by these pinned/retarded crack points. In the early work (Chapter 3), such dragging effect was described using a normal distribution which only depends on the distance between a discrete crack point to the pinned/retarded crack point. However, this descript of dragging force has several drawbacks. Firstly, it does not distinguish the crack points (j_{behind}) falling behind the pinned/retarded point (i_{pinned}) from those for those moving forward points ($k_{forward}$). In an equilibrium condition, a semi-circular crack front will be obtained where the distance from any discrete point to the reference center (r_i) are the same. Thus, for those crack points already falling behind the pinned/retarded one, namely $r_{j-behind} < r_{i-pinned}$, they will propagate faster in order to catch up the rest of the crack front, and for them, there should be no dragging force considered from those pinned/retarded points. Secondly, as a discrete point continues to move forward, while the pinned point remains its position, namely the difference of their distances to the reference center increases ($\Delta r_{ki} = r_{k-forward} - r_{i-pinned}$), a more prominent dragging effect should be expected, as indicated in Figure 5.3(a). On the other hand, as such moving-ahead points being further away from the pinned/retarded points, namely increase of angle θ_{ik}, as shown in Figure 5.2, a decrease of the dragging force should be considered, as indicated in Figure 5.3(b). However, according to the nominal distribution used in Chapter 3, the change of dragging force solely depends on the distance between

the pinned/retarded point and a discrete point on the crack front (l_{ki}), as shown in Figure 5.2. This dose not distinguish the differences of radial distance (the dragging force should increase with increase of Δr_{ki}) from the angular distance (the dragging force should decrease with increase of θ_{ik}). Taken into account the influences of these factors, a dragging parameter P_{ki} was proposed to describe such dragging effect exerted by pinned/retarded crack point i on those crack point k propagating ahead of point i:

$$P_{ki} = 1 - exp\left[-\frac{r_k - r_i}{2\theta_{ki} \cdot r_i}\right] \qquad \text{when } r_k > r_i \qquad \text{Eq. (5.3)}$$

in which, r_i and r_k are the distances from crack point i and k to the reference center, respectively, and the dragging parameter P_{ki} ranges from 0 to 1. Figure 5.3(c) was an example showing the distribution of such dragging parameter P_{ki} beneath the surface due to the pinned crack point i on the GB. The intensity of the dragging effect was represented using the rainbow colors. For those crack points whose distance to the reference center was smaller than r_i, the dragging parameter equals to zero, i.e. the crack points located within the semi-circle in dashed white line shown in Figure 5.3(c). Only for those points with $r_k > r_i$ will experience a non-zero dragging parameter. For instance, as crack point k, indicated in Figure 5.3(c), propagated to position k', namely increase of r_k while r_i and θ_{ki} remaining constant, an increase of the dragging parameter can be expected, as shown in Figure 5.3(c) where the colour/intensity of parameter P_{ki} changes from blue (zero) to light red (~0.8). If increase the angular distance and move crack point k' to k'', namely increase of θ_{ik}, while fixing the r_i and r_k values, the dragging parameter was gradually reduced, as illustrated in Figure 5.3(c).

It is worth mentioning that several discrete points on the crack front may be pinned on the same local microstructure barrier, however, among them, only the crack points directly connecting to the discrete points that are not on the microstructure barrier will be considered to exert the dragging force. When the crack points were pinned/retarded on different local microstructure barriers, an accumulative dragging effect was taken into account when calculating the total resistance experienced by a discrete point on the crack front through

$$R_j = \sum_{i=1}^{N} R_i(\alpha) \cdot P_{ij}(\theta_{ij}, r_i, r_j) \qquad \text{Eq. (5.4)}$$

in which N is the number of microstructure barriers that fatigue crack front interacted.

5.2.3.3 Average resistance to crack growth

In addition to the local resistance stemmed from microstructure barriers, an average resistance (R_{ave}) toward crack propagation was also considered. In the current work, an average resistance of $0.5 MPa \cdot \sqrt{m}$ was used, which was comparable to the minimum ΔK_I required for crack to propagate one Burgers vector ($|\vec{b}| = 0.28 \times 10^{-3} \mu m$) in aluminum alloys during one loading cycle.

5.2.4 Formulation of short crack growth

In the current work, the irregular crack front was discretized by points, and an effective driving force ($\Delta K_{eff,i}$) was considered when formulating the propagation of each discrete point on the crack front. It includes the SIF range ($\Delta K_{I,i}$) and a resistant term (R_i), which depend on the crack geometry and microstructures. The resistance considered here for short fatigue crack is analogous to the concept of the threshold SIF range defined for long

crack. However, instead of a constant value, the resistance considered in the current work is a variable depending on the local microstructure, i.e. grain orientation and particle geometry, as introduced in section 5.2.3. the $\Delta K_{eff,i}$ which equals to $\Delta K_{I,i}$ minus R_i was employed in this modified Paris power law to formulate the growth of a discrete crack point i on the crack front

$$\Delta a_i = \int C\left(\Delta K_{eff,i}\right)^m dN \qquad\qquad \text{Eq. (5.5)}$$

in which Δa_i is the propagating distance of discrete point i. The growth of crack point i will only be considered if a positive value of $\Delta K_{eff,i}$ is achieved. Parameters C and m are material dependent coefficients. In the current work, fatigue tests were conducted in AA2024-T351 alloy. Therefore, the exponent m of 2.73 was used, which is the same as the one quantified for long crack growth in AA2024 alloys [122]. Whereas a value of 1.89×10^{-9}m/cycle was assign to the coefficient C, which is an order of magnitude larger than that determined for long cracks as short fatigue cracks usually grow faster than the long cracks by 1 to 2 orders of magnitude [7].

In the current model, several assumptions were made including:

i)   The propagation of short fatigue crack follows one of the {111} slip plane orientation in each grain that the crack passed.

ii)   Applied to high cycle fatigue region.

iii)   Good bonding between the constituent particles and the matrix, so that the fatigue cracks do not initiate by particle debonding.

iv)   Homogeneous matrix grains are assumed except for GBs and interfaces

v)   The tortuous short fatigue crack profile is projected on the plane perpendicular to the load axis, so that the proposed analytical solution of SIF for an arbitrary-shape fatigue crack in three-dimensions for mode I loading can be applied.

5.3   Experiments

An AA2024-T351 alloy was selected in the current work, which was hot rolled to plate with thickness of 7mm, before solution heat treated and natural aged. The chemical composition of the alloy was shown in Table 5.1. The microstructure with elongated grain structured was demonstrated in Figure 5.1(a), with average grain size of 361 x 97 x 37 μm^3 in L (rolling), T (transverse) and S (short transverse) direction, respectively. The samples prepared for the four-point bend fatigue tests (4.6 (L) x 36(T) x 8 (S) mm^3) were cut with the plane under tension loading being parallel to the T-S plane, and the load axis being along T direction. The T-S plane was selected to fabricate micro-notches for two reasons. Firstly, the fractured Fe-containing particles were the primary fatigue crack nucleation sites on L-T plane, as the fracture plane is mostly parallel to the T-S plane. Therefore, when loading along T direction, the favorite fatigue crack initiation spots will become the fabricated micro-notches which are perpendicular to the T-S plane, instead of the fractured constituent particles. Moreover, the grains are elongated along the L direction which is perpendicular to the T-S plane. Thus, statistically, the initiated fatigue cracks from the micro-notches will have lower probability to interact with the GBs beneath the sample surface during its early stage of propagation, which could greatly simplify the situation and focus only on the influences of the notch roots on the short fatigue crack growth behavior from the micro-notches. The sample surface (T-S plane) under the cyclic tensile stress was ground first with waterproof abrasive papers from grit

240 to 1200, then mechanically polished using alumina powders from 1μm to 0.05μm and a silica colloidal suspension liquid, before etched with the Keller's etchant.

Using focused ion beam (FIB) in a Hitachi NB5000 dual beam SEM/FIB system, micro-notches were then fabricated with notch plane perpendicular to the loading axis (L direction) to mimic the fractured constituent particles, as shown in Figure 5.1(b). The selection of grains where the micro-notches locate were based on two criteria: firstly, the grain size in S direction should be large enough to contain the fabricated notch which ranging between 10-40 μm; secondly, the distance between each two micro-notches should be large enough to avoid possible stress shielding, i.e. at least 500 μm apart in both T and S directions. The corresponding grain orientations were measured with an Oxford Instrument EBSD system.

The samples with micro-notches were then subjected under the fatigue tests using a self-aligning four-point bend rig [64] under a constant maximum stress of 340MPa, which is equivalent to 95% the yield stress (358MPa) in the T direction at frequency of 20Hz, stress ratio $R = 0.1$ and room temperature in air. The tests were terminated when the sample failed, namely, the maximum sample deflection exceeded a pre-defined value. And the samples were then examined using optical microscope to reveal the short fatigue crack growth behavior from the fabricated micro-notches.

5.4 Comparison between experimental and simulated results

5.4.1 An example of type 3 fatigue crack from the micro-notch

Figure 5.4(a) is an example of a type 3 fatigue crack propagated from a micro-notch observed in the experiment, in which the notch boundary was highlighted using green

lines. The notch dimensions were measured as 30 x 12.2 x 2 μm^3 in S, L and T directions, respectively. Earlier experiments [37] observed the crystallographic propagation behaviors of short fatigue cracks in AA2024-T351 alloys, which is consistent with the current experimental observations shown in Figure 5.4(a). In order to determine the crack plane orientation immediate after the fatigue crack extended into the matrix grain, the grain orientation needs to be measured first using EBSD, which was [308.5º 36.9º 17º]. And the slip traces (SLTs) of the four {111} slip planes on the sample surface can then be computed using

$$SLT = (g \cdot SP) \times L \qquad\qquad\qquad \text{Eq. (5.6)}$$

in which g is the rotation matrix calculated from the three Euler angles [φ_1 φ_2 Φ] of the matrix grain

$$g =$$

$$\begin{pmatrix} cos\varphi_1 cos\varphi_2 - sin\varphi_1 sin\varphi_2 cos\Phi & sin\varphi_1 cos\varphi_2 + cos\varphi_1 sin\varphi_2 cos\Phi & sin\varphi_2 sin\Phi \\ -cos\varphi_1 sin\varphi_2 - sin\varphi_1 cos\varphi_2 cos\Phi & -sin\varphi_1 sin\varphi_2 + cos\varphi_1 cos\varphi_2 cos\Phi & cos\varphi_2 sin\Phi \\ sin\varphi_1 sin\Phi & -cos\varphi_1 sin\Phi & cos\Phi \end{pmatrix}$$

[65]

SP is slip plane orientation in crystal coordinates and L is the normal direction to the sample surface. For the four {111} slip planes in the matrix grain, their calculated slip traces on the sample surface (T-S plane) were illustrated in Figure 5.4(b). Only the slip trace of the ($1\bar{1}1$) slip plane exhibits the same orientation with the crack trace measured in the matrix grain on the sample surface (highlighted using red lines in Figure 5.4(a)). Therefore, the orientation of crack plane can be determined to follow the ($1\bar{1}1$)

orientation of the matrix grain. Knowing the notch plane is perpendicular to the loading axis, the corresponding twist and tilt angles at vertical notch root for the four {111} slip planes can be calculated, which were listed in Table 5.2. Among the four {111} slip planes, the fatigue crack extended from the micro-notch selected the $(1\bar{1}1)$ orientation which has the minimum twist angle with the vertical notch root. This further verified the minimum twist angle criteria proposed by Zhai et al. [42].

In the model, an initial rectangular crack with 30 μm in S direction on the surface and 12.2 μm in L direction beneath the surface was constructed, as shown in Figure 5.4(c) (the green rectangular shape). Given the experimentally determined matrix grain orientation and the micro-notch orientation, the model is able to automatically select the crack plane in the matrix grain following the minimum twist angle criteria. In this case, the $(1\bar{1}1)$ orientation with the smallest twist angle of 3.7° was selected as the crack plane in the matrix grain, and the corresponding resistance along the notch root can be calculated based on Eq. (5.4), which was $7.2\times10^{-4}\ MPa \cdot m^{0.5}$ along the two vertical notch roots and $0.150 MPa \cdot m^{0.5}$ along the horizontal notch root (bottom of the notch). After taking into account the average resistance of $0.5 MPa \cdot \sqrt{m}$, the total resistance against the fatigue crack to extend from the micro-notch into the matrix grain was illustrated in Figure 5.4(d) in dashed red line. The sudden change of the resistance at $\theta = $ 39º and 141º which corresponding to the two corners of the rectangular micro-notch is attributed to the change of notch root orientation from vertical to horizontal. For the micro-notch shown in Figure 5.4(a), the distribution of its ΔK_I along the notch roots/initial crack front when subjected under maximum loading of $358 MPa$ was plotted in Figure 5.4(d) in solid black line. Sharp decreases of ΔK_i around the rectangular corners

were successfully predicted, and the highest ΔK_i value of $1.479 \ MPa \cdot \sqrt{m}$ was obtained at $\theta = 90^\circ$. Except for the crack front around the two corners of the rectangular micro-notch, ΔK_i is larger than the total resistance, resulting in a positive $\Delta K_{eff,i}$ value. Therefore, in the next loading cycle, these discrete points on the crack front with positive $\Delta K_{eff,i}$ will propagate following Eq. (5.5).

The simulated propagation of the short fatigue crack beneath sample surface was demonstrated in Figure 5.4(c), in which the fatigue crack from the rectangular micro-notch gradually evolved into a semi-circular shape. To better illustrate the evolution, the crack front was projected on the L-S plane (perpendicular to the sample surface) and plotted every 4000 loading cycles. Thus, the denser the crack contours are, the lower the crack growth rate is. At the initial state, the crack front near the two corners of the rectangular micro-notch cannot propagate due to negative $\Delta K_{eff,i}$, or grow very slowly because of their small $\Delta K_{eff,i}$. Therefore, denser crack contours around these two corners were observed in Figure 5.4(c). As the rest part of the crack front continued to propagate, the tangent line change of the crack front (ϕ_j) around the two corners gradually smoothened from -90° to 0°, which according to Eq. (5.8), leads to an increase of the ΔK_I. The corresponding distributions of ΔK_i along the crack front were illustrated in Figure 5.4(e). As crack shape evolved under different loading cycles, the sharp decreases of ΔK_I around the two corners became less prominent. Eventually, a smooth and relatively constant distribution of ΔK_I was obtained around 36000 cycles which indicates the crack front had evolved from the initial rectangular to a semi-circular shape. If no other microstructure barriers, e.g. GB and particles, exists, the short fatigue crack will continue

to grow remaining a semi-circular shape, as shown in Figure 5.4(c). Consequently, the ΔK_I distributed along the crack front will increase, as demonstrated in Figure 5.4(e) when the loading cycles increases from 36000 to 60000.

5.4.2 An example of type 2 fatigue crack

An example of type 2 fatigue crack extended from the micro-notch with $10 \mu m$ in S direction and $10.2 \mu m$ in L direction was observed in the experiment, as shown in Figure 5.5(a). The left crack tip on the surface (Tip B) propagated $11.8 \mu m$ in S direction before ceased, while the right crack tip (Tip A) extended into the matrix grain for only $2.6 \mu m$ in S direction. From the inverse pole figure (IPF) map in Figure 5.5(c), the outline of G1 was obtained which was superimposed on Figure 5.5(a) using black lines. It is evident from Figure 5.5(a) that tip A stopped at the GB between G1 and G1 (called GB1/2), which explains the relatively short propagating distance of tip A. Crack tip B, on the other hand, ceased its propagation within G1, before intersecting with any GB. The propagation of both crack tips showed a crystallographic growth behaviour, and their crack planes followed the same orientation. To determine the crack plane orientation in G1, similar approach was employed as the one in section 5.4.2. Known the Euler angles of G1 ([246.8º 30.6º 83.5º]), the slip traces of the four {111} slip planes in G1 on sample surface (T-S plane) were calculated and plotted in Figure 5.5(b). Compared with the crack trace on the surface (indicated using red line in Figure 5.5(a)), two of the four {111} orientations were both very close to the crack trace, namely $(1\bar{1}1)$ and $(11\bar{1})$ planes. Therefore, FIB was introduced to reveal the crack trace on the cross-section plane (L-S plane) perpendicular to the sample surface, as shown in Figure 5.5(d). Correspondingly, the slip traces of the four {111} slip planes on the FIB cross-section plane were also

calculated, as illustrated in Figure 5.5(e). Now, compared with the crack traces on both sample surface and the cross-section plane, only the slip traces of $(1\bar{1}1)$ orientation in G1 aligned perfectly well with them. Thus, the crack plane orientation in G1 can be determined unambiguously. Moreover, from the FIB cross-section plane in Figure 5.5(d), the twist angle between the crack plane and the vertical notch root can be directly measured, which was around 10º. This value is consistent with the calculated twist angles of 10.5º for the $(1\bar{1}1)$ slip plane, which has the smallest twist angles among the four {111} slip planes in G1, as listed in Table 5.3. This example again obeys the minimum possible twist angle criteria proposed in the earlier work by Zhai et al. [42].

When constructing this example in the model, besides the shape and size of the micro-notch, the position of GBs and the neighbouring grain orientations were measured on the sample surface and taken into consideration in the model, because they also played an important role during the fatigue crack growth from the micro-notch in this case. As shown in Figure 5.6(a) in dashed red lines, GB1/2 and GB1/3 located $2.6\mu m$ and $10\mu m$ (in S direction) away from the right and left vertical notch roots, respectively. Known the Euler angles of G1 and the notch plane orientation, the $(1\bar{1}1)$ orientation was automatically assigned as the fatigue crack plane in G1 due to its smallest twist angle, which leads to resistance of 0.06 and 0.90 $MPa \cdot \sqrt{m}$ at the vertical and horizontal notch roots, respectively. Combined the notch root resistance and the averaged resistance, the total resistance that the fatigue crack has to overcome when extended from the micro-notch into the matrix grain was illustrated in Figure 5.6(b) using dashed red line. Compared with the ΔK_I distribution along the initial crack front (solid black curve in Figure 5.6(b)), the total resistance on the horizontal notch root (θ between 64º and 116º)

and around the two corners of the rectangular shape was higher, leading to negative $\Delta K_{eff,i}$ values. Therefore, in the subsequent cyclic loadings, the discrete points on the crack front in this region cannot propagate, and only those on the two vertical notch roots and away from the two corners can extend into the matrix grain, as shown in Figure 5.6(a).

Crack tip A on the surface reached GB1/2 after 37000 cycles. The resistance for the fatigue crack to propagate across GB1/2 can be calculated based on the minimum twist angle criteria [42]. With given crack plane orientation in G1 and Euler angles of G2 ([80.5º 32.5º 46º]), the ($\bar{1}$11) orientation in G2 was selected as the new crack plane orientation when tip A propagated into G2, because of its low twist angle of 22.6º among the four {111} slip planes in G2, which resulted in a resistance of $0.723 MPa \cdot \sqrt{m}$ at GB1/2, in addition to the average resistance. However, due to limited crack length at early stage of crack growth, the ΔK_I was not large enough to overcome such high resistance. Therefore, a sudden drop of growth rate to zero was obtained when crack tip A started to interact with GB1/2, as shown in Figure 5.6(c) in solid red curve. At the meantime, the crack tip B continued to propagate. As it moved ahead, namely increase of $\Delta r_{AB} = r_{tipB} - r_{tipA} > 0$, the tip B started to experience an increasing dragging force from the arrested crack front on GB1/2, according to Eq. (5.3). Its ΔK_I, on the other hand, also gradually increases as crack tip B growth. However, the increase of ΔK_I cannot compensate the increase of the total resistance that crack tip B experienced, which resulted in a decrease of the growth rate at crack tip B, as shown in Figure 5.6(c) from point p. It is worth mentioning that the decrease of the growth rate at tip B became steeper after point q (around 76000 cycles), which indicates an additional resistant source started to affect the propagation of crack tip B. The pinned crack front along the

horizontal notch root and around the two rectangular corners initially did not affect the growth of crack tip B, because their distance to the reference center (r_{pinned}) are larger than r_{tipB}. However, as the crack tip B propagated, its r_{tipB} increased and reached r_{pinned} after 76000 cycles. Therefore, the tip B started to experience the dragging force from some of these pinned points, leading to a more rapid decrease of the growth rate at tip B. Eventually, the crack tip B ceased its growth within G1 before reaching the next GB. In the simulated fatigue crack growth, the propagating distance of the crack tip B in S direction was $4.8\mu m$, which is close to the experimentally measured distance of $6.9\mu m$.

5.4.3 An example of type 1 fatigue crack

An example of type 1 non-propagating fatigue crack observed after the fatigue test was illustrated in Figure 5.7(a). The size of the micro-notch ($10\mu m$ in S direction and $14.2\mu m$ in L direction) is similar to the example of type 2 fatigue crack shown in section 5.4.2. However, due to their different matrix grain orientations, the resistance along the notch roots that the fatigue crack has to overcome in order to extend into the matrix grain were different. The Euler angles of the matrix grain in this case were [221.3º 35.7º 46.4º]. According to the minimum possible twist angle criteria [42], the ($\bar{1}11$) slip plane was selected in the model as the preferred crack plane orientation in the matrix grain with the smallest twist angle of 25.3º among the four {111} slip plane orientations, which resulted in resistances of 0.835 and 0.895 MPa $\cdot \sqrt{m}$ along the vertical and horizontal notch roots, respectively. Considering the average resistance in the material, the total resistance along the micro-notch roots was plotted in Figure 5.7(b) together with the distribution of ΔK_I. Since the ΔK_I is smaller than the resistance, $\Delta K_{eff,i} = 0$ along the entire crack front was

116

obtained leading to a non-propagating behavior of the fatigue crack. And this prediction by the model is consistent with the experimental observation shown in Figure 5.7(a).

5.5   Potential applications

By considering both local driving and resistant forces along the crack front, the current model incorporated several microstructure features, i.e. grain orientation, the size and shape of particles/micro-notches and grains, when simulating the 3-D fatigue crack growth behavior in planar slip alloys, like AA2024-T351. As demonstrated in section 5.4., with given microstructure information, i.e. initial crack geometry and orientation, grain orientations, GB position and loading condition, the model was able to select the preferred crack path/orientation when entering the next grain, and quantitatively represented the resistance exerted by the microstructure barriers it encountered. The model can also exhibit the evolution of crack front beneath the sample surface during each loading cycle, and reveal the growth rate of every discrete points along the crack front with detailed distributions of SIF and resistance as well.

As multi-site fatigue crack nucleation behaviors from second phase particles were reported in several engineering alloys [103], it became crucial to accurately identify those detrimental ones that will develop type 3 propagating fatigue cracks. Instead of a microstructure with fixed particle geometry and grain orientation, the distribution of particle width and thickness as well as texture need to be considered in order to obtain a reliable statistic prediction of the crack initiation behaviors in the material. This will greatly increase the computational burden, as the reconstruction of microstructure and the simulation of fatigue crack growth in it may need to repeat several thousands times in

117

order to obtain a steady statistical distribution. One of the advantages of the current model is the fast simulation of crack growth behavior. Therefore, different from other existing models [47, 48], the statistical effects of texture and the distribution of particle size can be taken into account in the simulation. For instance, with given texture, the distribution of resistance at interfaces/GBs can be calculated. Then for different particle size/notch dimensions, the probabilities of developing different types of fatigue cracks from these defects can be obtained. And a critical defect size can be determined by the model, below which a very low probability of type 3 propagating cracks can be achieved, i.e. less than 5%. Compared to the earlier models in which only the influence on the driving force were considered (by means of particle geometry), the current model which included a resistant term at microstructure barriers is able to explain the experimental observations that the initiation of the fatal cracks not always from the largest particles. And a more reliable critical value of particle size can be obtained.

5.6   Conclusions

- In this paper, the resistance at microstructure barriers, i.e. interfaces and GBs, toward short fatigue crack growth was quantitatively represented using the twist component of the crack plane deflection at the barrier, which depends on the crack plane orientation and the Euler angles of the neighboring grain. Based on this, a correlation function was developed to describe the dragging effect exerted on the entire crack front by the local barriers that intersected with the crack front.

- An effective driving force that included both driving and resistant forces along the crack front was used in the modified Paris power-law equation to simulate the growth behavior of short fatigue crack in 3D.

118

- Micro-notches with different dimensions were fabricated in an AA2024-T351 alloy to quantitatively study the three types of fatigue crack growth behaviors observed in the experiments. The model was able to distinguish these three different types of fatigue cracks from different micro-notches. Three examples were given to compare the simulated results with the experimental observations. And all of them show good agreement with their counterparts in the experiments.

- The model shows its potential in statistically predicting the weakest cracked particles from which the fatal fatigue crack is the most likely to be initiated.

Table 5.1. Chemical composition of the AA2024-T351 (wt.%)

Al	Cu	Mg	Fe	Mn	Si	Cr	Ti	Zn
Balance	4.1	1.4	0.45	0.43	0.43	<0.1	<0.15	<0.25

Table 5.2. The twist and tilt angles at vertical notch root for the type 3 crack demonstrated in Figure 5.4(a). (matrix grain orientation is [308.5° 36.9° 17°])

Slip plane	(111)	($\bar{1}$11)	(**1$\bar{1}$1**)	(11$\bar{1}$)
Twist angle α (°)	69.4	41.7	**3.7**	74
Tilt angle β (°)	80.1	52.1	**13.4**	6

Table 5.3. Twist and tilt angle at vertical notch root for the type 2 crack demonstrated in Figure 5.5(a) (matrix grain orientation is [246.8º 30.6º 83.5º])

Slip plane	(111)	($\bar{1}$11)	(**1$\bar{1}$1**)	(11$\bar{1}$)
Twist angle α (°)	49.9	25.7	**10.5**	82.1
Tilt angle β (°)	66	15.2	**49.6**	51.9
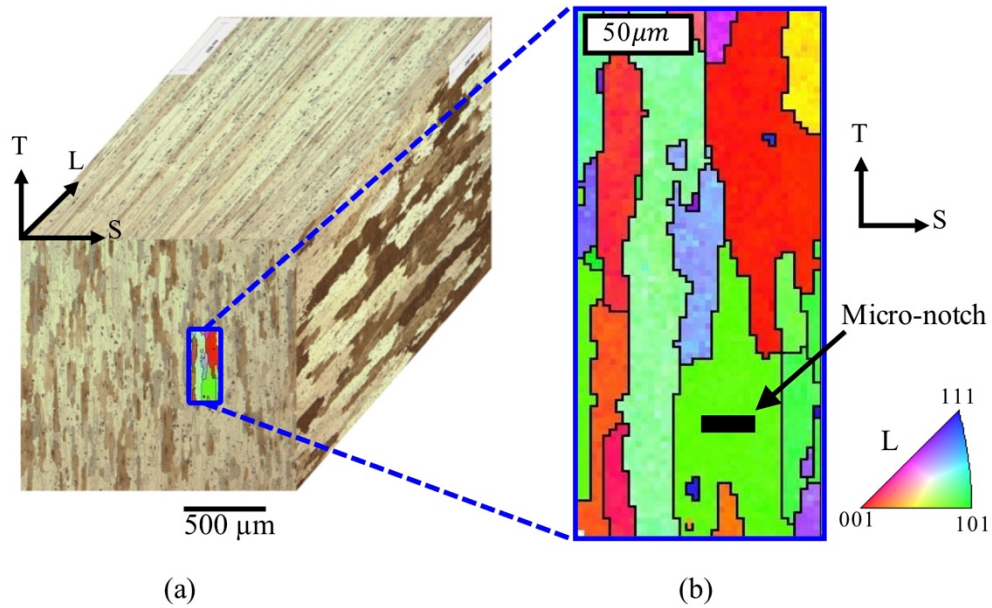
Figure 5.1. (a) Illustration of the microstructure observed on T-S, L-S and L-T planes in the AA2024-T351 Al alloy plate, and (b) IPF orientation map measured on the sample surface (T-S plane) showing relative straight GBs along T direction.
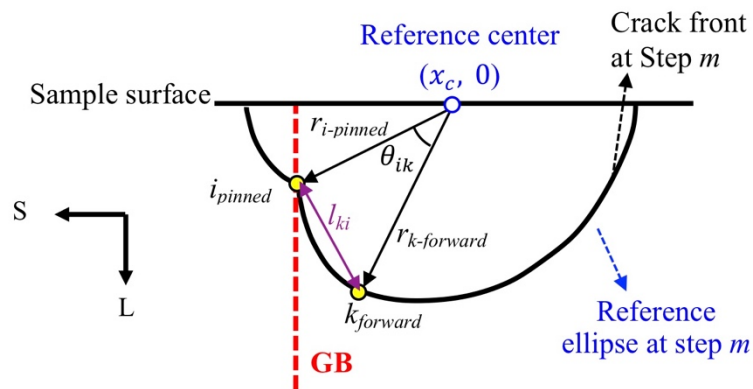
Figure 5.2. Schematic illustration of an irregular crack front beneath the sample surface.
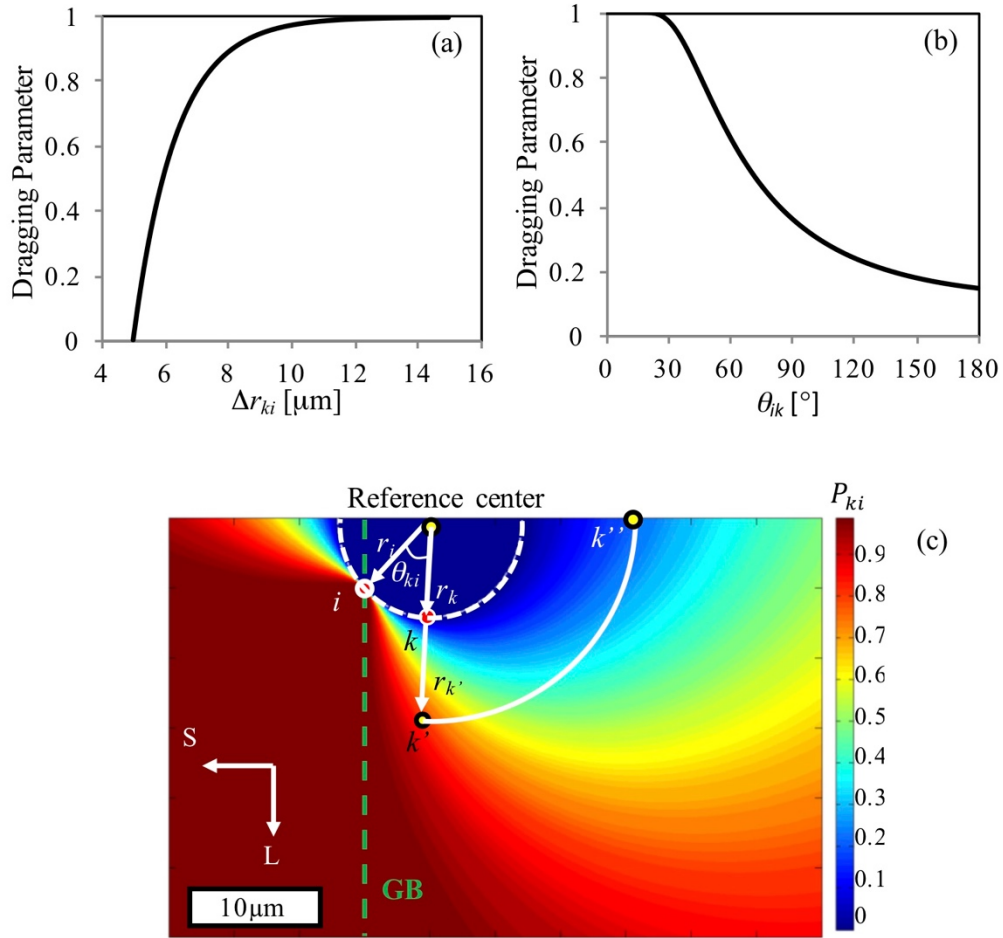
Figure 5.3. The dragging factor as a function of (a) Δr_{ki} (fixed $r_i = 5\mu m$ and $\theta_{ik} = 30°$) and (b) the angle θ_{ik} (fixed $r_i = 5\mu m$ and $r_k = 10\mu m$), and (c) The distribution of dragging parameter beneath sample surface due to pinning at point i on the crack front.

(a)

$(11\bar{1})$

$(\bar{1}11)$

$(1\bar{1}1)$

(111)

(b)

θ

S

L

$10\mu m$

(c)

(d)
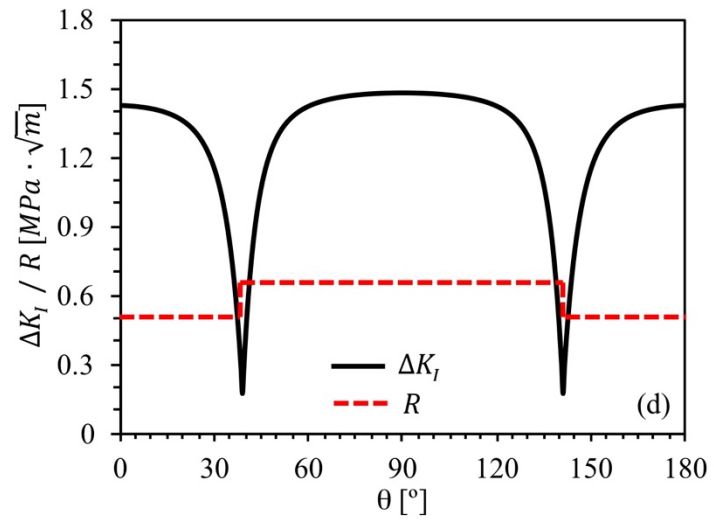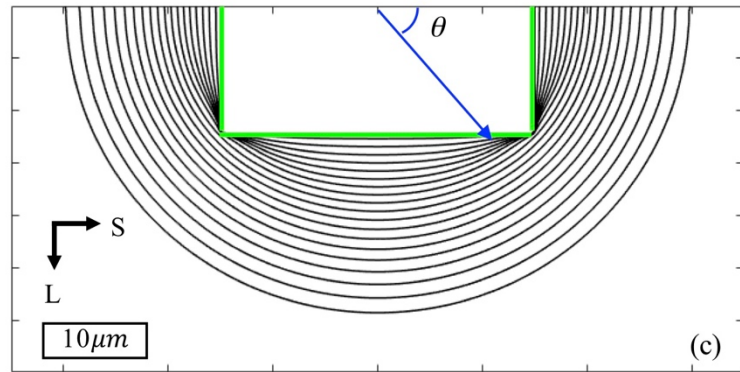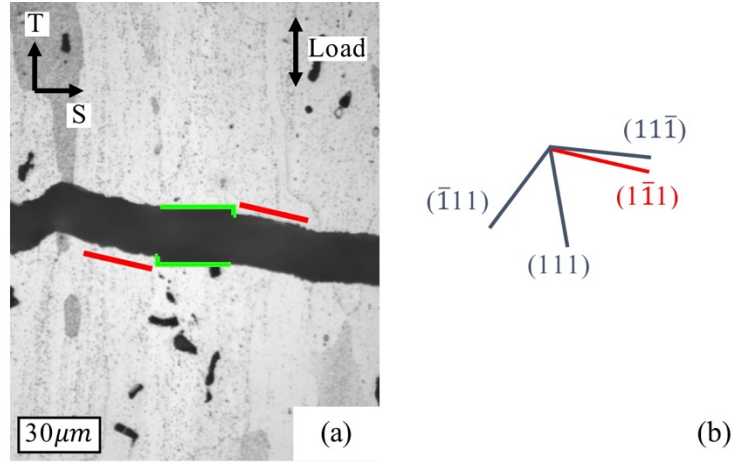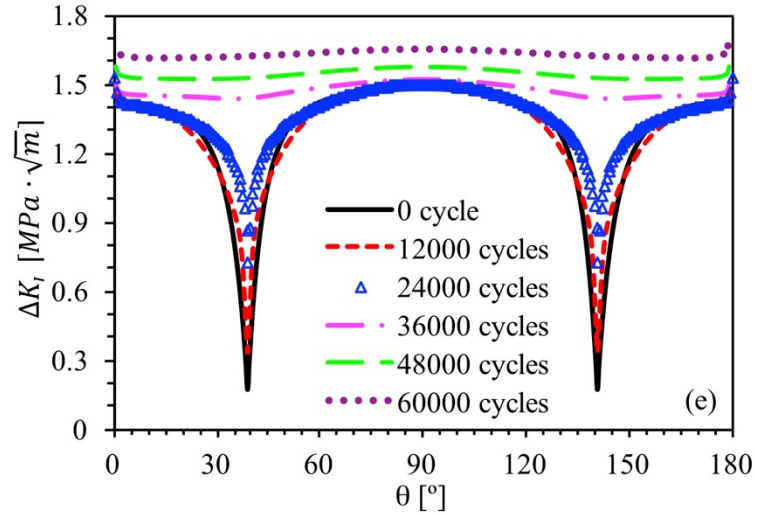
Figure 5.4. (a) An example of type-3 fatigue crack initiated from the micro-notch fabricated on T-S plane in the AA2024-T351 alloy, (b) the slip traces of the four {111} slip planes in the matrix grain on surface, (c) the simulated propagation of the fatigue crack front from the micro-notch below surface, (d) the distribution of ΔK_i and R along the roots of the micro-notch, and (e) the calculated evolution of ΔK_I along the crack front during different loading cycles.
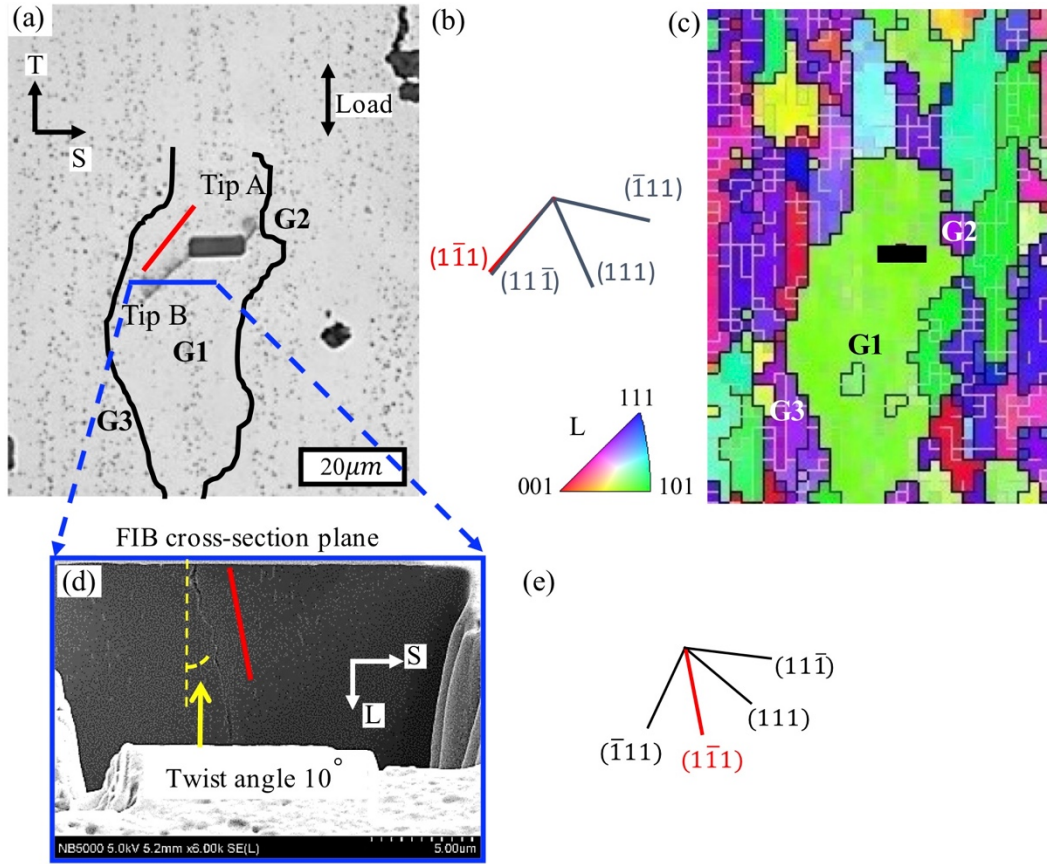
Figure 5.5. (a) An example of type-2 fatigue crack initiated from the micro-notch on T-S plane in the AA2024-T351 alloy, (b) the slip traces of the four {111} slip planes in G1 on the surface, (c) corresponding IPF orientation map at the same area as shown in Figure 5.5(a), (d) SEM image of the cross-section plane by FIB, showing the crack trace in G1 on L-S plane perpendicular to the sample surface, and (e) the slip traces of the four {111} slip planes in G1 on the FIB cross-sectioned plane.
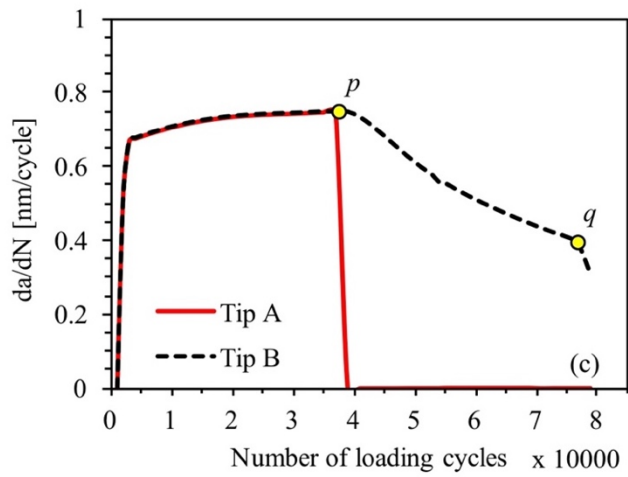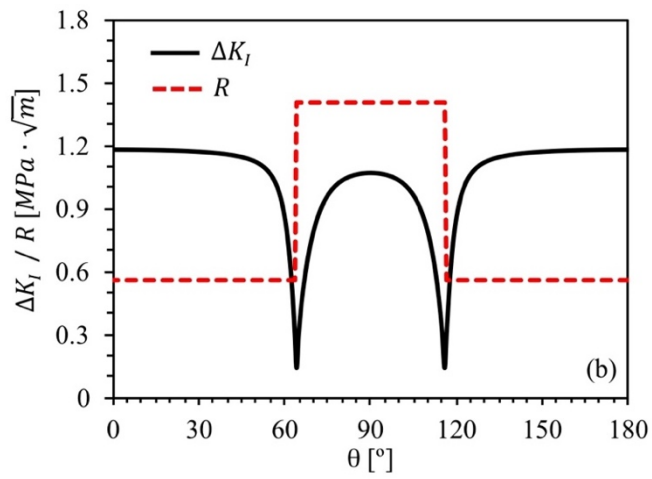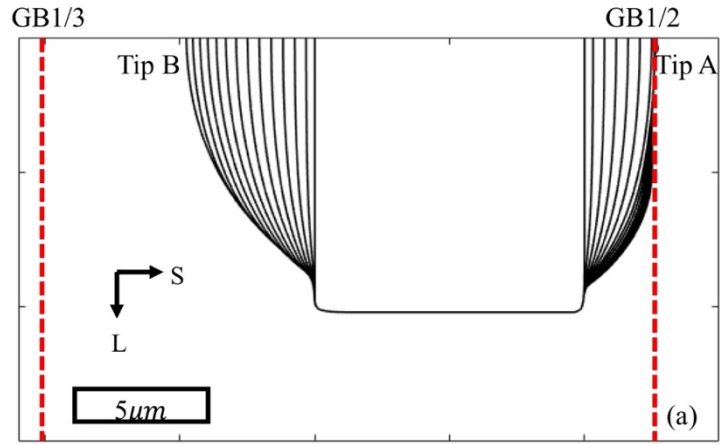
Figure 5.6. (a) The simulated propagation of the fatigue crack from the micro-notch shown in Figure 5.5(a), (b) distribution of the driving force and resistance along the notch

root and (c) the evolution of the growth rate at the two crack tips on the sample surface during cyclic loadings.
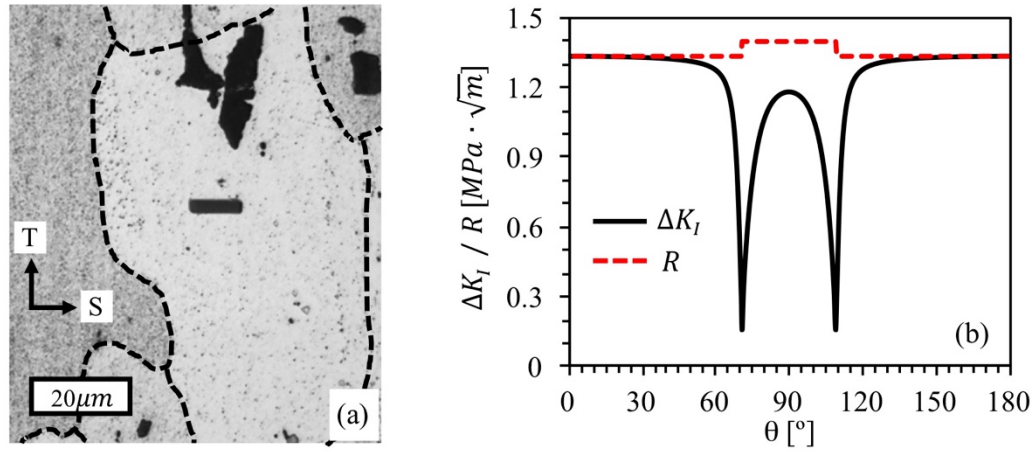
Figure 5.7. (a) An example of type-1 fatigue crack from the micro-notch on the T-S plane in the AA2024-T351 alloy, (b) the calculated ΔK_i and R along the notch root.

CHAPTER 6   Simulation of the stochastic growth behaviors of short fatigue cracks from pre-fractured particles in planar slip alloys

In the previous chapter, a microstructure-based model was developed to quantify the growth behaviors of the short fatigue crack from a micro-notch or a pre-fractured particle in planar slip alloys. In this chapter, the model is used to predict the stochastic growth behaviors of short fatigue crack from the pre-fractured constituent particles in AA2024-T3 alloy. To validate the model, the calculated crack initiation rate as well as other probabilistic behaviors of short crack growth is compared with the experimental results. Moreover, the effects of texture and grain size on the life distribution of short fatigue cracks are also studied using the current model.

6.1   Introduction

Multi-site fatigue crack nucleation behaviors from second phase particles were reported in several engineering alloys [103]. Due to the brittleness of these particles, some of them were cracked during the deformation process, and became favorite fatigue crack nucleation sites during subsequent cyclic loadings. Therefore, it becomes crucial to identify accurately those detrimental pre-fractured particles that will lead to propagating fatigue cracks. The statistical results in AA2024-T3 aluminum alloys [55] revealed that the particle thickness in the sample surface played an important role in determining the

growth behaviors of the short fatigue cracks initiated from these pre-fractured particles. When the particle thickness was smaller than 3μm, the cracks did not propagate into the matrix grain from these particles. As the particle thickness increased up to 5μm, the cracks could successfully be extended into the matrix grain, but arrested after propagated for several microns. Only the particles with thickness more than 5μm could initiate propagating fatigue cracks.

In order to understand fully the dependency of crack growth behaviors on the particle geometry, the distributions of their width and thickness as well as texture, need to be considered in theoretical simulation. This will greatly increase the computational burden, as the reconstruction of microstructure and the simulation of fatigue crack growth on computer may need to repeat several thousands times in order to obtain a statistically reliable results. One of the advantages of the model developed in this work is its timesaving method in simulation of crack growth behaviors. Therefore, different from other existing models [47, 68-70], the statistical effects of texture and the distribution of particle size can be readily taken into account in the simulation. For instance, knowing the texture, the distribution of resistance at interfaces/GBs can be readily calculated in an alloy in this work. Consequently, if pre-fractured particle/notch dimensions are known in surface, the probabilities of developing different types of fatigue cracks from these defects can be computed with the model developed in this work. A critical defect size could then be determined using the model, below which there will be a very low probability to develop the propagating cracks from the particles, i.e. less than 5%. Compared to the previously developed models which mostly are 2-D in nature [91, 92, 118, 119, 123], the current 3D microstructure-based model is able to explain the observed

behaviors of multi-site crack nucleation at particles, e.g. why the fatal cracks are not always initiated from the largest particles on surface of the alloy, since it takes into account both the driving force and resistance in simulation of the growth behaviors of the micro-cracks in the pre-fractured particles. As a result, a more reliable critical value of particle size can be obtained below which the particles could never develop fatigue cracks under an applied stress.

6.2 Experiments

The AA2024-T351 aluminum alloy plate was used in the current work. The material was hot rolled to 7mm in thickness and solution heat treated followed by natural aging. The chemical composition of the alloy was listed in Table 2.1. A pancake grain structure was presented in the alloy with average grain size of 361 x 97 x 37 μm^3 in L (rolling), T (transverse) and S (short transverse) direction, respectively. The yield stress was measured to be 358MPa along T direction. The samples prepared for the four-point bend fatigue tests (4.6 (L) x 36(T) x 8 (S) mm^3) were cut with the plane under tension-tension loading being parallel to the T-S plane, and the loading axis being along the T direction. As discussed in the previous chapter, the T-S plane was selected to avoid the interference from the pre-fractured constituent particles on the L-T and L-S plane, and ensure the initiation of fatigue crack from the micro-notches. Since the thickness of grains on the T-S sample is the largest which provides the lowest probability for the initiated fatigue cracks to interact with the GBs beneath the sample surface during its early stage of propagation, and greatly simplify the situation. The sample surface (T-S plane) under the cyclic tensile stress was ground first, then mechanically polished, before etched with the Keller's etchant.

Series of micro-notches were fabricated on the sample surface with notch plane perpendicular to the load axis (T direction), using focused ion beam (FIB) in a Hitachi NB5000 dual beam SEM/FIB system. The selection of grains where the micro-notches locate were based on two criteria: firstly, the grain size in S direction should be large enough to contain the fabricated notch which ranging between 10-40μm; secondly, the distance between selected grains should be far enough to avoid the possible shielding effects between plastic deformation zones from fatigue cracks. The corresponding grain orientations were measured with an Oxford Instrument EBSD system. In the AA2024-T351 alloy, the thickness beneath the sample surface of the pre-fractured constituent particles was the key parameter controlling the different propagating behaviors of short fatigue cracks from these particles [55]. To further investigate the geometric effects, namely the width, thickness and aspect ratio, on the propagating behaviors of short fatigue cracks, two series of micro-notches were fabricated with designed notch width (W) on surface and depth (D) beneath the surface. For the first batch of samples, constant notch width of 30μm was selected, while the depth varies from 2 to 14μm. For the second batch, similar notch depth around 10μm was fabricated with different notch width ranging from 20 to 40μm. It is worth mentioning that it is hard to obtain the exact designed notch depth, and the actual depth value was measured by identifying the narrow cross-section on the L-T plane using SEM which was 32º tilted toward the horizontal plane at tilting compensation mode until the final depth was close to the designed dimension.

The samples with micro-notches were then subjected under the fatigue tests using a self-aligning four-point bend rig [85] under a constant maximum stress of 340MPa, which is

equivalent to 95% the yield stress ($358MPa$) in the T direction at frequency of $20Hz$, stress ratio $R = 0.1$ and room temperature in air. The tests were terminated when the sample failed, namely, the maximum sample deflection exceeded a pre-defined value. And the samples were then examined using optical microscope to reveal the short fatigue crack growth behavior from the fabricated micro-notches.

6.3　Probability of a fatigue crack propagating from pre-fractured particles

With given notch width on sample surface, depth beneath the surface, notch plane orientation, grain orientation, grain size and loading condition, the microstructure-based model developed in Chapter 5 has demonstrated its ability to quantify fatigue crack growth from a micro-notch in surface, subsequently distinguish the three different types of growth behaviors of short fatigue crack from a micro-notch in the previous chapter. In this section, the influences of microstructure feature, i.e. particle size and grain orientation, on short fatigue crack growth from pre-fractured constituent particles will be quantitatively studied in an AA2024-T351 aluminum alloy using the developed model. And the probabilistic predictions of fatigue crack growth under the different distributions of particle size and texture will also be discussed and compared with the statistical results obtained in the experiments.

6.3.1　Effects of particle size

With given crack plane orientation in a pre-fractured particle and matrix grain orientation, the resistance along the particle/matrix interface was determined, therefore the effective driving force ($\Delta K_{eff} = \Delta K \text{-} R$) along the initial crack front or particle/matrix interface was merely affected by its shape and size (assume the loading condition is the same). If a

rectangular-shaped particle/micro-notch was considered, different combinations of particle width and thickness maybe result in different crack growth behaviors. Therefore, a crack propagating map can be predicted using the current model, in which the propagating types of short fatigue cracks developed from rectangular-shaped particles under different combinations of particle width and thickness were plotted. An example was given in Figure 6.1(a) where the copper orientation [0º 35º 45º] was considered as the matrix grain orientation, and the area filled with green color indicates type 1 non-propagating cracks were predicted under the corresponding particle width and thickness values in the map, while type 2 arrested cracks and type 3 propagating cracks were plotted in the map using black and red color, respectively. According to the minimum twist angle criteria [42], the model selected (111) orientation as the potential crack plane when a short fatigue crack propagated from the micro-notch into the matrix grain, leading to the minimum resistance of zero along the two vertical notch roots and $0.9MPa \cdot m^{0.5}$ along the horizontal notch root for the AA2024-T3 aluminum alloy. For the notches with relatively small width and depth, it is difficult for a short fatigue crack to extend into the matrix grain with copper orientation due to limited driving force and high resistance (both from the notch boundary and the average resistance). An example was given in Figure 6.1(b) where the distributions of driving force and resistance experienced by a micro-notch with $30\mu m$ in width and $2\mu m$ in depth was demonstrated. Comparing with the resistance, a driving force was obtained along the notch roots, which resulting in a type 1 non-propagating crack. As notch size increases, the initial driving force for crack growth enhances. Figure 6.1(c) exhibits the distribution of the driving force and resistance along the roots of a micro-notch with $20\mu m$ in width and $10\mu m$ in depth, in

which larger driving force along the two vertical notch roots was obtained compared to the resistance. Therefore, the crack was able to extend into the matrix grain from the two vertical notch roots where a relatively smaller resistance presented. But eventually their propagation ceased due to the large resistance from the horizontal notch root, resulting in type 2 fatigue cracks. Figure 6.1(d) demonstrates the propagation path of such a type-2 crack from the micro-notch beneath the sample surface. Only those micro-notches whose width and depth are large enough can successfully initiate a propagating type 3 short fatigue crack, as demonstrated in Figure 6.1(e) in which the distribution of driving force along a micro-notch with 30μm in width and 12.5μm in depth were presented. And Figure 6.1(f) shows the corresponding crack propagating path beneath the surface.

To validate the predicted crack propagating map, experiments were also conducted in the AA2024-T351 aluminum alloy by introducing micro-notches with different dimensions in the matrix grains close to the copper orientation. Two series of notches were fabricated by firstly fixing the notch width on the surface as 30μm, while varying their depth beneath the surface from 2.3μm, 7.4μm to 12.5μm, as shown in Figure 6.2(a)-(c), respectively. It is worth mentioning that it is hard to obtain the exact depth value as designed when milling a micro-notch using FIB, therefore, the actual depth of a micro-notch was determined by measuring the narrow cross-section plane beneath the surface with sample stage tilting 32º toward the horizontal plane under the tilting compensation mode in the SEM chamber. For the micro-notches with relatively shallow depth beneath the surface, namely the examples shown in Figure 6.2(a) and (b), non-propagating type 1 fatigue cracks were obtained. While propagating type 3 crack was observed for the micro-notch with depth of 12.5μm, as shown in Figure 6.2(c). In the predicted crack

propagating map shown in Figure 6.1(a), the depth and width values of the three above-mentioned examples in the experiments were highlighted using blue square markers. The predicted crack propagating types were represented using different colors which are consistent with the experimental observations in the AA2024-T351 alloy. Similarly, the second series of micro-notches were designed to have the same depth of 10μm beneath the surface, but various width on the surface. A type 3 fatigue crack was observed propagated from the micro-notch with 40μm in width and 9.9μm in depth, while a type 2 crack was developed from the micro-notch width 20μm in width and 10.4μm in depth, as shown in Figure 6.3 (a) and (b), respectively. And the predicted crack types read from Figure 6.1(a) are consistent with the experimental observations for both examples.

Based on the current experimental observations in AA2024-T351 alloy and the predicted crack propagating maps obtained from the developed model, both notch width and depth contribute when determining the crack propagating behaviors from a micro-notch. However, when a short fatigue crack propagated from a pre-fractured constituent particle in AA2024-T351, the statistical observations indicate only the particle thickness is the controlling parameter on the different types of crack growth behaviors [55]. There must be other microstructure factors also affecting the propagating behaviors of short fatigue cracks from the surface micro-notches. So far, only the copper orientation was considered as the matrix grain orientation. In the following section, the effects of matrix grain orientation and its distribution (texture) on the different crack growth behaviors will be discussed.

6.3.2 Effects of texture

Different fatigue crack propagating behaviors may be expected when the micro-notch located in the matrix grains with various orientations, due to the change of the minimum twist angle and correspondingly the boundary resistance along the notch roots. In addition to the copper orientation discussed in the previous section, the predicted propagating maps of another two matrix grain orientations were demonstrated in Figure 6.4(a) and (b), namely cube [0º 0º 0º] and brass [35º 45º 90º] orientations, respectively. For a rectangular micro-notch in cube orientated matrix grain whose plane was perpendicular to the load axis, the minimum twist angle of 45º along both vertical and horizontal notch roots were obtained, resulting in a large boundary resistance of 0.9 MPa·m$^{0.5}$ in the AA2024-T351 alloy. Therefore, compared to the map for the notches in the copper orientated matrix grain shown in Figure 6.1(a), larger notch width and depth are required in order to successfully develop a propagating type 3 crack. On the other hand, when the brass orientated matrix grain was considered, a short fatigue crack is relatively easier to extend from a micro-notch into the matrix grain, as the minimum twist angle between the notch plane and the slip plane in the brass orientated matrix grain was only 0.26º (R = 1.1x10^{-8} MPa·m$^{0.5}$) and 0º (R = 0 MPa·m$^{0.5}$) along the vertical and horizontal notch roots, respectively. Taking the micro-notch with 20μm in width and 10μm in depth for instance, a non-propagating type 1 crack was expected when the notch was fabricated in a cube orientated grain; a type 2 crack was obtained when the matrix grain orientation was copper; and a type 3 crack can successfully propagate from the micro-notch located in a brass orientated matrix grain.

For a given matrix grain orientation, the predicted crack propagating map, i.e. as shown in Figure 6.4, demonstrates its capability of distinguishing the different growth behaviors of a short fatigue crack from given micro-notch by identifying its propagating type. When the distribution of matrix grain orientation was considered, namely micro-texture, instead of a fixed orientation, the probabilities of obtaining the three different three types of fatigue cracks for a micro-notch with given combination of depth and width value (Pn_{ij}: the probability of obtaining type-n fatigue cracks from a micro-notch with notch width of i and depth of j) were expected. Figure 6.5(a) is an example showing the predicted probabilities of obtaining type 1 non-propagating fatigue crack ($P1_{ij}$) from a rectangular micro-notch with different combinations of notch width and depth under random texture, in which different colors represent various values of the probability. The dark blue color in the predicted map shown in Figure 6.5(a) indicates 0% probability of developing a type 1 fatigue crack, while dark red means 100% of obtaining a type 1 fatigue crack from a given notch size. In general, as increasing both notch width on the surface and depth beneath the surface, the probability of developing a non-propagating type 1 fatigue crack from a micro-notch gradually decreases. In contrary to the type 1 fatigue cracks, the probability of obtaining a type 3 propagating cracks shown in Figure 6.5(c) was higher as increase of notch width and depth. In Figure 6.5(b), the probability of obtaining type 2 arrested fatigue cracks under random texture was demonstrated. Instead of reaching 100%, the highest probability was only 34%, which locates around notch depth of 10μm and width of 20μm.

Figure 6.5 is an example showing the statistical effects of random texture on the predicted probabilities of obtaining the three types of fatigue cracks. In the next section,

137

the texture components measured in the AA2024-T351 alloy will be input into the model, and the simulated probabilities will be compared with the statistical observations regarding the different types of fatigue cracks from the pre-fractured constituent particles measured in the experiments.

6.3.3 Comparison of predicted probabilities with statistical results in an AA2024-T351 aluminum alloy

With given particle size and matrix grain orientation, the developed model has exhibited its capability in quantifying a short fatigue crack growth from the pre-fractured particles in planar slip alloys. However, during alloy design, instead of determining the growth behaviors of fatigue crack from each pre-fractured particle in the alloy, a cracking rate is more straightforward when evaluating the initiation/propagation behaviors of fatigue cracks, which is the ratio of the number density of fatigue cracks over the particles. Hillberry et al. [54, 124] statistically studied the initiation of fatigue cracks from constituent particles in AA2024-T351 aluminum alloy, where the fatigue crack nucleation rate which is the number of fatigue cracks over the total number of particles on the sample surface was determined as 0.32%. Since the majority of the fatigue crack initiated from the pre-fractured Fe-containing particles, the fatigue crack nucleation rate from pre-fractured particle ($Rt1$) was considered by diving the the particle cracking rate by the particle cracking rate. In the work done by DeBartolo and Hillberry [124], the particle cracking rate which is the number of cracked particle over the total number of particles was measured as 3.00%, which leading to a fatigue crack nucleation rate from pre-fractured particles of 10.53% in the AA2024-T351 aluminum alloy. Next, the measured distributions of microstructure in the AA2024-T351 alloy, namely, texture,

particle width and thickness distributions, will be input into the model, and the statistical predictions of different growth behaviors of short fatigue cracks from the pre-fracture particles will be compared with the experimental results.

Different from random texture discussed in section 6.3.2, a rolling-type of texture was measured in the AA2024-T351 aluminum alloy. The volume fraction of each texture components in the alloy were listed in Table 6.1 and input into the model when simulating the growth behavior of a short fatigue crack from a pre-fractured particle on surface. The corresponding predicted maps showing the probabilities of obtaining type 1, 2 and 3 fatigue cracks were demonstrated in Figure 6.6(a), (b) and (c), respectively. In general, as increase of notch width and depth, the probability of developing a type 1 fatigue crack gradually decreases, while the probability of having a type 3 crack increases. Compared to the predicted results with random texture, as shown in Figure 6.5, the change of the probabilities for type 1 and 3 cracks are more rapid as notch width and depth increase. For instance, when the rolling-type of texture was input, the probability of obtaining a type 3 propagating fatigue crack quickly reaches 80% when notch size increases to D=18μm and W=20μm, while notch size of D=30μm and W=32μm are required in order to achieve 80% probability of developing a type 3 crack under random texture. Moreover, the highest probability obtaining a type 2 fatigue crack increases from 34% in random texture to 44% in the rolling-type of texture.

Experimentally, the fatigue crack propagating behaviors at particles with different width on the surface and thickness beneath the surface were also investigated. For different types of fatigue cracks from the particles, their corresponding particle width and thickness were plotted in Figure 6.7. The type 1 non-propagating cracks are always

associated with the particles with shallow thickness beneath the sample surface. As increase of the thickness, type 2 arrested fatigue cracks are more likely to obtained in the AA2024-T3 alloy. And only for those particles with large thickness can successfully initiate a propagating type 3 fatigue crack. For each type of fatigue cracks, if mapping these experimental data points onto their corresponding predicted probability maps, as shown in Figure 6.6(a)-(c), it can be seen that the model successfully captures the general trend, as these experimental data points locate in the regions with relatively high probabilities.

To better evaluate the fatigue properties of the material, the distributions of particle width and thickness, in addition to texture, were considered when calculating the probabilities of obtaining the different types of fatigue cracks in the given alloy. DeBartolo and Hillberry [124] have statistically described the pre-fractured particles size distribution in the AA2024-T3 alloy (as shown in Figure 6.8) using lognormal distributions as

$$g(x) = \frac{1}{x\sigma\sqrt{2\pi}} exp\left[\frac{-(ln\,x - \mu^2)}{2\sigma^2}\right]$$

in which σ is the shape and μ is the scale. For the particle width on the surface L-T plane, $\sigma = 0.603$ and $\mu = 1.823$, and for half particle thickness perpendicular to the sample surface on T-S plane, $\sigma = 0.408$ and $\mu = 1.056$. With the width and thickness distributions, namely $g_1(w)$ and $g_2(t)$, respectively, the probability of obtaining a type-n fatigue crack at a pre-fractured particle can be calculated as

$$Pn = \iint f_n(w,t) \cdot g_1(w) \cdot g_2(t)\, dwdt$$

in which $f_n(w,t)$ is the probability of obtaining a type-n fatigue crack from a pre-fractured particle with width of w and thickness of t. With input of texture and pre-fractured particle size distributions for the AA2024-T3 alloy, the calculated probabilities of having a type 1, 2 and 3 fatigue crack were *P1*=77.0%, *P2*=12.8% and *P3*=10.2%, respectively. *P3* can also be interpreted as the crack nucleation rate from the pre-fractured particles which was the number of type 3 fatigue cracks divided by the total number of the pre-fractured particles in the alloy, therefore can be directly compared to the experiments. For the AA2024-T3 alloy, the crack nucleation rate was measured as 10.5% in the experiment which shows a good agreement with the predicted one of 10.2% using the developed model.

6.4 Life distribution of short fatigue cracks

For those type 3 fatigue cracks successfully propagated from the pre-fractured particles, with given grain structures information, the model is able to quantify their short fatigue crack life. For the AA2024-T3 aluminum alloy studied in this work, elongated grain structure was observed with average grain size of 361 x 97 x 37 μm^3 in L (rolling), T (transverse) and S (short transverse) direction, respectively. As the grain size in L direction is much larger than it in the T and S direction, a pancake-shaped grain structure with flat grain boundaries (GBs) plane parallel to the L-T plane was first considered in the simulation. An initial semi-penny shaped micro-crack of 5μm in radius was included in grain center on the sample surface. The crack plane is normal to the loading axis, L-direction, which has the same orientation as those cracks in the pre-fractured particles on the L-T plane in Al-Cu and Al-Zn alloys [55]. The loading condition and parameters are the same as those in Chapter 5. The number of loading cycles for such a crack to reach

500μm in length is referred as the short fatigue crack life in this work. And the life distribution of short fatigue cracks is influenced by microstructures as well, therefore, in the following sections, the effects of texture and grain size on the life distribution of short fatigue crack will be discussed in details.

6.4.1   Effects of texture

Firstly, the grain orientations were randomly assigned for the layered grain structure with grain size of 20μm. The growth of short fatigue crack from the surface micro-crack under such grain structure was quantified using the current model. This simulation was repeated 1000 times to achieve statistically valid growth behaviors of short fatigue cracks. For a better graphic presentation of the simulated results Figure 6.9 shows only 40 out of 1000 simulated crack growth curves, namely the half crack length on surface over loading cycles (a-N curves). It is evident in Figure 6.9 that the lives of short fatigue cracks at the length of 500μm on surface are scattered between 0.95×10^5 and 1.7×10^5 cycles, and distributed preferably around 1.0×10^5 and 1.65×10^5 cycles. The crack retardation (i.e. the crack length remains the same for a large number of loading cycles at GBs) occurs most significantly at the first GB that the crack encounters, due to its limited driving force at the early stage of crack growth. As crack propagating, the retardation gradually become less significant at the subsequent GBs and hardly noticeable after the half crack length reaches 100μm, as indicated in Figure 6.9. A bimodal distribution of short fatigue crack lives was obtained for such grain structure under random texture, as illustrated in Figure 6.10(a), in which the probability of the crack life at surface length of 500μm was plotted as a function of load cycle. The probabilities at the left ("short life") peak and right

142

("long life") peak were close which were 25% and 31%, respectively. The bimodal life distribution of short fatigue cracks indicates that for the same batch of alloys subjected under same loading conditions, the growth of a short fatigue crack could exhibit one of the two characteristic lives round the left and right peaks. From the crack growth curve shown in Figure 6.9, it is evident that the first few of GBs that crack encountered during its propagation exhibit more significant influence on its growth behavior. To better understand the influences on the life of short fatigue crack, the twist angles at the first three GBs that the crack encountered were statistical analyzed. Figure 6.11 demonstrates the relationship between the life of short fatigue crack with the average twist angles at the 1st, 2nd and 3rd GB. It can be seen that the longer life of a short fatigue crack is attributed to the higher twist angle/GB resistance at the 1st GB, and a monotonic relationship between the average α angle at the 1st GB and the life of short fatigue crack was obtained. Therefore, the right peak of the life distribution shown in Figure 6.10(a) is always associated with a larger GB resistance at the 1st GB with an average α angles of 35.7º, while the left peak of the lift distribution is the resultant of a much smaller α angles of 6.7º. Unlike the 1st GB, the life of short fatigue crack does not show strong dependency on the twist angles at the 2nd and 3rd GBs, as shown in Figure 6.11.

In addition to random texture, a recrystallization-type and a rolling-type of texture in aluminum alloys were also considered, which contain primarily six texture orientations, namely, Brass [35º 45º 90º], S [59º 34º 65º], Copper [90º 35º 45º], Cube [0º 0º 0º], Goss [0º 45º 0º] and R-cube [45º 0º 0º], and their volume fractions for different texture combinations were listed in Table 6.1. The grain orientations were randomly assigned within 10º deviations around the six ideal texture orientations in Euler space under the

constraint that the volume fractions of texture components were statistically consistent with the texture combinations listed in Table 6.1. The corresponding life distributions of short fatigue cracks were exhibited in Figure 6.10(b) and (c) for the recrystallization-type (combination 2) and rolling-type of textures (combination 3), respectively. Similar to the random texture, the lives of short fatigue crack under these two texture combinations also exhibit bimodal distributions in which the positions for the left and right peaks are the same. For the texture combination 2, the probability at the "long life" peak reaches 60% which is much higher than the value at the "short life" peak of 21%. However, when rolling-type of texture was considered, the "short life" peak exhibits a higher probability of 56%, while the probability at the "long life" peak is only 5%. Compared to random texture, a statistically longer life of a short fatigue crack would be achieved when the crack propagated in the grain structures with recrystallization-type of texture, while a shorter life of a short fatigue crack would be expected when rolling-type of texture was considered.

When different textures were considered, the probability of the life distribution of short fatigue crack changes, especially around the position of the left and right peaks. Since it is known that the twist angle at the 1st GB plays an important role in determining the life of a short fatigue crack, the minimum twist angle at the 1st GB was calculated when different crystal orientation was considered for the neighboring grain of the initiation site, as shown in Figure 6.12 where the neighboring grain orientations [φ_1 Φ φ_2] was plotted in the Euler space as a series of φ_1-Φ sections each of which has a constant value of φ_2, and the calculated value of twist angle was represented using different colors. To understand the influences of texture on the life distribution of short fatigue cracks, the six

ideal texture orientations were marked in the figure, among which the three typical orientations after rolling all exhibit small twist angles, namely $\alpha=0^{\circ}$ for Copper, 4.9° for S and 0.26° for Brass orientation, while the Cube and R-cube orientation in the recrystallization-type of texture show large twist angles of 45° and 35.3°, respectively. Therefore, when the crystal orientation of the neighboring grain exhibits Cube or R-cube orientation, a large GB resistance would be expected at the 1st GB, leading to a longer life of the short fatigue crack. For the recrystallization-type of texture with high volume fractions of Cube and R-cube texture components, there are higher probability that the 1st GB the crack encountered has a large value of twist angle, which explains the higher probability of the "long life" peak in the life distribution of short fatigue cracks shown in Figure 6.10(b). Similarly, a small twist angle would be expected when the neighboring grain has a typical rolling orientation, i.e. Copper, S or Brass. Thus, there are higher probability that the 1st GB the crack encountered has a small value of twist angle, resulting in a higher probability of the "short life" peak in the life distribution shown in Figure 6.10(c).

6.4.2   Effects of grain size

The effects of grain size on short crack growth were quantified using the model in this work. Layered grain structures with six different grain thicknesses ranging from 10μm to 35μm were studied. The life of an initial crack was quantified in each of these six grain sizes (GSs) which were assigned a random texture. The corresponding life distributions of short fatigue cracks were demonstrated in Figure 6.13(a)-(f). A bimodal distribution of short fatigue crack life was obtained when grain size of 20μm was considered, in which

145

the left "short life" and right "long life" peak locate around 10^5 and 1.7×10^5 cycles, respectively. As increase of grain size, the position of the "short life" peak remains relatively the same, while the "long life" peak gradually shifts to the left indicating a shorter life of short fatigue crack, as shown in Figure 6.13(c)-(f). When the two peaks are close enough, they start to merge together. Eventually, an unimodal distribution is obtained when the grain size increases to 35μm. In the previous section, it has been shown that the bimodal distribution of the life was primary attributed to the resistant that the short fatigue crack experienced at the 1st GB. And the short fatigue crack with a "long life" is always associated with a large twist angle at the 1st GB. Due to limited crack length at the early stage of crack growth, the driving force was small, therefore, the influences of the resistance at the 1st GB cannot be neglected when determining the crack growth behavior using the effective driving force, which is the driving force minus the resistance. However, as increase of grain size, the crack length at the 1st GB also increases, leading to a higher driving force when the crack interacts with the 1st GB. For instance, the driving force that a short fatigue crack experienced is 0.89 MPa·m$^{0.5}$ when it encountered the 1st GB in GS=20μm, but this value increases to 1.78 MPa·m$^{0.5}$ when GS=40μm. Therefore, when determining the effective driving force, the resistance at the 1st GB becomes less significant, which explains the shift of the "long life" peak of the life distribution to the left.

In the grain structure with grain size smaller than 20μm, only the "short life" peak was obtained, as shown in Figure 6.13(a) and (b). Unlike the unimodal distribution for the grain size of 35μm in which the probability of the left peak reaches 55%, the probabilities at the left peak for these two grain size conditions are around 10%. This can be better

understand from the cumulative probability of the short fatigue crack life, shown in Figure 6.13(g). It can be seen that the cumulative probability varies between 0 to 1 when grain size is larger than 20μm, in contrast to 0 to 0.34 and 0 to 0.44 in GS=10μm and 15μm, respectively. In other words, 66% and 56% of the cracks were fully arrested before reaching 500μm long on the surface in GS of 10μm and 15μm, respectively. As explained earlier, the influence of the 1st GB resistance increases as decrease of grain size. For the layered grain structure with small grain size, the driving force at the 1st GB which is limited by the crack length could be smaller than the GB resistance, and the short fatigue crack cannot overcome the GB, therefore arrested in front of the 1st GB. If the grain size is small enough, it is possible that not only the 1st GB, but also the 2nd and even the 3rd GB exhibit strong influences on the growth behavior of a short fatigue crack. In Figure 6.14, the relationship between the life of short fatigue crack and the average twist angle at the 1st, 2nd and 3rd GB that the crack encountered were plotted in GS=10μm. It can be seen that the life of short fatigue crack gradually increases as the twist angle at the 1st GB increases, until it reaches 14º above which the short fatigue crack cannot propagate across the 1st GB but arrested in front of it. Unlike the results in GS of 20μm, the average twist angle at the 2nd and 3rd GB dose not remain a constant value. Take the marked region I in Figure 6.14 for example, while the average twist angles at the 1st and 3rd GB remain relatively constant around 12º and 18º, respectively, the enhance of the life of short fatigue crack was attributed to the increase of the average twist angle at the 2nd GB. In the region II marked in Figure 6.14, the life of short fatigue crack depends on the twist angle at both 2nd and 3rd GB, while the average twist angle at the 1st GB remains the same.

The microstructure-based model developed in this work has demonstrated its ability in predicting the life of short fatigue crack in different textures and grain sizes in planar slip alloys. The model can also be used for optimizing the texture through maximizing the GB resistance in the alloy. However, other factors, i.e. tilt angle, Schmidt factor, and the effects of grain orientation on crack initiation, grain size-grain orientation correlation etc., may also need to be incorporated into the model.

6.5   Conclusions

- The 3D microstructure-based model was used to quantitatively study the effects of grain orientation, particle width and thickness on the growth behavior of short fatigue crack from a pre-fractured constituent particle in planar slip alloys.

- For a given microstructure orientation, the fatigue crack propagating behaviors from particles with different combinations of particle width and thickness were predicted, which were consistent with the experimental observations.

- The developed model was able to predict the probabilities of obtaining the three different types of fatigue cracks propagated from the pre-fracture particles with different combinations of the particle width and thickness with given texture.

- The simulated probability of obtaining a type-3 propagating fatigue crack from the pre-fractured constituent particles in AA2024-T3 was 10.3% which can be directly compared to the crack nucleation rate measured in the experiments, which shows a good agreement.

- The consistency between the simulated and experimental results validates the capability of the model in quantifying the texture and particle size effects on the

growth behaviors of short fatigue cracks from the pre-fractured particles in planar slip alloys.

- For those cracks successfully propagated into the matrix grains from the pre-fractured particles, their subsequent growth behaviors in the engineering alloys with different textures and grain sizes were also studied using the current model. The results showed that the grains with recrystallization-type of texture can exert more resistance against the short fatigue crack growth, comparing to random and rolling-type of textures. And depending on grain size, the first few GBs that a short fatigue crack encountered can significantly prolong the life of short fatigue crack.

Table 6.1. Volume fractions of the texture components measured in the AA2024-T351 Al alloy

Grain orientation	Brass	S	Copper	Cube	Goss	Random
Vol%	4%	19%	11%	2%	3%	balance

Table 6.2. Three different combinations of texture components made in the digital microstructure.

Grain orientation	Brass	S	Copper	Cube	Goss	R-cube	Random
Combination 1 (random texture)	-	-	-	-	-	-	100%
Combination 2 (recrystallization-type of texture)	5%	5%	5%	50%	5%	30%	-
Combination 3 (rolling-type of texture)	30%	30%	30%	4%	4%	2%	-

(a)

(b)

(c)

(d)

5μm

(e)
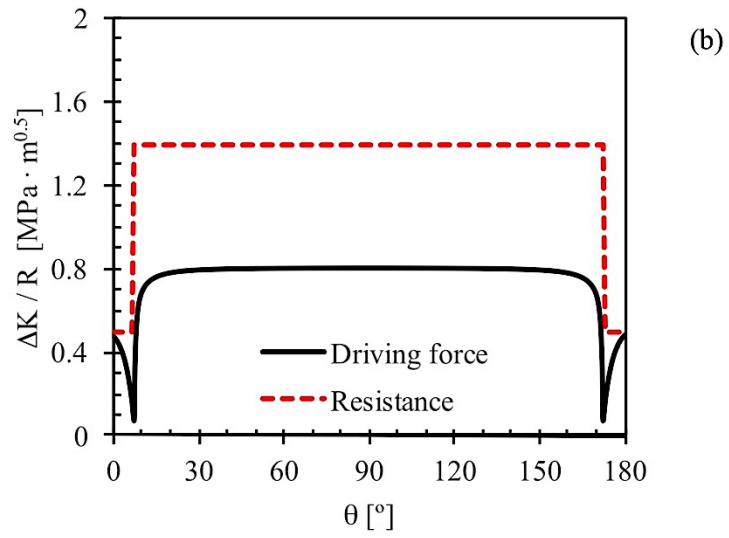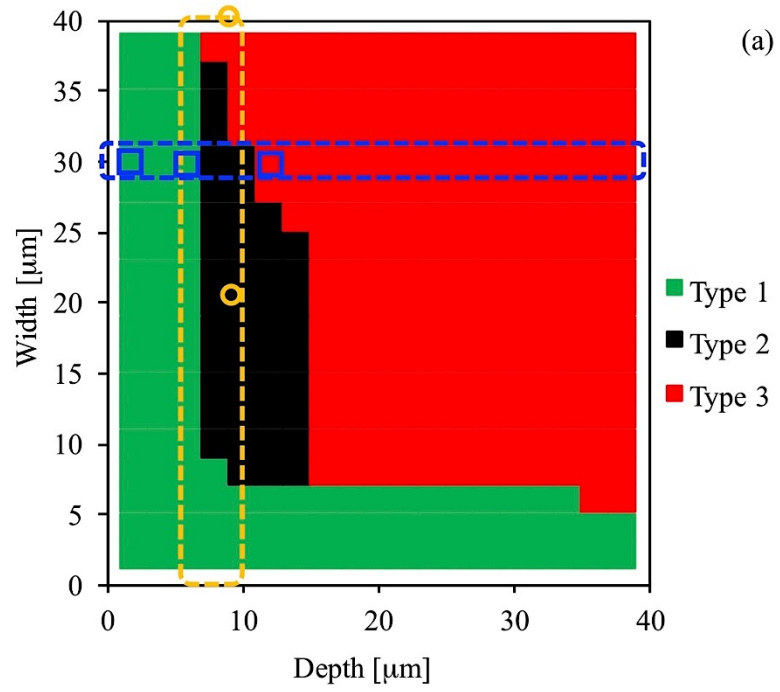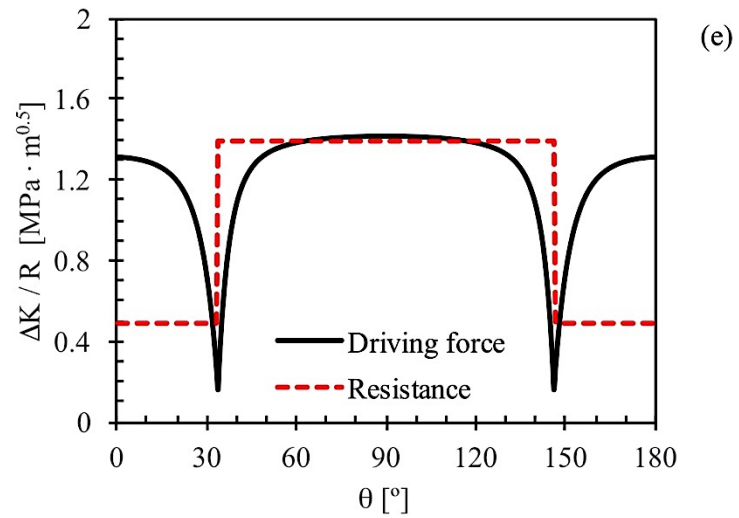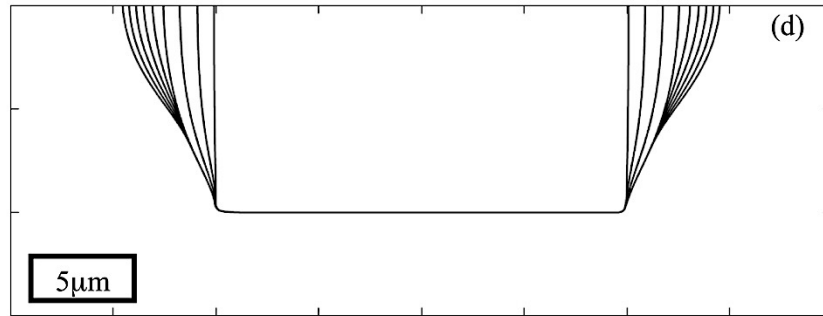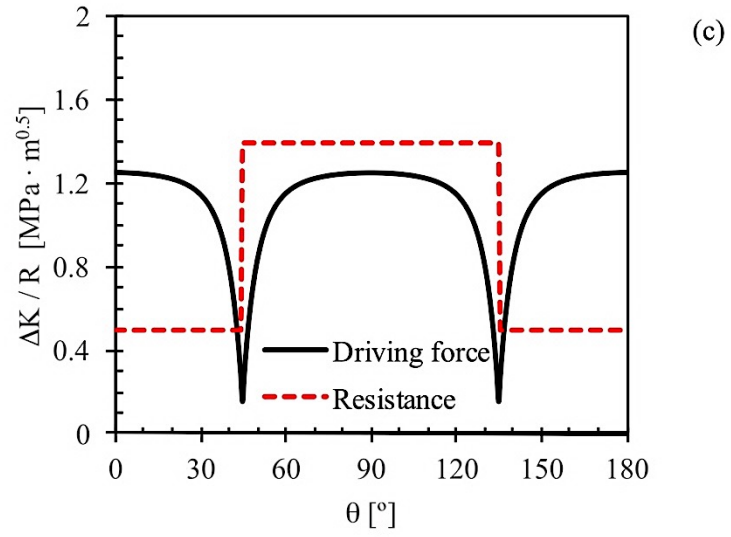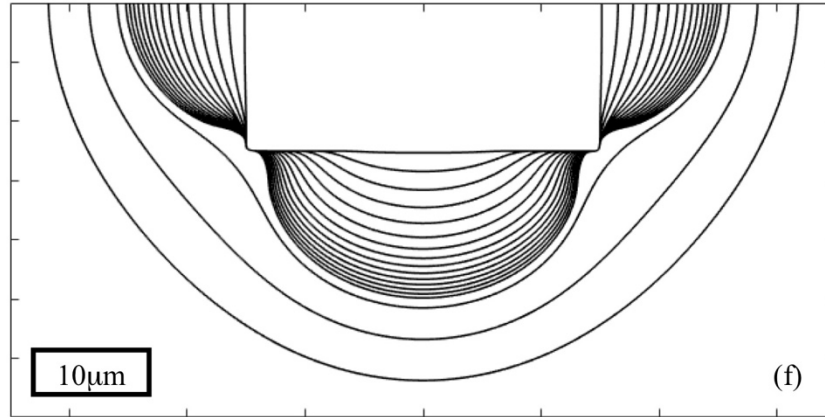
Figure 6.1. (a) The predicted map of short fatigue crack propagation behaviors from rectangular micro-notches with different combinations of width and depth located in copper orientated ([0° 35° 45°]) grain in the AA2024-T351 alloy. (b), (c) and (e) The calculated distributions of driving force and resistance along micro-notches with geometries of 30 μm x 2 μm (width x depth), 20 μm x 10 μm, 30 μm x 12.5 μm, respectively. (d) and (f) The predicted crack propagation profiles beneath the sample surface from micro-notches with geometries of 20 μm x 10 μm, 30 μm x 12.5 μm, respectively.
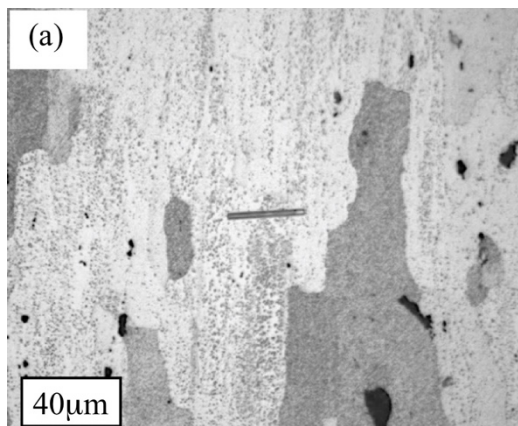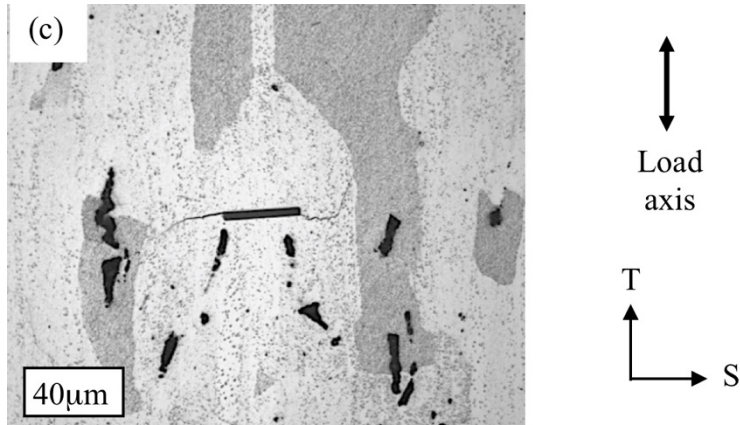
Figure 6.2. Three examples of micro-notches with same width of 30 μm on surface but different depths beneath the surface (all of them are located in the grains with copper orientation), (a) 2.3 μm, (b) 7.4 μm and (c) 12.5 μm.
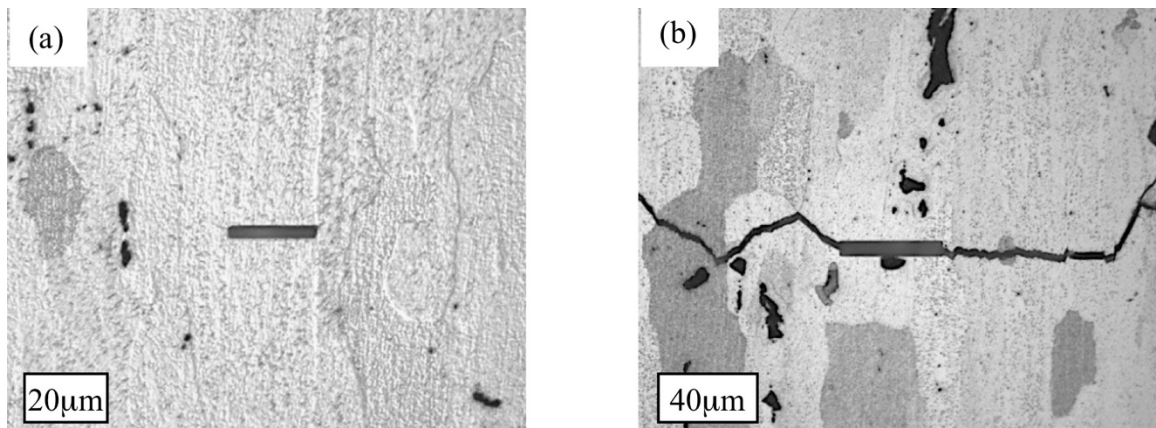
Figure 6.3. Two examples of micro-notches with similar notch depth around 10μm beneath the surface but different widths on the surface (both of them are located in the grain with near copper orientation), (a) 20 μm and (b) 40 μm.

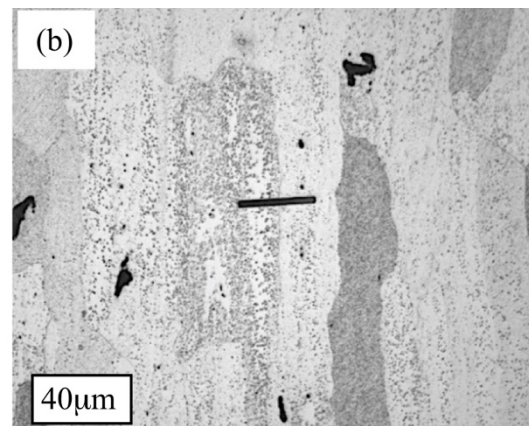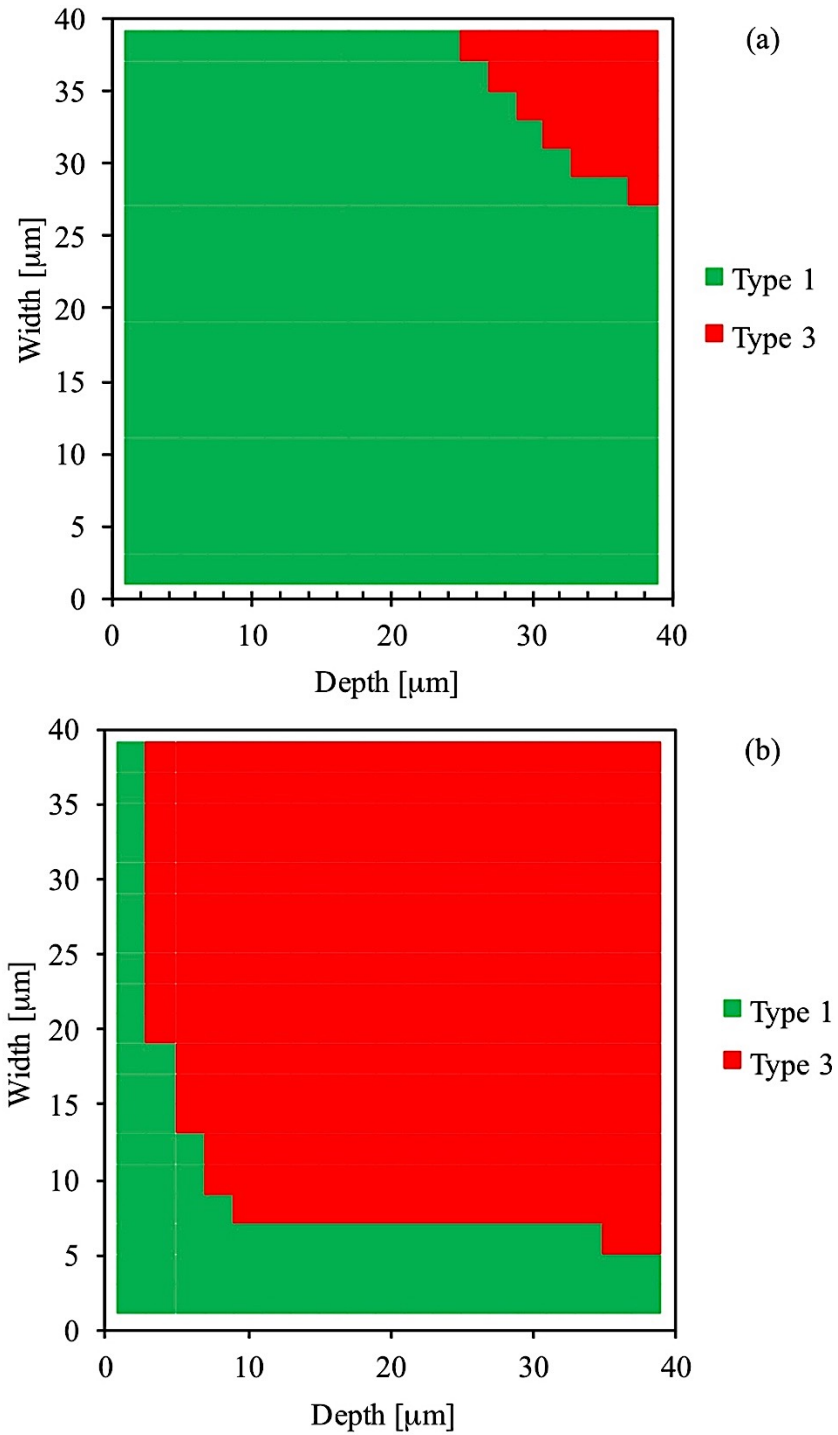**Figure 6.4**. The predicted maps of short fatigue crack propagation behaviors from rectangular micro-notches in (a) a cube orientated ([0º 0º 0º]) grain and (b) a brass orientated ([35º 45º 90º]) grain for an AA2024-T351 alloy.

(a)

(b)
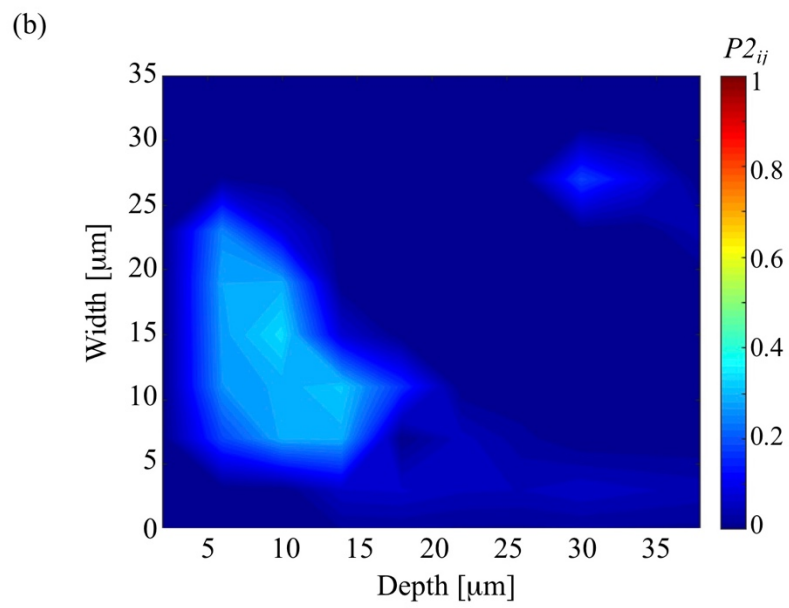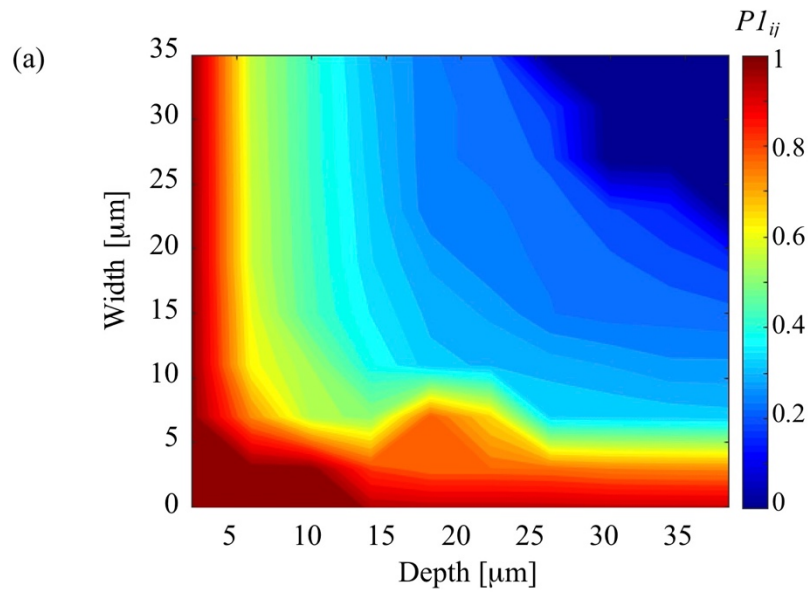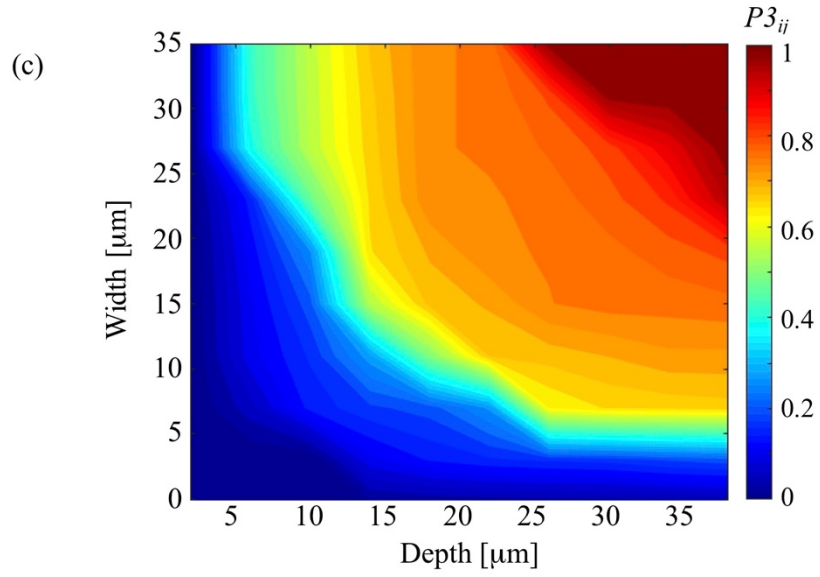
Figure 6.5. The predicted probabilities of obtaining (a) type 1, (b) type 2 and (c) type 3 fatigue cracks from rectangular micro-notches in a random texture.
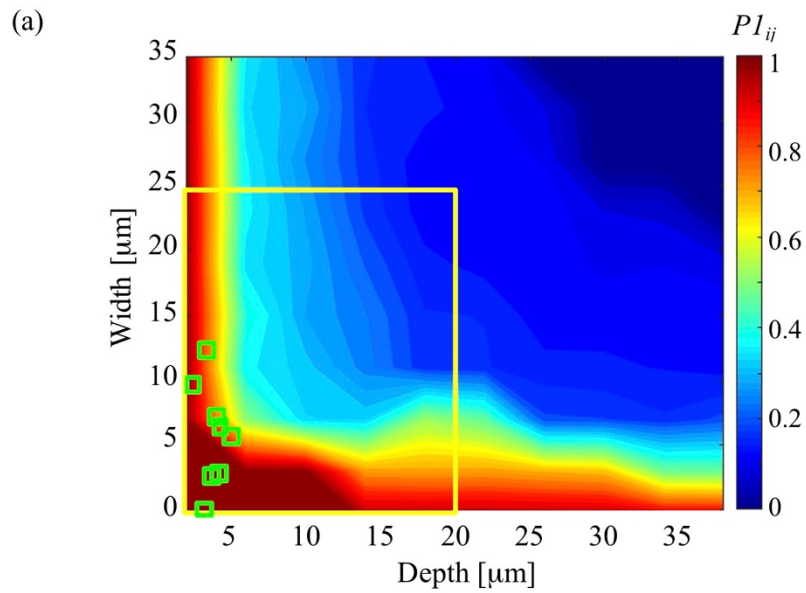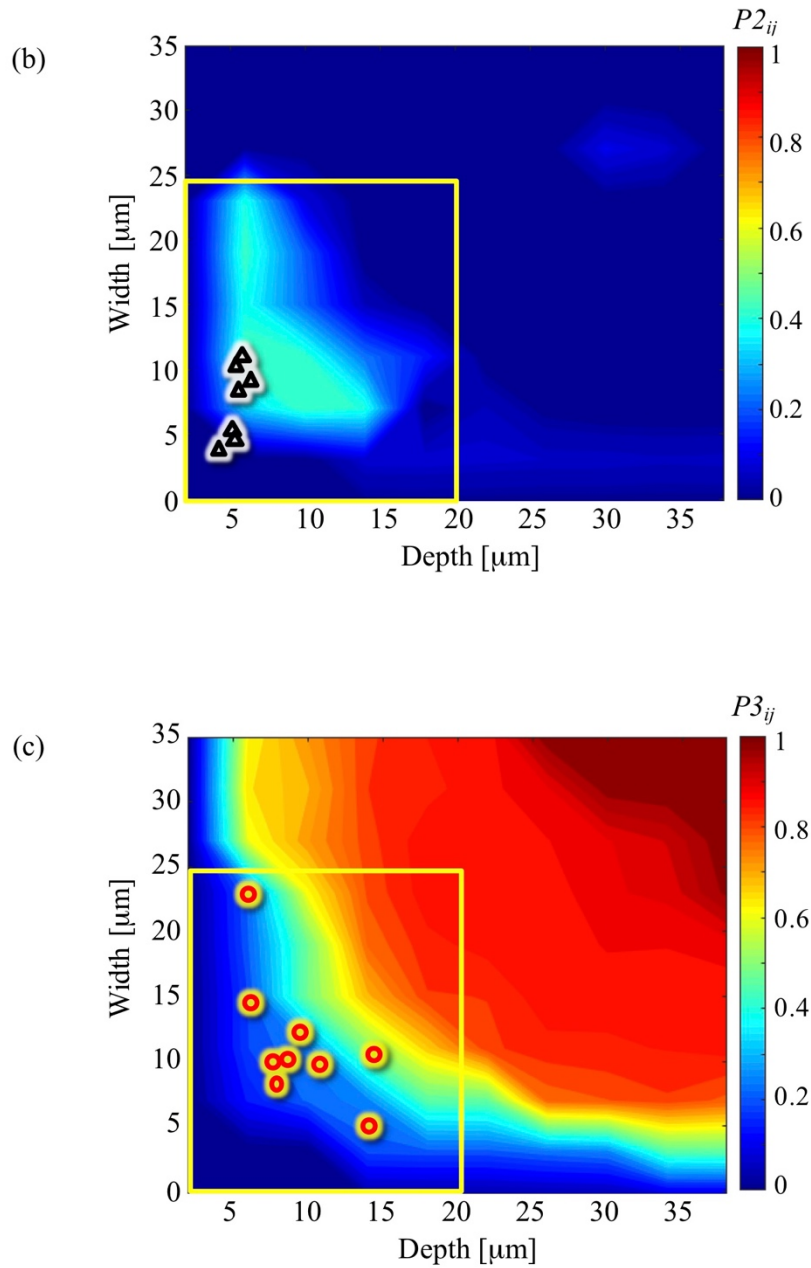
Figure 6.6. The predicted probabilities of obtaining fatigue cracks of (a) type 1, (b) type 2 and (c) type 3 from the rectangular micro-notches in the grain structure with a rolling-type of texture.
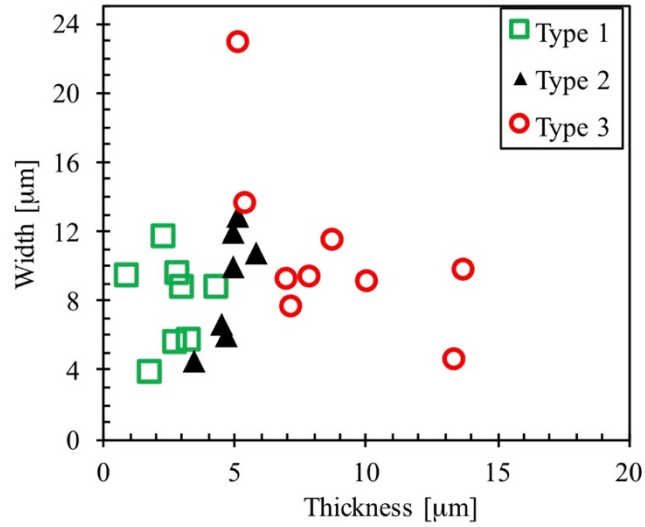
Figure 6.7. Experimentally determined thickness beneath the surface and width on surface of the particles initiating fatigue cracks in the AA2024-T3 aluminum alloy.
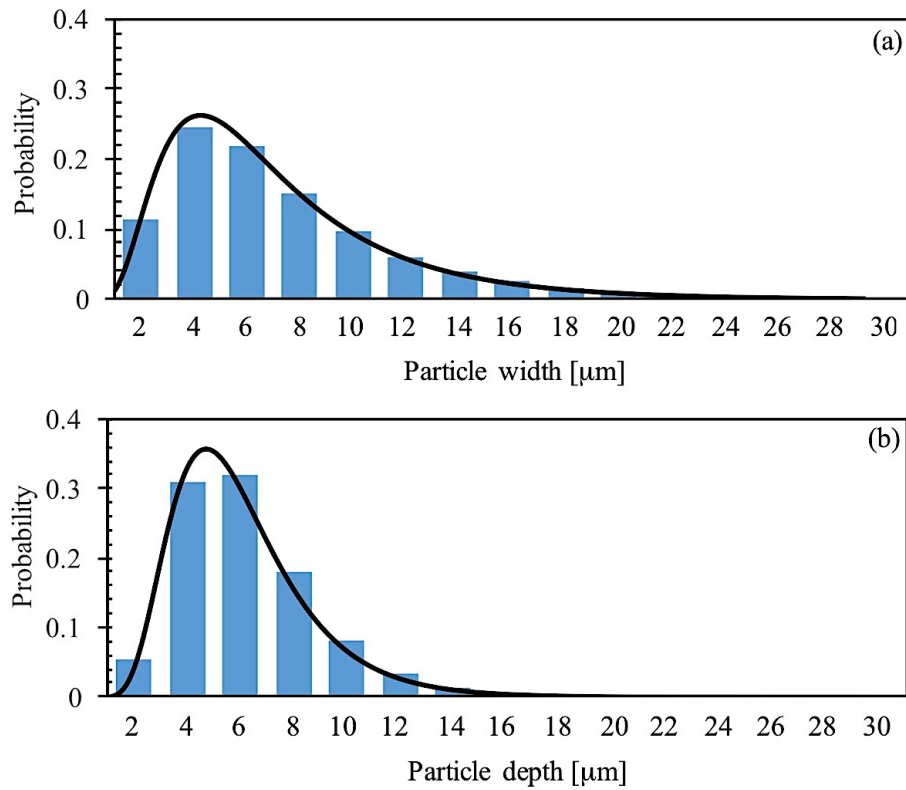
Figure 6.8. Lognormal fits to the pre-fractured constituent particles (a) width and (b) thickness distributions in the AA2024-T3 alloy [124]
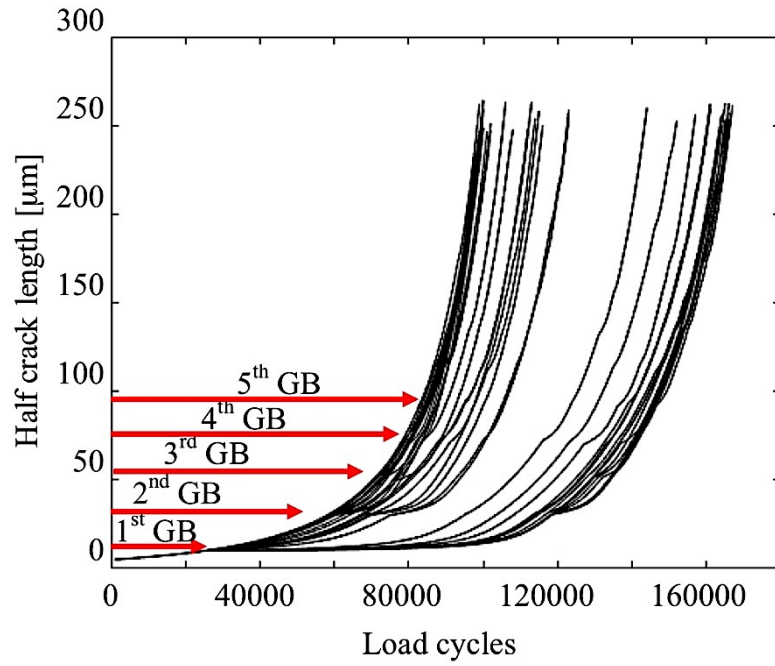
Figure 6.9. Simulated plots of half crack length on surface vs. load cycles in a layered grain structure with a random texture and grain size of 20 μm.
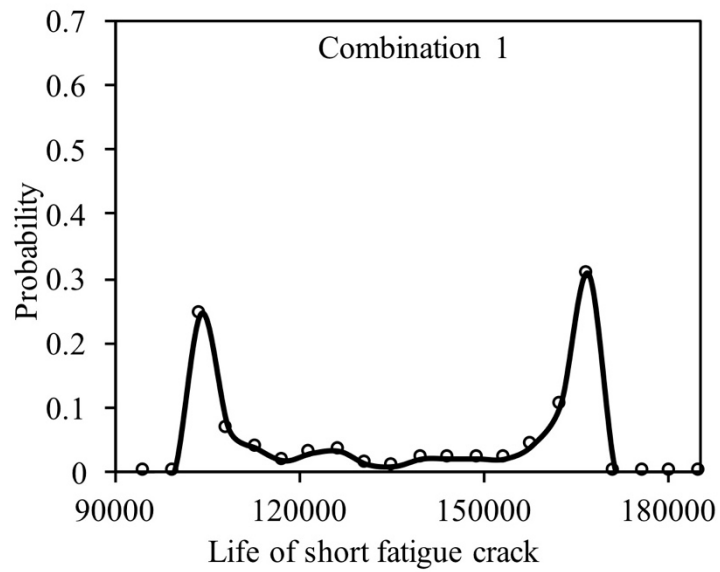
(a)
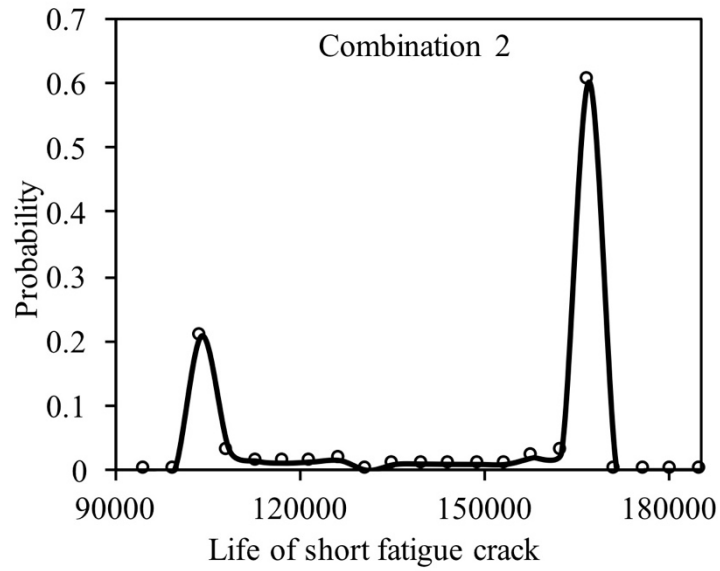
(b)
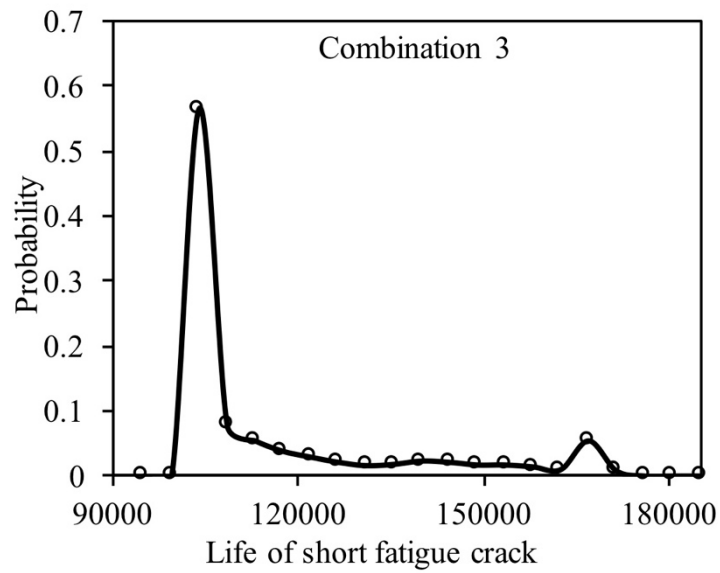
(c)

Figure 6.10. The life distributions of short fatigue cracks under three different combinations of texture components, (a) random texture, (b) typical recrystallization texture, and (c) typical rolling texture.
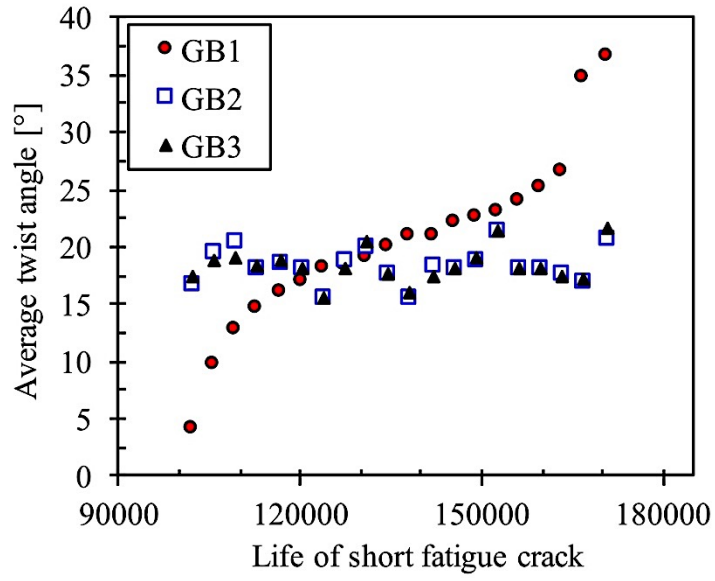
Figure 6.11. The relationship between the life of short fatigue crack and the average twist angle at the 1st, 2nd and 3rd GBs that the crack encountered during its propagation under the grain structure with random texture.
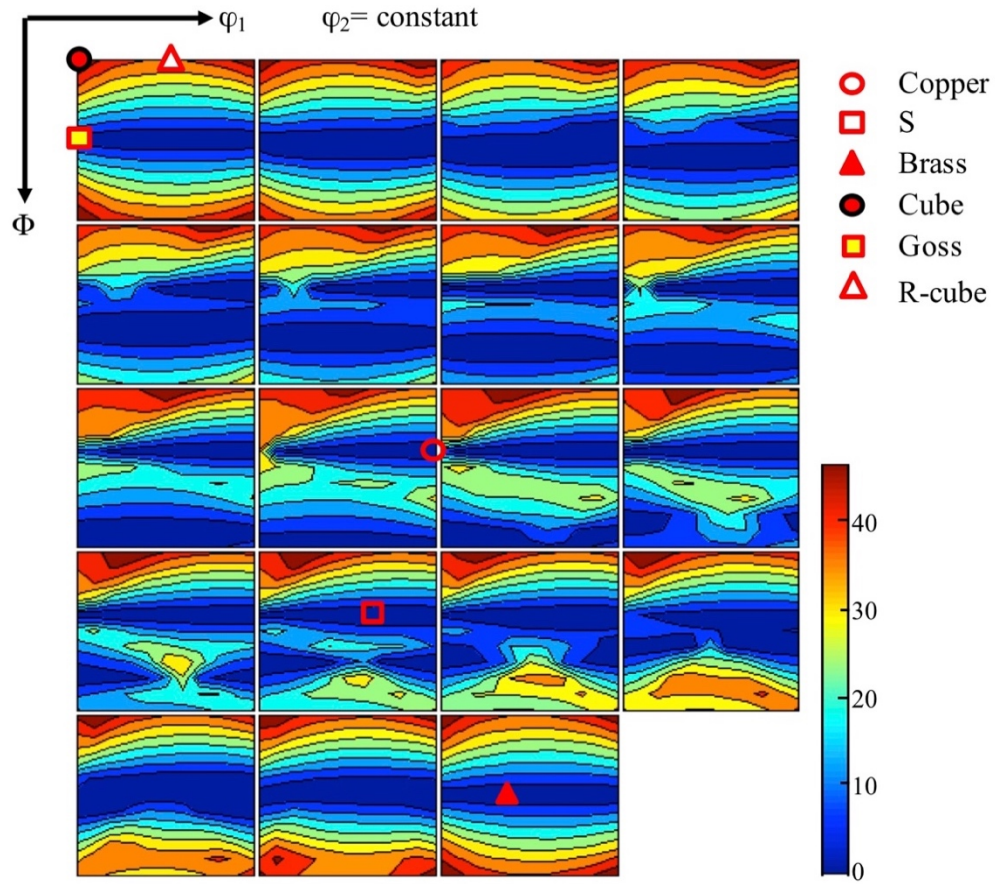
Figure 6.12. The calculated minimum twist angle map at the first GB a short crack encounters with a neighboring grain of different orientations.

163
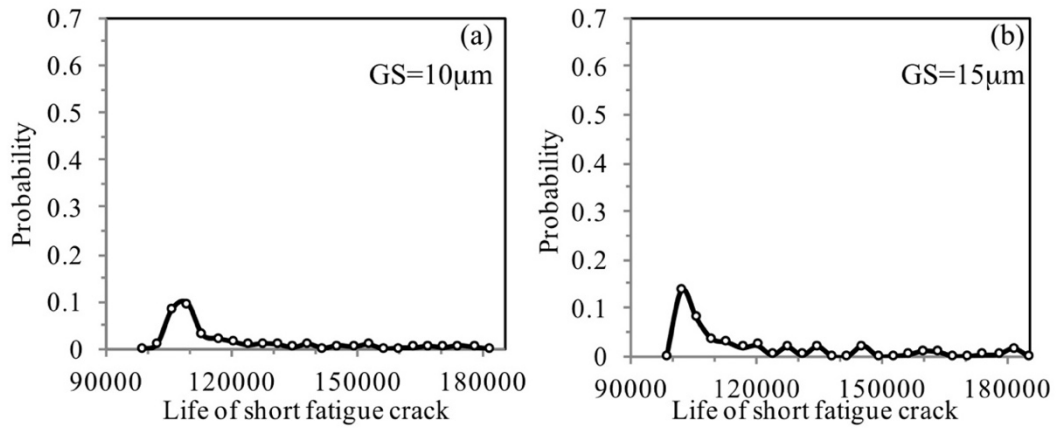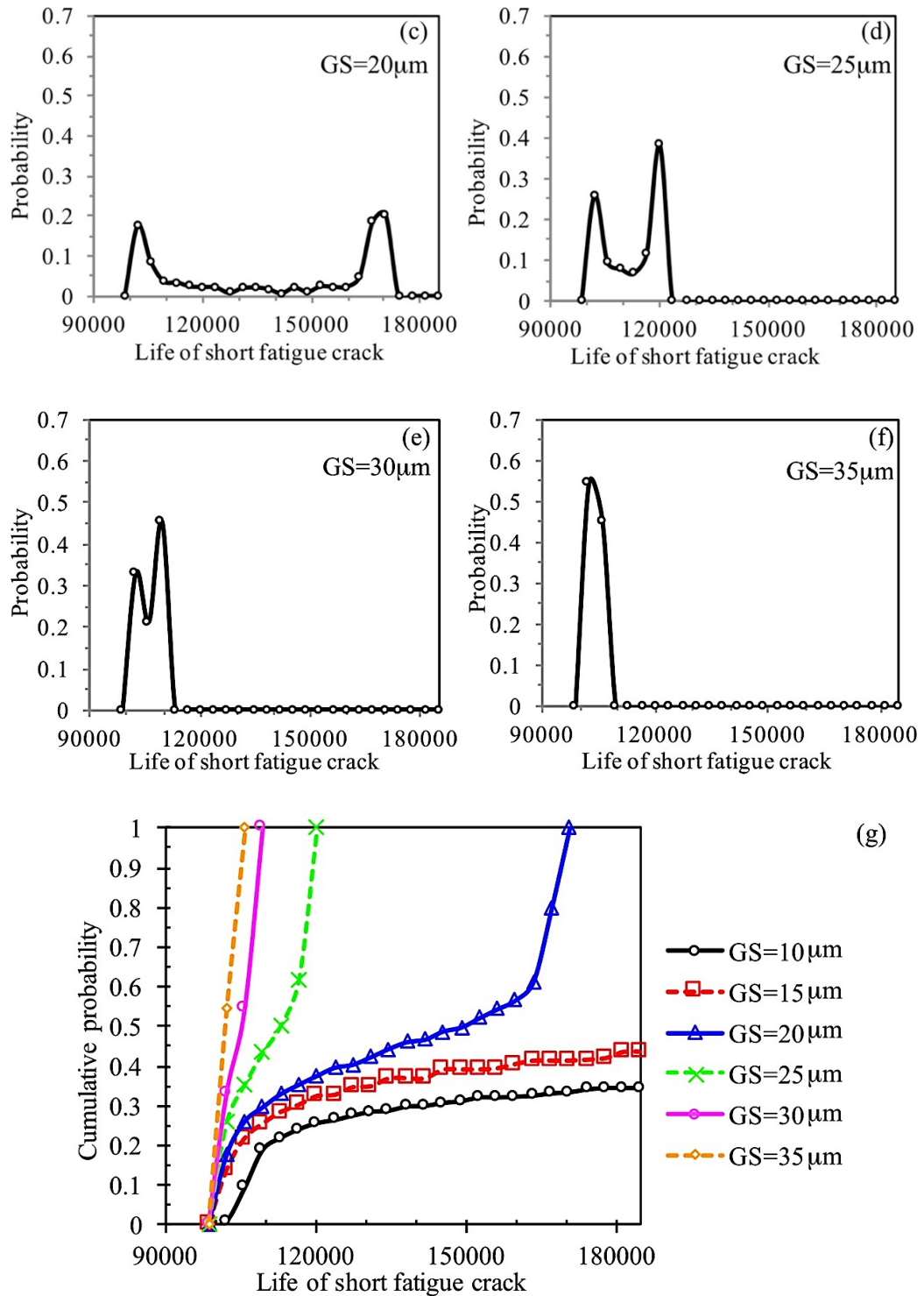
Figure 6.13. The life distributions of short fatigue cracks in grain structures of (a) 10μm, (b) 15μm, (c) 20μm, (d) 25μm, (e) 30μm and (f) 35μm in size, respectively. (g) The cumulative probability of short fatigue crack life in the six different grain sizes.
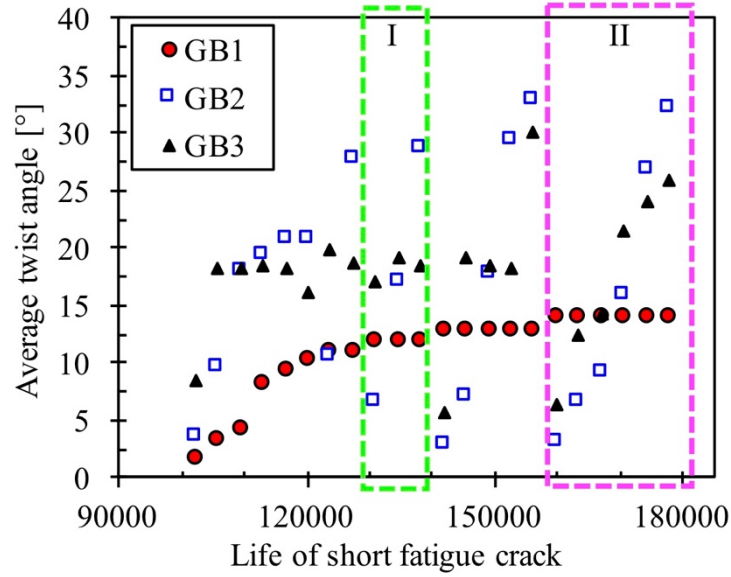
Figure 6.14. (a) The relationship between the short fatigue life and the average twist angle at the 1st, 2nd and 3rd GBs, respectively, that the short fatigue crack encountered during its propagation in a grain structure with an average size of 10μm.

CHAPTER 7   Conclusions

Based on the recent discovery that the twist component of the crack plane deflection at a GB plays an important role in determining the GB resistance against short fatigue crack growth in planar slip engineering alloys, a three-dimensional microstructure-based model was developed in this work to quantify the anomalous growth behaviors of short fatigue cracks in these alloys. By taking into account the effects of microstructure and texture, the model successfully simulates the different growth behaviors of the micro-cracks from pre-fractured constituent particles, and retardation and arrest of short fatigue cracks at GBs. The consistency between the simulated and experimental results of short crack growth in AA2024-T3 Al-Cu alloys and AA8090 Al-Li alloy validates the model. In addition, the model is also able to make prediction of the stochastic growth behaviors of short fatigue cracks in the planar slip alloys with different textures and various grain structures. The exhibits its potentials for advancing the technology for alloy design by optimizing texture and grain structure to achieve maximum resistance against fatigue crack growth. The main conclusions of the current research work are summarized as follows:

1. A microstructure-based model was developed to quantify the 3-D growth behaviors of short fatigue cracks by taking into account both the local nominal driving force and resistance at each point along a crack front in a planar slip alloy. The local driving force ΔK_I was computed by incorporating the stress

concentration effects due to the irregularity in shape on the crack front, while the local resistance R at a GB was quantified by taking into account the resistance of the GB and the dragging effects from the surrounding GBs at which the crack front fell behind relative to the crack front at the GB. The effective driving force ΔK_I-R was used in a microscopic-scale Paris' equation to quantify the growth rate at each point along the crack front beneath the free surface.

2. Knowing the grain orientation, initial particle size and shape, and loading conditions, the model could successfully simulate the three different types of fatigue cracks extended from the micro-cracks in the pre-fractured particles in AA2024 Al alloys.

3. Rectangular micro-notches with different combinations of width on surface and depth beneath the surface were fabricated in the selected grains on the T-S planes in AA2024-T3 Al-Cu alloys using FIB. The growth behaviors of the fatigue cracks initiated from these notches were measured experimentally and compared to those simulated using the model developed in this work. A good agreement was obtained between experimental and theoretical results, confirming that the 3-D geometry of the pre-fractured particles played an important role in determining the growth behaviors of the micro-cracks from the particles in the AA2024 Al alloys.

4. Given the texture in the alloy, a crack propagation map where the growth behavior of the micro-crack in a pre-fractured particle is plotted as a function of particle thickness and width was calculated using the model, from which the probabilities of the occurrence of the three different types of fatigue cracks

propagated from the pre-fracture particles could be quantified in the particle width vs. thickness plot.

5. Experimentally measured texture and distributions of the pre-fractured particle width and thickness in the AA2024-T3 alloys were used to reconstruct the digital microstructure of the alloy in the model. The simulated probabilistic predictions of short fatigue crack growth from the micro-cracks in the pre-fractured particles showed good agreements with the statistical results in the experiments.

6. The consistency between the simulated and experimental results validates the capability of the model in quantifying the texture and particle size effects on the growth behaviors of short fatigue cracks from the pre-fractured particles in planar slip alloys.

7. The model was also used to simulate the 3-D growth behaviors of a naturally-occurring short fatigue crack, giving rise to the results consistent with those experimentally observed in an AA8090 Al-Li alloy. This indicated that the modified Paris' equation was still valid for describing the growth behaviors of short fatigue cracks as long as the local resistance to crack growth was incorporated into the model.

8. Depending on the resistance and position of secondary GBs beneath the surface, their retarding effects on crack growth in the sample surface could be captured by the current model. This explained the crack growth rate drop within a grain, as observed experimentally.

9. The microstructure-based model was capable of quantifying the influence of microstructure and texture, such as primary and secondary GBs, different textures

and grain size, etc., on the statistical growth behaviors of short fatigue cracks in planar slip alloys.

10. It was found that the first few GBs that a short fatigue crack encountered played a crucial role in determining the life of the crack. The smaller the twist component of crack plane deflection at these GBs, the short the life of the short crack.

11. There was a bimodal distribution in the life spectrum of short fatigue cracks in a planar slip alloy, such as AA2024-T3 Al-Cu alloy and AA8090 Al-Li alloy regardless of the texture in the alloy. The "shorter life" peak in the spectrum was related to case with the small twist angle of crack deflection at the first GB the crack encountered, while the "longer life" peak was caused by the large twist angle at the first GB.

12. The recrystallization texture presented a higher resistance against crack growth, thereby leading to a higher probability of longer lives for short fatigue cracks, than a typical rolling type of texture and random texture, respectively.

13. With the current model, it was revealed that grain refinement and secondary GBs could lead to pronounced crack retardation and a higher probability of crack arrest or a longer life for a short crack to reach 500μm in length on surface. With increase in grain size, the location of the "shorter life" peak remained the same in the calculated life spectrum for short cracks, while that of "longer life" peak gradually decreased and eventually merged with the "shorter life" peak, resulting in a unimodal distribution in the life spectrum of short cracks.

14. For the first time, the anomalous growth behaviors of short fatigue cracks, such as crack retardation and arrest at GBs, scattering in growth rate, microstructural and

texture effects, etc., could be quantitatively simulated with the model developed in this work.

REFERENCES

[1] W. Schutz, "A history of fatigue," *Eng. Fract. Mech.,* vol. 54, pp. 263-300, 1995.

[2] F. Braithwaite, "On the fatigue and consequent fracture of metals," *Minutes of Proceed,* vol. XIII, pp. 464-474, 1854.

[3] A. Wohler, "Über die Festigkeits-Versuche mit Eisen und Stahl," *Zeitschrift fur Bauwesen,* vol. XX, pp. 73-106, 1870.

[4] O. Basquin, "The exponential law of endurance tests," *Proc. Annual Meeting, American Society Testing Mater. ,* vol. 10, pp. 625-630, 1910.

[5] S. Kalpakjian, Manufacturing Engineering and Technology, 3rd ed., Addison-Wesley Publishing Co., 1995.

[6] G. Irwin, "Analysis of stresses and strains near the end of a crack traversing a plate," *J. App. Mech.,* vol. 24, pp. 361-364, 1957.

[7] S. Suresh, Fatigue of Materials 2nd ed, Cambridge: UK: Cambridge University Press, 1998.

[8] P. Paris, M. Gomez and W. Anderson, "A rational analytic theory of fatigue," *Trends. Eng. ,* vol. 13, pp. 9-14, 1961.

[9] P. Paris and F. Erdogan, "A critical analysis of crack propagation laws," *J. Basic Eng. ,* vol. 85, pp. 528-534, 1963.

[10] S. Pearson, "Initiation of fatigue crack in commercial aluminium alloys and the subsequent propagation of very short cracks," *Eng. Fract. Mech.,* vol. 7, pp. 235-240, 1975.

[11] W. Morris, "The noncontinuum crack tip deformation behavior of surface microcracks," *Metal. Trans. A,* vol. 11, pp. 1117-1123, 1980.

[12] J. Lankford, "The growth of small fatigue cracks in 7075-T6 aluminum," *Fatigue of Engineering Materials and Structures,* vol. 5, pp. 233-248, 1982.

[13] C. Y. Kung and M. E. Fine, "Fatigue crack initiation and microcrack growth in 2024-T4 and 2124-T4 aluminum alloys," *Metallurgical Transactions A,* vol. 10, pp. 603-610, 1979.

[14] D. Gerard and D. Koss, "The influence of porosity on short fatigue crack growth at large strain amplitude," *Int. J. Fatigue,* vol. 13, pp. 345-352, 1991.

[15] T. Zhai, A. Wilkinson and J. Martin, "The effects of micro-texture and b' particle distribution on short fatigue crack growth in an Al-Li 8090 alloy," *Mater. Sci. Forum,* Vols. 331-337, pp. 1549-1554, 2000.

[16] S. Suresh and R. Ritchie, "Propagation of Short Fatigue Cracks," *Int. Met. Rev. ,* vol. 29, pp. 445-476, 1984.

[17] K. Hussain, "Short fatigue crack behaviour and analytical models: A review," *Eng. Fract. Mech.,* vol. 58, pp. 327-354, 1997.

[18] M. Herbig, A. King, P. Reischig, H. Proudhon, E. Lauridson, J. Marrow, J. Buffiere and W. Ludwig, "3-D growth of a short fatigue crack within a polycrystalline microstructure studied using combined diffraction and phase-contrast X-ray tomography," *Acta Mater. ,* vol. 59, pp. 590-601, 2011.

[19] J. R. Brockenbrough, A. J. Hinkle, P. E. Magnusen and R. J. Bucci, "Microstuctually based model of fatigue and growth," *NASA Conference Publication,* vol. 3274, pp. 71-84, 1994.

[20] C. Q. Bowles and J. Schijve, "The role of inclusions in fatigue crack initiation in an aluminum alloy," *International Journal of Fatigue,* vol. 9, pp. 171-179, 1973.

[21] J. Lankford, "The influence of microstructure on the growth of short fatigue cracks," *Fatigue Eng. Mater. Struct.,* vol. 8, pp. 161-175, 1985.

[22] A. Turnbull and E. de los Rios, "The effect of grain size on fatigue crack growth in aluminium magnisium alloy," *Fatigue Fract. Eng. Mater. ,* vol. 18, pp. 1355-1366, 1995.

[23] A. Zabett and A. Plumtree, "Microstructural effects on the small fatigue crack behavior of an aluminum alloy plate," *Fatigue and Fracture of Engineering Materials and Structures,* vol. 18, pp. 801-809, 1995.

[24] A. Melander, M. Rolfsson, A. Nordgren, B. Jansson, H. Hedberg and T. Lund, "Influence of inclusion contents on fatigue properties of SAE 52100 bearing steels," *Scandinavian Journal of Metallurgy,* vol. 20, pp. 229-244, 1991.

[25] F. Meurling, A. Melander, M. Tidesten and L. Westin, "Influence of carbide and inclusion contents on the fatigue properties of high speed steels and tool steels," *International Journal of Fatigue,* vol. 23, pp. 215-224, 2001.

[26] Y. B. Zhang, C. X. Teng and T. G. Zhai, "Porosities and fatigue property of two A356 cast aluminum alloy," *Applied Mechanics and Materials,* Vols. 423-426, pp. 263-266, 2013.

[27] E. De Los Rios, Z. Tang and K. Miller, "Short crack fatigue behavior in a medium carbon steel," *Fatigue Fract. Eng. Mater. Struct. ,* vol. 7, pp. 97-108, 1984.

[28] K. Tokaji and T. Ogawa, "The growth behaviour of microstructurally short fatigue cracks in metals," in *Short Fatigue Cracks*, K. Miller and E. De Los Rios, Eds., London, Mechanical Engineering Publications, 1992, pp. 85-99.

[29] W. Wen and T. Zhai, "Three-dimensional effects of microstructures on short fatigue crack growth in an Al-Li 8090 alloy," *Philosophical Magazine,* vol. 91, pp. 3557-3577, 2011.

[30] K. S. Chan and J. Lankford, "A crack-tip strain model for the growth of small fatigue cracks," *Scripta Metallurgica,* vol. 17, pp. 529-532, 1983.

[31] A. Navarro and E. R. De Los Rios, "Fatigue crack growth modelling by successive blocking of dislocations," *Proceeding of the Royal Society of London A,* vol. 437, pp. 375-390, 1992.

[32] C. Przybyla, R. Prasannavenkatesan, N. Salajegheh and D. McDowell, "Microstructure-sensitive modeling of high cycle fatigue," *Int. J. Fatigue,* vol. 32, pp. 512-525, 2010.

[33] K. Tanaka, Y. Akiniwa, Y. Nakai and R. P. Wei, "Modelling of small fatigue crack growth interacting with grain boundary," *Engineering Fracture Mechanics,* vol. 24, pp. 803-819, 1986.

[34] P. Hansson and S. Melin, "Dislocation-based modelling of the growth of a microstructurally short crack by single shear due to fatigue loading," *International*

Journal of Fatigue, vol. 27, pp. 347-356, 2005.

[35] P. Hobson, "The formation of a crack growth equation for short cracks," *Fatigue Fract. Eng. Mater. Struct.,* vol. 5, pp. 323-327, 1982.

[36] K. Tokaji, T. Ogawa and K. Ohya, "The effect of grain size on small fatigue crack growth in pure titanium," *Int. J. Fatigue,* vol. 16, pp. 571-578, 1994.

[37] G. Deng, S. Tu, X. Zhang, Q. Wang and C. Qin, "Grain size effect on the small fatigue crack initiation and growth mechanisms of nickel-based superalloy GH4169," *Eng. Fract. Mech.,* vol. 134, pp. 433-450, 2015.

[38] A. Zurek, M. James and W. Morris, "The effect of grain size on fatigue growth of short cracks," *Metal. Trans. A,* vol. 14, pp. 1697-1705, 1983.

[39] W. Schaef, M. Marx, H. Vehoff, A. Heckl and P. Randelzhofer, "A 3-D view on the mechanisms of short fatigue crack interating with grain boundaries," *Acta Materialia,* vol. 59, pp. 1849-1861, 2011.

[40] Y. Zhang and L. Edwards, "The effect of grain boundaries on the development of plastic deformation ahead of small fatigue cracks," *Scr. Metal. Mater.,* vol. 26, pp. 1901-1906, 1992.

[41] Y. Zhang and L. Edwards, "On the blocking effect of grain boundaries on small crystallographic fatigue crack growth," *Mater. Sci. Eng. A,* vol. 188, pp. 121-132, 1994.

[42] T. Zhai, A. J. Wilkinson and J. W. Martin, "A crystallographic mechanism for fatigue crack propagation through grain boundaries," *Acta Materialia,* vol. 48, pp. 4917-4927, 2000.

[43] J. X. Li, T. Zhai, M. D. Garratt and G. H. Bray, "Four-point bend fatigue of AA2026 aluminum alloys," *Metallurgical and Materials Transactions A,* vol. 36A, pp. 2529-2539, 2005.

[44] A. King , W. Ludwig, M. Herbig, J. Y. Buffiere, A. A. Khan, N. Stevens and T. J. Marrow, "Three dimensional in-situ observations of short fatigue crack growth in magnesium," *Acta Materialia,* vol. 59, pp. 6761-6771, 2011.

[45] Z. Liu, F. Li, P. Xia, S. Bai, Y. Gu, D. Yu and S. Zeng, "Mechanisms forGoss-grainsinducedcrackdeflection andenhanced fatigue crackpropagationresistanceinfatiguestageIIofan AA2524alloy," *Mater. Sci. Eng. A,* vol. 625, pp. 271-277, 2015.

[46] W. Wu, Z. Liu, Y. He, F. Li, S. Bai, P. Xia, A. Wang and C. Ye, "Goss texture intensity effect on fatigue crack propagation resistance in an Al-Cu-Mg alloy," *J. Alloys Compd.,* vol. 730, pp. 318-326, 2018.

[47] W. Musinski and D. McDowell, "Simulating the effect of grain boundaries on microstructurally small fatigue crack growth from a focused ion beam notch through a three-dimensional array of grains," *Acta Mater. ,* vol. 112, pp. 20-39, 2016.

[48] C. Bjerken and S. Melin, "A tool to model short crack fatigue growth using a discrete dislocation formulation," *International Journal of Fatigue,* vol. 25, pp. 559-566, 2003.

[49] G. Patton, C. Rinaldi, Y. Brechet, G. Lormand and R. Fougeres, "Study of fatigue

damage in 7010 aluminum alloy," *Materials Science and Engineering A,* vol. 254, pp. 207-218, 1998.

[50] A. Merati, "A study of nucleation and fatigue behavior of an aerospace aluminum alloy 2024-T3," *International Journal of Fatigue,* vol. 27, pp. 33-44, 2005.

[51] H. Weiland, J. Nardiello, S. Zaefferer, S. Cheong, J. Papazian and D. Raabe, "Microstructural aspects of crack nucleation during cyclic loading of AA7075-T651," *Engineering Fracture Mechanics,* vol. 76, pp. 709-714, 2009.

[52] G. Trantina and M. Barishpolsky, "Elastic-plastic analysis of small defects-voids and inclusions," *Engineering Fracture Mechanics,* vol. 20, pp. 1-10, 1984.

[53] A. Melander, "A finite element study of short cracks with different inclusion types under rolling contact fatigue load," *International Journal of Fatigue,* vol. 19, pp. 13-24, 1997.

[54] P. J. Laz and B. M. Hillberry, "Fatigue life prediction from inclusion initiated cracks," *International Journal of Fatigue,* vol. 20, no. 4, pp. 263-270, 1998.

[55] W. Wen, A. H. Ngan, Y. B. Zhang, B. Xu and T. Zhai, "A study of the effects of particle 3-dimensional geometry and micro-texture on fatigue crack initiation behaviors in an Al-Cu alloy using focused ion beam and electron backscatter diffraction," *Materials Science and Engineering A,* vol. 564, pp. 97-101, 2013.

[56] Y. Murakami and S. Beretta, "Small defects and inhomogeneities in fatigue strength: experiments, models and statistical implications," *Extremes,* vol. 2, no. 2, pp. 123-147, 1999.

[57] M. Liao, "Probabilistic modeling of fatigue related microstructural parameters in aluminum alloys," *Engineering Fracture Mechanics,* vol. 76, pp. 668-680, 2009.

[58] M. Liao, G. Renaud and N. Bellinger, "Probabilistic modeling of short-crack growth in airframe aluminum alloys," *Journal of Aircraft,* vol. 45, no. 4, pp. 1105-1111, 2008.

[59] W. Musinski, "Modeling the effects of short-peened residual stresses and inclusions on microstructure-sensitive fatigue of Ni-base superalloy components," *Doctoral Dissertation,* 2014.

[60] J. D. Hochhalter, D. J. Littlewood, M. G. Veilleux, J. E. Bozek, A. M. Maniatty, A. D. Rollett and A. R. Ingraffea, "A geometric approach to medeling microstructurally small fatigue crack formation: III. Development of a semi-empirical model for nucleation," *Modelling and Simulation in Materials Science and Engineering,* vol. 19, pp. 1-27, 2011.

[61] K. Miller, "Metal fatigue-past, current and future," *J. Mech. Eng. Sci.,* vol. 205, pp. 291-304, 1991.

[62] A. Navarro and E. R. De Los Rios, "Short and long fatigue crack growth: a unified model," *Philosophical Magazine,* vol. 57, pp. 15-36, 1988.

[63] A. J. Wilkinson, "Modelling the effects of texture on the statistics of stage I fatigue crack growth," *Philosophical Magazine A,* vol. 81, pp. 841-855, 2001.

[64] B. A. Bilby, A. H. Cotrell and K. H. Swinden, "The spread of plastic yield from a notch," *Proceeding of the Royal Society of London A,* vol. 272, pp. 304-314, 1963.

[65] B. Kunkler, O. Duber, P. Koster, U. Krupp, C. P. Fritzen and H. J. Christ,

"Modelling of short crack propagation- transition from stage I to stage II," *Engineering Fracture Mechanics,* vol. 75, pp. 715-725, 2008.

[66] P. Koster, H. Knobbe, C. P. Fritzen, H. J. Christ and U. Krupp, "A three-dimensional model for stage I-crack propagation," *Technische Mechanik,* vol. 30, pp. 185-194, 2010 .

[67] D. A. Hills, P. A. Kelly, D. N. Dai and A. M. Korsunsky, Solution of crack problems-The distributed dislocation technique, Springer Netherlands, 1996.

[68] C. Bjerken and S. Melin, "A study of the influence of grain boundaries on short crack growth during varying load using a dislocation technique," *Engineering Fracture Mechanics,* vol. 71, pp. 2215-2227, 2004.

[69] C. Bjerken, "The discrete nature of the growth and arrest of microstructurally short fatigue cracks modelled by dislocation technique," *International Journal of Fatigue,* vol. 27, pp. 21-32, 2005.

[70] P. Hansson and S. Melin, "Grain boundary influence on short fatigue crack growth rate," *International Journal of Fracture,* vol. 165, pp. 199-210, 2010.

[71] T. Zhai, X. P. Jiang, J. X. Li, M. D. Garratt and G. H. Bray, "The grain boundary geometry for optimum resistance to growth of short fatigue cracks in high strength Al-alloys," *International Journal of Fatigue,* vol. 27, pp. 1202-1209, 2005.

[72] W. Wen, P. Cai, T. Zhai and A. H. Ngan, "An experimental methodology to quantify the resistance of grain boundaries to fatigue crack growth in an AA2024 T351 Al-Cu Alloy," *Mater. Sci. Eng. A,* vol. 666, pp. 288-296, 2016.

[73] M. Herbig, A. King, P. Reischig, H. Proudhon, E. M. Lauridson, J. Marrow, J. Y. Buffiere and W. Ludwig, "3-D growth of a short fatigue crack within a polycrystalline microstructure studied using combined diffraction and phase-contrast X-ray tomography," *Acta Materialia,* vol. 59, pp. 590-601, 2011.

[74] F. Campbell, Elements of metallurgy and engineering alloys, ASM International, 2008.

[75] SpaceX, "Falcon Heavy," SpaceX, 2017. [Online]. Available: http://www.spacex.com/falcon-heavy.

[76] G. Gottstein, Physical foundations of materials science, Springer, 2004.

[77] V. Gerold and H. Karnthaler, "On the origin of planar slip in F.C.C. alloys," *Acta Metall.,* vol. 37, pp. 2177-2183, 1989.

[78] A. Bregianos, A. Crosky, P. Munroe and A. Hellier, "A study aimed at determining and understanding the fracture behaviour of an Al-Li-Cu-Mg-Zr alloy 8090," *Int. J. Fract.,* vol. 161, pp. 141-159, 2010.

[79] W. Cassada, G. Shiflet and E. Starke, "The effect of germanium on the precipitation and deformation behavior of Al-2Li alloys," *Acta Metall.,* vol. 34, pp. 367-378, 1986.

[80] T. Hidayetoglu, P. Pica and W. Haworth, "Aging dependence of the Bauschinger effect in aluminum alloy 2024," *Mater. Sci. Eng.,* vol. 73, pp. 65-76, 1985.

[81] H. Shih, N. Ho and J. Huang, "Precipitation behaviors in Al-Cu-Mg and 2024 aluminum alloys," *Metal. Mater. Trans. A,* vol. 27, pp. 2479-2494, 1996.

[82] T. Zhai, "Strength distribution of fatigue crack initiation sites in an Al-Li alloy,"

Metal. Mater. Trans. A, vol. 37, pp. 3139-3147, 2006.

[83] Annual book of ASTM standards 2000, ASTM Intl., 2000.

[84] L. Grabowski and J. Yates, "The effect of specimen geometry on short-crack growth bahaviour of a nickel-based superalloy," *Int. J. Fatigue,* vol. 14, pp. 227-232, 1992.

[85] T. Zhai, Y. G. Xu, J. W. Martin, A. J. Wilkinson and G. A. D. Briggs, "A self-aligning four-point bend testing rig and sample geometry effect in four-point bend fatigue," *International Journal of Fatigue,* vol. 21, pp. 889-894, 1999.

[86] O. Engler, Introduction to texture analysis-macrotexture, microtexture and orientation mapping, 2 ed., CPC Press, 2010.

[87] C. Volkert and S. Minor, "Focused ion beam microscopy and micomachining," *MRS Bulletin,* vol. 32, pp. 389-399, 2007.

[88] S. Reyntjens and R. Puers, "A review of focused ion beam applications in microsystem technology," *J. Micromech. Microeng. ,* vol. 11, pp. 287-300, 2001.

[89] Fibics, "Introduction: Focused Ion Beam Systems," Fibics Incorporated, 2018. [Online]. Available: http://www.fibics.com/fib/tutorials/introduction-focused-ion-beam-systems/4/.

[90] S. Güngör and L. Edwards, "Effect of surface texture on the initiation and propagation of small fatigue cracks in a forged 6082 aluminum alloy," *Materials Sicence and Engineering A,* vol. 160, no. 1, pp. 17-24, 1993.

[91] S. Taira, K. Tanaka and Y. Nakai, "A model of crack-tip slip band blocked by grain boundary," *Mechanics Research Communications,* vol. 5, no. 6, pp. 375-381, 1978.

[92] E. R. De Los Rio and A. Navarro, "Considerations of grain orientation and work hardening on short-fatigue-crack modelling," *Philosophical Magazine A,* vol. 61, no. 3, pp. 435-449, 1990.

[93] F. P. Riemelmoser, R. Pippan and H. P. Stuwe, "An argument for a cycle-by-cycle propagation of fatigue cracks at small stress intensity ranges," *Acta Mater.,* vol. 46, pp. 1793-1799, 1998.

[94] A. J. Wilkinson, S. G. Roberts and P. B. Hirsch, "Modeling the threshold considerations for propagation of stage I fatigue cracks," *Acta Mater.,* vol. 46, pp. 379-390, 1998.

[95] W. Ludwig, J. Y. Buffiere, S. Savelli and P. Cloetens, "Study of the interaction of a short fatigue crack with grain boundaries in a cast Al alloy using X-ray microtomography," *Acta Materialia,* vol. 51, pp. 585-598, 2003.

[96] M. Oja, K. S. Ravi Chandran and R. G. Tryon, "Orientation imaging microscopy of fatigue crack formation in Waspaloy: crystallographic conditions for crack nucleation," *International Journal of Fatigue,* vol. 32, pp. 551-556, 2010.

[97] W. O. Soboyejo, W. Shen and T. S. Srivatsan, "An investigation of fatigue crack nucleation and growth in a Ti-6Al-4V/TiB in situ composite," *Mechanics of Materials,* vol. 36, pp. 141-159, 2004.

[98] Y. Murakami, Metal Fatigue: Effects of Small Defects and Nonmetallic Inclusions, New York: Elsevier, 2002.

[99] J. C. Newman and I. S. Raju, "Empirical stress intensity factor equation for the

surface crack," *Engineering Fracture Mechanics,* vol. 15, pp. 185-192, 1981.

[100] W. Wen and T. Zhai, "Quantification of Resistance of Grain Boundaries to Short-Fatigue Crack Growth in Three Dimensions in High-Strength Al Alloys," *Metallurgical and Materials Transactions A,* vol. 43, pp. 2743-2752, 2012.

[101] X. J. Wu, W. Wallace, M. D. Raizenne and A. K. Koul, "The Orientation Dependence of Fatigue Crack Growth in 8090 Al-Li Plate," *Metallurgical and Materials Transactions A,* vol. 25, pp. 575-588, 1994.

[102] W. Schaef, M. Marx and A. F. Knorr, "Influence of microstructural barriers on small fatigue crack growth in mild steel," *Int. J. Fatigue,* vol. 57, pp. 86-92, 2013.

[103] Y. Jin, P. Cai and T. Zhai, "An experimental methodology for quantitative characterization of multi-site fatigue crack nucleation in high-strength Al alloys," *Fatigue Fract. Eng. Mater. Struct.,* vol. 00, pp. 1-16, 2016.

[104] M. Oore and D. Burns, "Estimation of stress intensity factors for embedded irregular cracks subjected to arbitrary normal stress fields," *J. pressure vessel tech. ,* vol. 102, pp. 202-211, 1980.

[105] J. Rice, "Some remarks on elastic crack-tip stress fields," *Int. J. Solids Struct. ,* vol. 8, pp. 751-758, 1972.

[106] E. Mastrojannis, L. Keer and T. Mura, "Stress intensity factor for a plane crack under normal pressure," *Int. J. Fract. ,* vol. 15, pp. 247-258, 1979.

[107] P. Livieri and F. Segala, "An analysis of three-dimensional planar embedded cracks subjected to uniform tensile stress," *Eng. Fract. Mech.,* vol. 77, pp. 1656-1664, 2010.

[108] L. Keer, "A class of non-symmetrical punch and crack problems," *Q. J. Mech. Appl. Math.,* vol. 17, pp. 423-436, 1964.

[109] L. Sneddon and M. Lowengrub, Crack problems in the classic theory of elasticity, New York: J. Wiley and Son, 1969.

[110] S. Chan, I. Tuba and W. Wilson, "On the finite element method in linear fracture mechanics," *Eng. Fract. Mech.,* vol. 2, pp. 1-17, 1970.

[111] T. Cruse, "Numerical solutions in three dimensional elastostatics," *Int. J. Solids Struct. ,* vol. 5, pp. 1259-1274, 1969.

[112] H. Bueckner, "A novel principle for the computation of stress intensity factors," *Z Agnew Math. Mech.,* vol. 50, pp. 529-546, 1970.

[113] H. Montenegro, A. Cisilino and J. Otegui, "A weight function methodology for the assessment of embedded and surface irregular plane cracks," *Eng. Fract. Mech.,* vol. 73, pp. 2662-2684, 2006.

[114] P. Livieri and F. Segala, "First order Oore-Burns integral for nearly circular cracks under uniform tensile loading," *Int. J. Solid Struct. ,* vol. 47, pp. 1167-1176, 2010.

[115] J. Weaver, "Three-dimensional crack analysis," *Int. J. Solids Struct.,* vol. 13, pp. 321-330, 1977.

[116] Q. Wang, N. Noda, M. Honda and M. Chen, "Variation of stress intensity factor along the front of a 3D rectangular crack by using a singular integral equation method," *Int. J. Fract.,* vol. 108, pp. 119-131, 2001.

[117] M. Isida, T. Yoshida and H. Noguchi, "A rectangular crack in an infinite solid, a semi-infinite solid and a finite-thickness plate subjected to tension," *Int. J. Fract.,* vol. 52, pp. 79-90, 1991.

[118] J. C. Newman Jr, "A review of modelling small-crack behavior and fatigue-life predictions for aluminum alloys," *Fatigue and Fracture of Engineering Materials and Structures,* vol. 17, no. 4, pp. 429-439, 1994.

[119] M. Liao, "Dislocation theory based short crack model and its application for aircraft aluminum alloy," *Engineering Fracture Mechanics,* vol. 77, pp. 22-36, 2010.

[120] C. Vallellano, A. Navarro, F. J. Garcia-Lomas and J. Dominguez, "On the estimation of microstructural effects in the near-threshold fatigue of small cracks," *Journal of Strain Analysis for Engineering Design,* vol. 43, pp. 337-347, 2008.

[121] J. E. Bozek, J. D. Hochhalter, M. G. Veilleux, M. Liu, G. Heber, S. D. Sintay, A. D. Rollett, D. J. Littlewood, A. M. Maniatty, H. Weiland, R. J. Christ Jr, J. Payne, G. Welsh, D. G. Harlow, P. A. Wawrzynek and A. R. Ingraffea, "A geometric approach to modeling microstructurally small fatigue crack formation: I. Probabilistic simulation of constituent particle cracking in AA7075-T651," *Modelling and Simulation in Materials Science and Engineering,* vol. 16, pp. 1-28, 2008.

[122] F. Bergner and G. Zouhar, "A new approach to the correlation between the coefficient and the exponent in the power law equation of fatigue crack growth," *International Journal of Fatigue,* vol. 22, pp. 229-239, 2000.

[123] E. A. DeBartolo and B. M. Hillberry, "Effects of constituent particle clusters on fatigue behavior of 2024-T3 aluminum alloy," *International Journal of Fatigue,* vol. 20, pp. 727-735, 1998.

[124] E. A. DeBartolo and B. M. Hillberry, "A model of initial flaw sizes in aluminum alloys," *International Journal of Fatigue,* vol. 23, pp. S79-86, 2001.

VITA OF PEI CAI

Place of Birth: Beijing, CHINA

Education:

- University of Kentucky, Lexington, Kentucky, USA

  08/2013-present   Ph.D. candidate (Materials Science and Engineering)
- RWTH Aachen University, Germany

  08/2010-07/2013   M.Sc. (Metallurgical Engineering)
- University of Science and Technology Beijing, China

  09/2006-07/2010   B.Sc. (Materials Science and Engineering)

Award Received:

- Outstanding Graduate Student Award, University of Kentucky, 2017
- Best Poster Award, *2017 International Symposium on Multiscale Modeling and Simulation of Materials*, Shenyang, China
- The 1st prize of poster competition, *Fatigue in Materials: Fundamentals, Multiscale Modeling and Prevention, TMS2016*, Nashville, TN, USA
- Visiting Scientist Grant, the University of Hong Kong, 2015

Professional Service:

- President of Materials Research Society-University of Kentucky Chapter, 2016-2017
- Reviewer of *Scientific Reports*, *Metallurgical and Materials Transactions A*, *Fatigue & Fracture of Engineering Materials & Structures*, *Journal of Materials Engineering and Performance*, *Journal of Testing and Evaluation.*

Publications:

1. **<u>Pei Cai</u>**, W. Wen and T. Zhai, "A novel microstructure-based model validated experimentally for simulating short fatigue crack growth in 3-D in planar slip alloys", *Materials Science and Engineering A, under review*.

2. **<u>Pei Cai</u>**, Y. Jin and T. Zhai, "Simulation of short fatigue crack growth from micro-notches in an AA2024-T351 Al alloy using a 3D microstructure-based model", *to be submitted*.

3. **<u>Pei Cai</u>**, Y. Jin and T. Zhai, "Simulation of the stochastic growth behaviors of short fatigue cracks from pre-fracture particles in planar slip alloys", *to be submitted*.

4. **<u>Pei Cai</u>** and T. Zhai, "Quantification of driving force for the growth of an arbitrary-shape planar fatigue crack in three-dimensions", to be submitted.

5. L. Yang, **<u>Pei Cai</u>**, Z. Xu, Y. Jin, C. Liang, F. Yin and T. Zhai, "A 3-D model for quantification of fatigue weak-link density and strength distribution in an A713 cast aluminum alloy", *International Journal of Fatigue*, 96(2017), 185-195.

6. Z. Lv, **<u>Pei Cai</u>**, T. Yu, Y. Jin, H. Zhang, W. Fu and T. Zhai, "Fatigue behaviors and damage mechanism of a Cr-Mn-N austenitic steel", *Journal of Alloys and Compounds*, 691(2017), 103-109.

7. W. Wen, **<u>Pei Cai</u>***, A.H.W. Ngan and T. Zhai, "An experimental methodology to quantify the resistance of grain boundaries to fatigue crack growth in an AA2024-T351 Al-Cu Alloy", *Materials Science and Engineering A*, 666(2016), 288-296.

   a. **Equally contributed first author.*

8. Y. Jin, **<u>Pei Cai</u>**, Q. Tian, C. Liang, D. Ke, G. Wang and T. Zhai, "An experimental methodology for quantitative characterization of multi-site fatigue crack nucleation in high strength aluminum alloys", *Fatigue & Fracture of Engineering Materials & Structures*, 00 (2016), 1-16.

9. L. Yang, Y. Jin, **<u>Pei Cai</u>**, F. Yin, Q. Li and T. Zhai, "Quantification of fatigue weak-links in high strength Al alloys", *Materials Science Forum*, 877(2016), pp. 427-434.

10. Y. Niu, H. Liu, X. Liu, Y. Jiang, X. Ren, **<u>Pei Cai</u>** and T. Zhai, "Study on nano-pores enlargement during Ag-assisted electroless etching of diamond wire sawn polycrystalline silicon wafers", *Materials Science in Semiconductor Processing*, 56(2016), 119-126.

11. Y. Jin, **<u>Pei Cai</u>**, W. Wen, H. Nagaumi, B. Xu, Y. Zhang and T. Zhai, "The anisotropy of fatigue crack nucleation in an AA7075-T651 Al alloy plate", *Materials Science and Engineering A* 622(2015), 7-15.

Technical Presentations (*presenter):

1. **Pei Cai*** and T. Zhai, "Simulation of stochastic behaviors of fatigue crack initiation from pre-fractured constituent particles in high-strength Al alloys", *2017 ASM International Bluegrass Chapter Meeting*, Oct. 24, 2017, Lexington, KY, USA. (**Invited**)
2. **Pei Cai***, L. Yang, F. Yin, C. Liang and T. Zhai, "Quantification of multi-site fatigue crack initiation by considering the 3-D effects of micro-pores in 713 cast Al alloys", *2017 International Symposium of Multi-Scale Modeling & Simulation of Materials*, July 3-7, 2017, Shenyang, China. (**Invited**)
3. **Pei Cai***, "Simulation of stochastic behaviors of fatigue crack initiation from pre-fractured constituent particles in high-strength Al alloys", *Hebei University of Technology*, June 16, 2017 Tianjin, China. (**Invited**)
4. **Pei Cai*** and T. Zhai, "From quantitative understanding to statistic prediction of early fatigue crack growth in high strength Al alloys", *2017 MACE Symposium*, May 12, 2017, Lexington, KY, USA. (**Invited**)
5. Y. Jin*, L. Yang, **Pei Cai**, J. Xu, W. Sun, D. Leonard, F. Yang, Y.T. Cheng and T. Zhai, "A 3-D understanding of the anisotropy in fatigue crack nucleation in an AA7075-T651 Al alloy plate". 2016 *TMS meeting*, Nashville, TN, USA. (**Invited**)
6. **Pei Cai***, Y. Jin and T. Zhai, "From quantitative understanding to statistic prediction of micro-crack growth behaviors from pre-fractured particles inAA2024", 2017 *TMS meeting*, Feb. 26-Mar. 2, 2017, San Diego, CA, USA.
7. **Pei Cai***, L. Yang, Y. Jin, Z. Xu and T. Zhai, "Probabilistic analysis of the fatigue incubation life distribution in an A713 cast Al alloy based on a multi-sized pore-sensitive numerical model", *2017 TMS meeting*, Feb. 26-Mar. 2, 2017, San Diego, CA, USA.
8. **Pei Cai***, W. Wen, Y. Jin and T. Zhai, "Quantitative effects of texture and grain size on short fatigue crack growth in high strength Al alloys by a 3D microstructural-based model", *TMS 2016*, Feb. 14-18, 2016, Nashville, TN, USA.
9. **Pei Cai***, Y. Jin, A.H.W. Ngan and T. Zhai, "Modelling of the 3D effects of particles on fatigue crack initiation in high strength Al alloys". *2015 TMS meeting*, Mar. 15-19, 2015, Orlando, FL, USA.
10. **Pei Cai***, Y. Jin, W. Wen, D.N. Leonard and T. Zhai, "Quantitative understanding 3-D effects of constituent particles on fatigue crack initiation in high strength aluminum alloys by FIB", *2015 CNMS User Meeting*, September 1-2, 2015, Oak Ridge National Laboratory, Oak Ridge, TN, USA (poster).
11. Y. Jin*, **Pei Cai** and T. Zhai etc. 3-D effects of constituent particles on fatigue crack initiation in high strength aluminum alloys by FIB, 2015 TMS meeting, Mar. 15-19, 2015, Orlando, FL, USA.